Design and Construction of Graphene-Based Advanced Materials for Emerging Concept Supercapacitors

by

Wenwen Liu

A thesis

presented to the University of Waterloo

in fulfillment of the

thesis requirement for the degree of

Doctor of Philosophy

in

Chemical Engineering (Nanotechnology)

Waterloo, Ontario, Canada, 2020

Examining committee membership

The following served on the Examining Committee for this thesis. The decision of the Examining Committee is by majority vote.

External Examiner	**Name**: Elena A. Baranova Title: Professor Institution: Department of Chemical and Biological Engineering, University of Ottawa
Supervisor	**Name**: Aiping Yu Title: Associate Professor Institution: Department of Chemical Engineer, University of Waterloo
Internal Member	**Name**: Eric Croiset Title: Professor Institution: Department of Chemical Engineer, University of Waterloo
Internal Member	**Name**: Jeff Gostick Title: Associate Professor Institution: Department of Chemical Engineer, University of Waterloo
Internal-external Member	**Name**: Bo Cui Title: Professor Institution: Department of Electrical and Computer Engineering, University of Waterloo

Author’s declaration

This thesis consists of material all of which I authored or co-authored: see Statement of contributions included in the thesis. This is a true copy of the thesis, including any required final revisions, as accepted by my examiners.

I understand that my thesis may be made electronically available to the public.

Statement of contributions

The body of this thesis is based on a combination of published works. Various sections are adapted from the following list of publications.

Chapter 3

W. Liu, J. Li, K. Feng, A. Sy, Y. Liu, L. Lim, G. Lui, R. Tjanda, L. Rasenthiram, G. Chiu, A. Yu. "Advanced Li-ion hybrid supercapacitors based on 3D graphene-foam composites". *ACS Appl. Mater. Interfaces*, **2016**, *8*, 25941-25953. Reproduced with permission.[108] Copyright 2016, The American Chemical Society.

Prof. A. Yu proposed and supervised the project. Prof. A. Yu and I discussed the logical structure of the paper. I carried out the experiment and finished the writing of manuscript. Dr. J. Li conducted all DFT calculations. Dr. K. Feng, Mr. A. Sy and Mr. L. Lim assisted with the synthesis of materials. Dr. Y. Liu helped with drawing the schematic illustration. Dr. G. Lui, Dr. R. Tjanda, Mr. L. Rasenthiram, and Dr. G. Chiu edited the manuscript. All authors reviewed the manuscript.

Chapter 4

W. Liu, K. Feng, Y. Zhang, T. Yu, L. Han, G. Lui, M. Li, G. Chiu, P. Fung, A. Yu. "Hair-based flexible knittable supercapacitor with wide operating voltage and ultra-high rate capability". *Nano Energy* **2017**, *34*, 491-499. Reproduced with permission.[169] Copyright 2017, Elsevier.

Prof. A. Yu proposed and supervised the project. Prof. A. Yu and I designed the

experiments. Dr. K. Feng, Dr. Y. Zhang and I carried out characterization of the related materials. Dr. K. Feng, Dr. T. Yu, Dr. L. Han and I performed the device assembly and electrochemical characterization. Prof. A. Yu, Dr. G. Lui, Mr. M. Li, Dr. G. Chiu, Ms. P. Fung, and I analyzed the data and wrote the paper. All authors discussed the results and commented on the manuscript.

Chapter 5

W. Liu, M. Zhang, M. Li, B. Li, W. Zhang, G. Li, M. Xiao, J. Zhu, A. Yu, Z. Chen. "Advanced electrode materials comprising of structure engineered quantum dots for high-performance asymmetric micro-supercapacitors". *Adv. Energy Mater.*, **2020,** *10*, 1903724. Reproduced with permission.[219] Copyright 2020, WILEY-VCH.

Prof. A. Yu and Prof. Z. Chen proposed and supervised the project. I design the experiment, carried out the characterizations, and wrote the manuscript. Ms. M. Zhang and Mr. M. Li assisted some material characterizations. Mr. M. Li and Ms. B. Li edited the manuscript. Dr. W. Zhang helped with drawing the schematic illustration of device. Dr. G. Li, Dr. M. Xiao, and Dr. J. Zhu assisted with the electrochemical testing. All authors reviewed the manuscript.

W. Liu, M. Li, G. Jiang, G. Li, J. Zhu, M. Xiao, Y. Zhu, R. Gao, A. Yu, M. Feng, Z. Chen. "Graphene quantum dots-based advanced electrode materials: design, synthesis and their applications in electrochemical energy storage and electrocatalysis". *Adv. Energy Mater.*, **2020**, *10*, 2001275. Reproduced with permission.[220] Copyright 2020, WILEY-VCH.

Prof. A. Yu, Prof. Z. Chen, and Prof. M. Feng proposed and supervised the project. I wrote the manuscript. Mr. M. Li, Dr. G. Jiang, Dr. G. Li, and Dr. M. Xiao edited the manuscript. Dr. G. jiang, Dr. M. Xiao, Dr. J. Zhu, and Dr. R. Gao assisted with the electrocatalysis section. Dr. G. Li, Mr. Y. Zhu assisted with the battery section. All authors reviewed the manuscript.

Abstract

Supercapacitors (SCs) as a new class of energy storage devices have attracted great attention in industry and academia community due to their higher energy density than dielectric capacitors, higher power density than rechargeable batteries, long cycle life, safety and environment friendliness. Although they have many attractive advantages and much work has been done to improve their performance, their relatively low energy density compared with batteries has severely limited their practical applications to some extent. At the same time, the rapid development of micro-electromechanical systems (MEMS), portable/wearable electronic devices, and self-powered systems have stimulated new demands for SCs with small size, various shapes, lightweight, flexibility as well as compatibility. However, the current development of SCs with large size, heavy weight and rigid nature clearly lags behind these new requirements. To address these issues, it is highly desired to develop new-concept SCs by innovating upon their design from various aspects (e.g., electrode materials, electrode configuration, and preparation technology), thus matching these new demands and endowing the obtained SCs with real applications.

Based on the above considerations, my thesis mainly focuses on the development of new-concept SCs by exploring alternative electrode materials with unique structure and texture, introducing new energy storage mechanism, and designing new electrode configuration to overcome the abovementioned limitations and meet these new requirements:

(1) To increase the energy density of SCs, lithium ion hybrid supercapacitors (LIHSs) as a new-concept energy storage system have been constructed by consisting of a battery-type anode (3D graphene-wrapped MoO_3 nanobelts foam) and a capacitor-type cathode

(3D graphene-wrapped polyaniline nanotube derived carbon). From the viewpoint of material design, it is expected to effectively take the advantage of each component and synergistic effect to endow the resulting materials with excellent electrochemical performance. Encouragingly, benefiting from these unique structures and configuration, the obtained LIHSs exhibit large operating voltage (up to 3.8 V), high energy and power densities, and long cycling stability.

(2) To match these emerging portable/wearable electronic devices, a flexible fiber-shaped micro-supercapacitor (MSC) has been rationally designed and successfully prepared with coaxial human hair/Ni/graphene/MnO_2 fiber as positive electrode and coaxial human hair/Ni/graphene fiber as negative electrode. With the facile fabrication technique (e.g., self-assembly, chemical bath) and the unique morphology and structure of electrode materials as well as the asymmetrical configuration, the as-prepared MSCs display extraordinary flexibility and outstanding electrochemical performance including a wide potential window, an excellent rate capability, a fast frequency response (τ_0 = 55 ms), a high volumetric energy density, and a long cycle life.

(3) In the last section, the surface and structural engineering strategies by downsizing to quantum dot scale, doping heteroatoms, creating more defects, and introducing more rich functional groups are employed to tailor the physicochemical properties of 2D materials (e.g., graphene, MoS_2), thereby boosting the electrochemical performance of in-plane MSCs. Notably, the resulting nitrogen-doped graphene quantum dots (N-GQDs) and molybdenum disulfide quantum dots (MoS_2-QDs) show outstanding electrochemical performance as negative and positive electrode materials, respectively. Importantly, the obtained N-GQDs//MoS_2-QDs asymmetric in-plane MSCs exhibit a

large operating voltage up to 1.5 V (far exceeding that of most reported MSCs), an ultrafast frequency response (with a short time constant of 0.087 ms), a high energy density, and a long-term stability.

Acknowledgements

I would like to express my sincere gratitude to my supervisor Prof. Aiping Yu for giving me the great opportunity to study at the University of Waterloo and be trained in the promising field of electrochemical energy storage and electrocatalysis. Her continuous support, encouragement, and guidance as well as thoughtful comments and valuable suggestions help me in all the time of my Ph.D. study. Her patience, vision, and profound knowledge in materials science as well as dedication to science not only steer me through my research, but also motivate me to think beyond the box and go farther than I thought I could. In a word, it is such a great honor to study under her guidance.

Besides my advisor, I am also very grateful to my Ph.D. thesis examining committee members: Prof. Elena A. Baranova, Prof. Bo Cui, Prof. Eric Croiset, and Prof. Jeff Gostick for their time, insightful comments, and constructive suggestions as well as inspiring questions. Also, I gratefully acknowledge the financial support from Natural Science and Engineering Research Council of Canada, the Waterloo Institute for Nanotechnology, and the University of Waterloo.

I greatly appreciate the help and support received from all group members in Applied Carbon Nanotechnology Laboratory during the past several years, making my Ph.D. study in an environment with happiness and fulfillment. And many thanks also go to my friends for their accompany, advice, and help as well as fun we have had during the past few years. All the good time that we spent together will always stay in my memory.

Special thanks to my dearest wife for giving me selfless love, great help and strong support to go through this journey even when the road gets tough. Thank you for pushing me

to become better and stronger, giving me the motivation to strive to lead a meaningful life, and guiding me take the responsibility that I should have. Particularly, thank you for making a long trip from Singapore to Canada to celebrate Chinese New Year and Christmas Holiday with me. In a short, I cannot imagine my life without you standing beside me.

Last but not the least, I would like to thank my family, including my parents, younger brother, sister-in-law, and nieces, for their unselfish love, endless joy, and unconditional support. I do not think that I could go through this journey without you all.

Table of contents

List of figures

List of tables

List of abbreviations

AC	Activated carbon
BET	Brunauer-Emmett-Teller
CNTs	Carbon nanotubes
CPs	Conductive polymers
CV	Cyclic voltammetry
DDI	Distilled de-ionized
DEC	Diethyl carbonate
DFT	Density functional theory
1D	One-dimensional
3D	Three-dimensional
EIS	Electrochemical impedance spectra
EDS	Energy-dispersive X-ray spectroscopy
EDL	Electric double layer
EDLCs	Electric double layer capacitors
ESR	Equivalent series resistance
ESW	Electrochemical stability window
EC	Ethylene carbonate
FMSCs	Fiber-shaped micro-supercapacitors
GCD	Galvanic charge/discharge
GNSs	Graphene nanosheets
GO	Graphene oxide

LIHSs	Li ion hybrid supercapacitors
MSCs	Micro-supercapacitors
MoS_2-QDs	Molybdenum disulfide quantum dots
NMP	N-methyl-2-pyrrolidinone
N-GQDs	Nitrogen-doped graphene quantum dots
PPY	Polypyrrole
PANI	Polyamine
PTh	Polythiophene
PEDOT	Poly(3,4-ethylenedioxythiophene)
PP	Polypropylene
PE	Polyethylene
PTFE	Poly(tetrafluoroethylene)
PVDF	Polyvinylidene difluoride
PAA	Polyacrylic acid
PDDA	Poly(diallyldimethylammonium chloride)
PVA	Polyvinyl alcohol
QDs	Duantum dots
SEM	Scanning electron microscopy
SAED	Selected area electron diffraction
TEM	Transmission electron microscopy
XRD	X-ray powder diffraction
XPS	X-ray photoelectron spectroscopy
Z_W	Warburg resistance

Chapter 1: Background and motivation

1.1 Introduction

To response the depletion of fossil fuel, global warming and environmental pollution as well as the rapid development of electric vehicles, there is an urgent need to explore highly efficient, cheap in cost, green and sustainable electrochemical energy storage and conversion systems to meet these demands.[1-4] Among these devices, supercapacitors (SCs) have received extensive attention in the research and engineering communities due to its unique advantages such as high power density, fast charge/discharge rate, excellent cycling stability, wide operating temperature, high safety (**Table 1-1**).[5-7] Owing to these advantages, they are widely utilized in many fields such as public transportation tools, memory back-up devices.[7-9]

However, the restriction of charge stored at or near the surface of electrode materials leads to the relatively lower charge storage capacity and energy density compared with those of batteries, which seriously limits their large-scale applications to some extent.[10-12] As reported, the energy stored in SCs is associated with the surface adsorption/desorption of electrolyte ions at the electrode/electrolyte interface (electric double layer capacitors (EDLCs)) or fast surface redox reaction (pseudo-capacitors). [13-15] In this case, the pursuit of advanced electrode materials with high energy and power densities as well as prolonged cycle life are highly required. Fortunately, Li-ion hybrid supercapacitors (LIHSs) as novel energy storage system are expected to simultaneously improve both energy and power densities by the synergistic effect of a battery-type anode and a capacitor-type cathode in

organic electrolyte.[16, 17] However, the sluggish kinetics of anode and the low capacity of cathode result in unsatisfactory performance of the LIHSs such as relatively low energy density, poor rate capability, and short life cycle. [17-19] Some attempts have been made to explore the alternative high-performance anode and cathode materials because the overall performance of LIHSs strongly depends on the electrode materials,[20-23] but how to rationally design and construct the ideal configuration constituted by a battery-type anode and a capacitor-type cathode is still a challenge but meaningful work.

Additionally, portable/wearable electronic devices (e.g., health monitor systems, flexible displays) have also received great interest and will dominate the market of modern electronics in near future,[23-26] but conventional SCs with large size, heavy weight and rigid nature cannot meet these new requirements and serve as energy sources to power these electronic devices.[27-30] For this purpose, it is also urgent and important to exploit the new energy storage systems to match these emerging portable/wearable devices. Among these emerging energy storage systems, micro-supercapacitors (MSCs) have sparked lots of interests due to their unique configuration and advantages such as small size, light weight, excellent rate capability as well as long lifespan.[31-34] Currently, some efforts have been made, but the unsatisfactory performances (e.g., narrow potential window, low energy density, and slow frequency response capability) of these MSCs hinder their further application.[34-37] Therefore, it is highly desired to design and construct the novel MSCs with excellent electrochemical performances by adopting different techniques and strategies.

In a word, meeting these new and higher challenges existing in the electric vehicles and next-generation consumer electronics, especially portable/wearable electronic devices, strongly relies on the design and construction of new-concept SCs, which not only possess

the superior super-capacitive performance, but also have low-cost, simple preparation process and good compatibility. Based on these considerations, the core work of this thesis is devoted to the design and construction of novel and high-performance supercapacitors with unique electrode structure and configurations, which include the synthesis of electrode materials, the device design and assembly, and the physical and chemical characterization of related nanomaterials/devices as well as corresponding electrochemical performance evaluation.

Table 1-1 Comparison of the performance of supercapacitors with electrostatic capacitors and batteries.[2]

Parameter	Supercapacitors	Electrostatic capacitors	Batteries
Discharge time (s)	0.3-30	10^{-6}-10^{-3}	1800-10800
Charge time (s)	0.3-30	10^{-6}-10^{-3}	3600-18000
Operating voltage (V)	1-2.7	6-800	1.2-4.2
Energy density ($Wh \cdot kg^{-1}$)	1-10	< 0.1	10-100
Power density ($W \cdot kg^{-1}$)	1000	> 10,000	50-200
Energy efficiency	0.85-0.98	1	0.7-0.85
Cycle numbers	> 100,000	> 500,000	500-2000
Operating temperature (℃)	-40-85	-20-100	-40-85
Form factor	Small	Small to Large	Large
Wight (g)	1-2	1-10000	> 10000

1.2 Fundamentals of supercapacitors

Currently, the research associated with SCs has become a hot topic, which is not only due to their promising applications in many fields, but also because of the remaining problems and challenges pushing the researchers to put many efforts in this field. In this sense, it is very necessary to present a comprehensive analysis of supercapacitors including their structure, components, and current research progresses of each critical part as well as their energy storage mechanism, which are beneficial for the better understanding of the fundamentals of SCs and inspiring the researchers to adopt the most effective strategy to address the major difficulties found.

1.2.1 Structure and components of supercapacitors

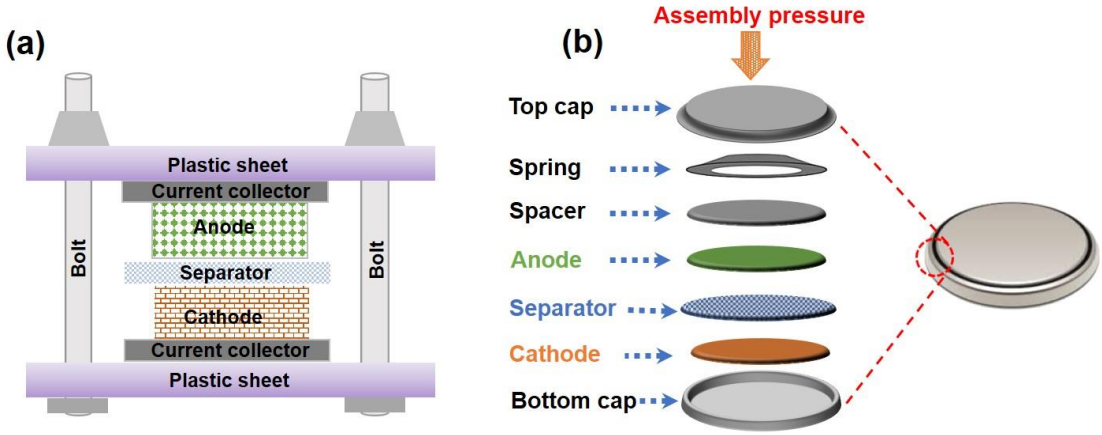

Figure 1-1 Schematic illustration a supercapacitor device (a) open system device, (b) close system device (coin cell).

The SCs come in many different shapes (e.g. cylindrical cell, button cell, pouch cell), sizes, capacity, and even energy storage mechanism, but they are comprised by some general characteristics/components such as two electrodes, electrolyte, separator (**Figure 1-1**).[38, 39] Each component plays a different role in SCs, thus affecting the performance of SCs in

different way. [40,41] In this section, the function and basic requirements of each component (e.g., electrode, electrolyte, separator) as well as their problems are briefly introduced, which are some key points that should be considered when designing and constructing high-performance SCs.

1.2.1.1 Electrode materials

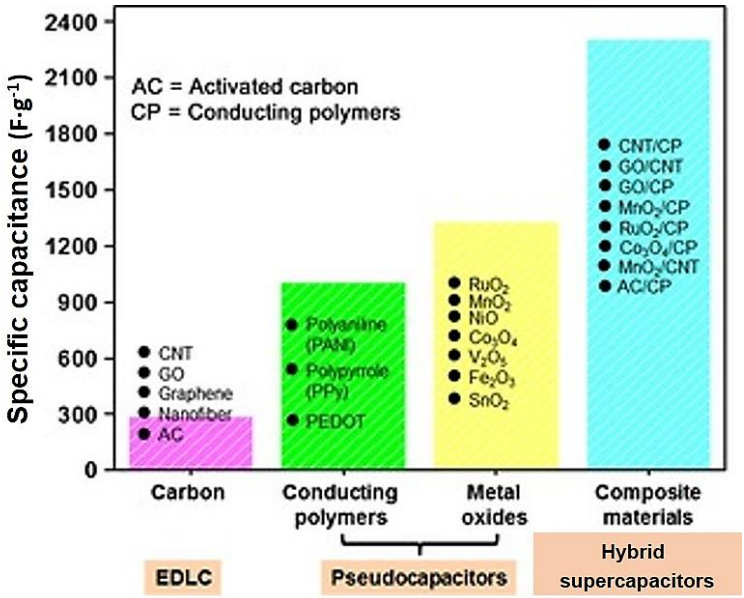

Figure 1-2 Comparison of specific capacitance of various electrode materials for supercapacitors. Reproduced with permission.[42] Copyright 2015, WILEY-VCH.

Electrode materials as a core component of SCs have significant effects on the performance of SCs. This is because the entire performance of SCs strongly relies on the intrinsic properties of electrode materials. Therefore, many works have been done to design various types of advanced electrode materials for the construction of high-performance SCs. The essential requirements for electrode materials are high specific capacitance, large surface area, good conductivity, excellent electro-/chemical stability (inertness), earth

abundance, environmental friendliness and low cost. Currently, carbon materials, conductive polymers, and metal oxides are three typical types of electrode materials for SCs (**Figure 1-2**), [42, 43] which exhibit the obvious discrepancy in electrochemical performance such as different energy storage mechanism, specific capacitance, and lifespan. Furthermore, the hybrid nanomaterials, consisting of a combination of carbon material and pseudocapacitive material or two pseudocapacitive materials, are also developed to boost the electrochemical performance by the synergistic effects from each component. Here, it should be mentioned that, to make more clarity and well understand the property of each type of electrode materials as well as their current research status, the hybrid nanomaterials are not discussed in this section.

1.2.1.1.1 Carbon materials

Among these materials, carbon materials with various manifestations such as activated carbon (AC), carbon fiber, carbon aerogel, graphene and its derivatives are the most used electrode materials. [44-46] Generally, carbon-based materials display an ideal electrical double layer capacitance behavior (**Figure 1-3a**), even though there is a small amount of pseudocapacitance introduced by the functional group and heteroatoms doping (**Figure 1-3b**). The capacitive performance of carbon materials is significantly influenced by many critical factors such as specific surface area, graphitization, functional group, porosity, and electrical conductivity (**Figure 1-3c**). To design and achieve a satisfactory electrode material, it is necessary to investigate the effects of these key factors on the performance of SCs as well as understanding some general guidelines and effective strategies to tailor these key factors, which can provide some useful thoughts and reference for the researchers.

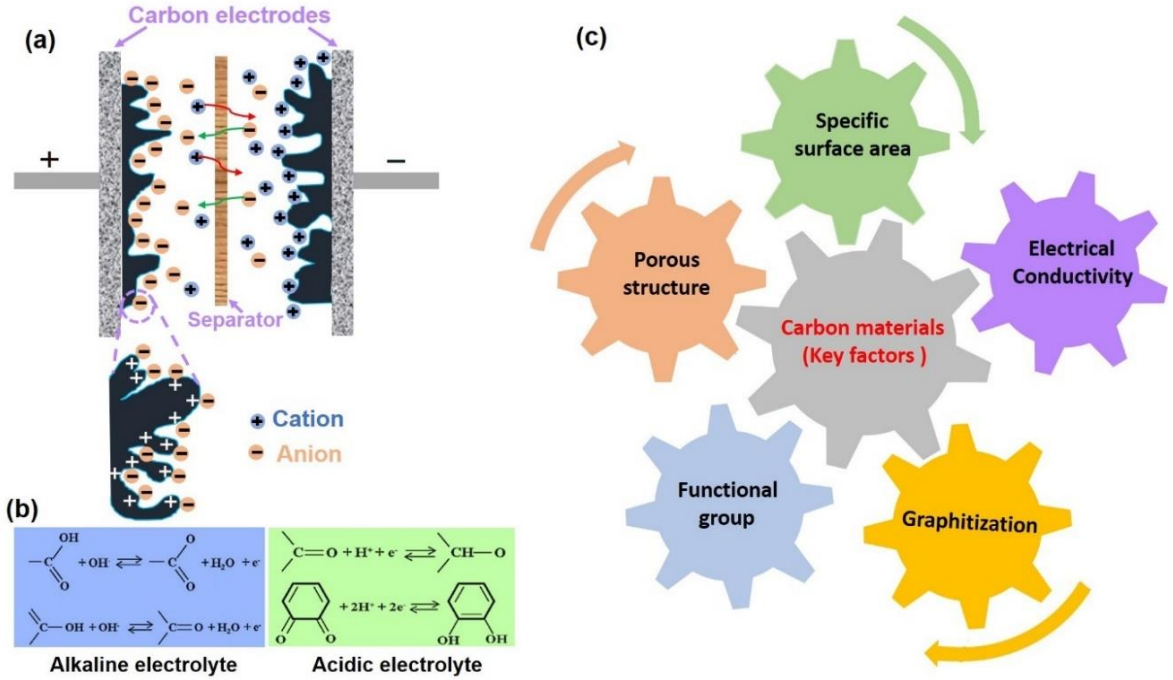

Figure 1-3 (a) Schematic illustration of carbon-based SCs under charged status, (b) Pseudocapacitance contribution of different functional groups in different aqueous electrolytes, (c) Key factors influencing the supercapacitive performance of carbon mataerials.

Usually, pore sizes in carbon materials is ranging from micropores (≤ 2 nm) to mesopores (2-50 nm),[47] which play the different roles in the charge/discharge process of supercapacitors. Among them, mesopores can serve as the reservoir of electrolyte and reduce the ion diffusion distance, thus beneficial for the improvement of rate capability, while micropores contribute to the specific surface area and provide more contact area with the electrolytes, thereby enhancing the specific capacitance.[48-50] In short, more macropores are required to improve the rate capability and enhance the power density of electrodes, while more micropores are highly desired to achieve the high energy density. Despite many progresses made, the contribution of micropores is still under debate. Recently, the new

results reveal that, as pore size is close to or smaller than the size of solvated ions, only de-solvated ions can access and fill the pores, thus contributing to the capacity. [50] Notably, the specific surface area and pore size distribution of carbon materials can be effectively tailored by different chemical and/or physical activation process. The former is carried out by mixing amorphous carbons with certain chemicals (e.g., alkalis, carbonates, chlorides, acids) followed by heat-treated at high temperature, while the latter is achieved in an oxidizing atmosphere (e.g. CO_2, H_2O) under high temperature conditions. [44]

Additionally, it is found that the relatively high synthesis temperature facilitates to form high graphitized carbon materials, thus improving the conductivity of electrode materials and enhancing their electrochemical performance, but the high temperature will lead to the collapse of the produced porous structure during the activation process. Therefore, there is a trade-off between of porosity and graphitization of carbon materials. Besides, heteroatom doping is another effective strategy to boost the electrochemical performance by tailoring electronic conductivity, adjusting the wetting behavior, and introducing pseudocapacitance contribution. [48-50] Based on the above-mentioned, the performance of carbon materials is closely associated with their surface and structure properties as well as kinetic feature, hence when designing high-performance EDLCs, carbon materials with large surface area, high conductivity, appropriate pore size distribution, and good wettability are highly needed.

1.2.1.1.2 Metal oxides

Metal oxides have also been considered as one of the prominent electrode materials due to their multiple oxidation states, rich abundance, and good environmental friendless. Early study of metal oxides mainly focuses on noble metal oxides (e.g., RuO_2, IrO_2) owing to their

high theoretical capacitance (about 2000 $F \cdot g^{-1}$), high conductivity, and good faradic reaction reversibility.[51-53] As a representative noble metal oxide, the faradic reaction of RuO_2 can be described as following equation:[54]

$$RuO_2 + xH^+ + xe^- \leftrightarrow RuO_{2-x}(OH)_x \qquad (0 \leq x \leq 2) \qquad (1\text{-}1)$$

Unfortunately, the high-cost and poisonous nature limit their large-scale applications even though they have delivered remarkable electrochemical performance. In this case, the research and development trends have switched to explore alterative base-metal oxides (e.g., MnO_2, NiO, Co_3O_4, CuO, V_2O_5, TiO_2) with superior electrochemical performance, abundant resources, and low-cost. [55-60] Particularly, MnO_2 as a promising candidate to replace RuO_2 has been widely reported as electrode material in SCs. Currently, there are two kinds of energy storage mechanisms proposed:

$$MnO_2 + C^+ + e^- \leftrightarrow MnOOC \qquad (1\text{-}2)$$

$$(MnO_2)_{surface} + C^+ + e^- \leftrightarrow (MnOOC)_{surface} \qquad (1\text{-}3)$$

Where the former indicates the insertion/de-insertion of electrolyte ions into the bulk of MnO_2, while the latter is based on the fast adsorption/desorption of ions on MnO_2 surface. [54] On the other hand, bi-metal oxides (e.g., $NiCo_2O_4$, $FeCo_2O_4$, $MnCo_2O_4$) with spinel structures have also been extensively studied because of their better electrochemical performance compared with individual components.[61-63] However, they also encounter the similar problems with single-metal oxides such as short cycle-life and unsatisfactory rate performance.

In addition to the different intrinsic properties of these metal oxides resulting in the discrepancy of electrochemical performance, the crystal structure and morphology (e.g.,

nanoflowers, nanospheres, nanoarrays) as well as synthesis methods also have an important impact on their electrochemical performance.[64-66] Because these hierarchical nanomaterials self-assembled from low dimensional building blocks (e.g., nanoparticles, nanosheets, nanowires) will result in the obvious difference in specific surface area, electroactive sites, ion diffusion pathway as well as structure stability. In this case, the controllable design and synthesis of hierarchical nanostructured metal oxides with remarkable electrochemical performance is a feasible way to improve the performance even though it is still a big challenge at this stage. Besides, the construction of metal oxides-based nanocomposites (e.g., metal oxides/carbon materials, metal oxides/conductive polymers) is also employed to boost their electrochemical performance by taking the advantage of each component and synergistic effects.[67, 68]

1.2.1.1.3 Conductive polymers

Besides transition metal oxides, conductive polymers (CPs) are another typical class of electrode material with pseudocapacitive behavior.[70, 71] Importantly, their unique merits (e.g., high electric conductivity, considerable structural diversity, excellent mechanical flexibility, and low cost) endow them with great potential for SCs. Due to their advantages such as large specific capacitance and relatively high conductivity (**Figure 1-4**), many CPs have been popularly used as electrode materials in SCs such as polypyrrole (PPy), polyamine (PANI), polythiophene (PTh), poly(3,4-ethylenedioxythiophene) (PEDOT).[60]

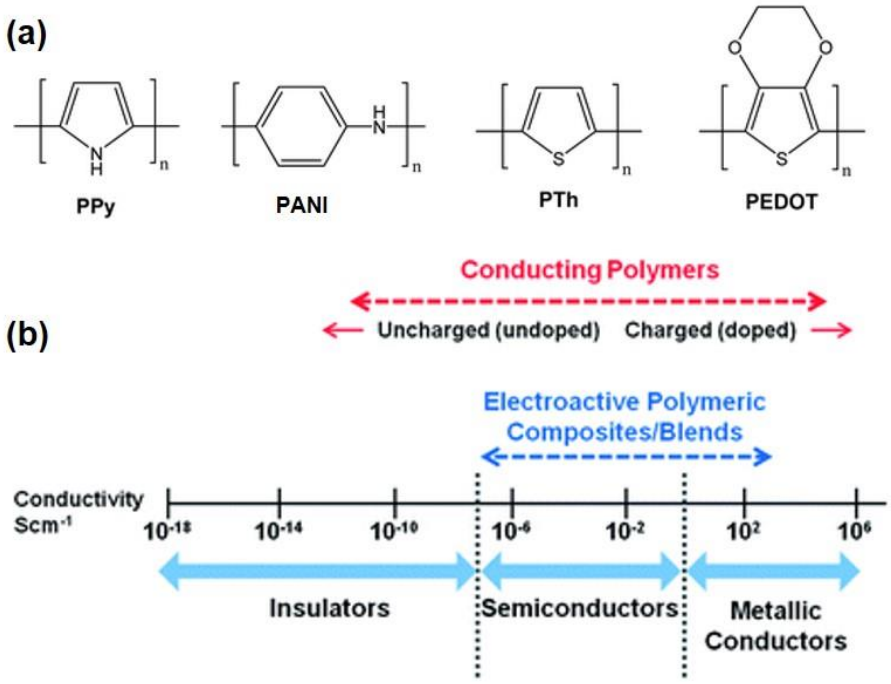

Figure 1-4 (a) Structure of four representative conductive polymers (CPs), (b) Conductivity range of CPs. Reproduced with permission.[69] Copyright 2015, The Royal Society of Chemistry.

Compared with carbon materials, CPs store a greater amount of charge through a Faradic process, where the counter ions move in and out of the conductive polymer backbones during the reversible doping and de-doping processes (**Figure 1-5**). The detail energy storage mechanism of CPs can be described by the following two formulas based on their different states: [70]

$$CP \leftrightarrow CP^{n+}(A^-)_n + ne^- \ (P-doping) \qquad (1\text{-}4)$$

$$CP + ne^- \leftrightarrow (C^+)_n CP^{n-} \ (N-doping) \qquad (1\text{-}5)$$

Where A and C stand for the anion and cation in the electrolyte. Generally, most of CPs (e.g., PANI, PPy) work as P-doped state while only a few (e.g., PTh) work as N-doped. However, CPs usually suffer remarkable capacitance decay because of the swelling and shrinking of

electrode structure during the charge/discharge process. It is no doubt that the poor cycle stability greatly restricts their practical applications. To improve the cycle stability, designing the CPs-based nanocomposites by combing CPs with other materials (e.g., carbon materials, metal oxides) are conducted.[72-75]

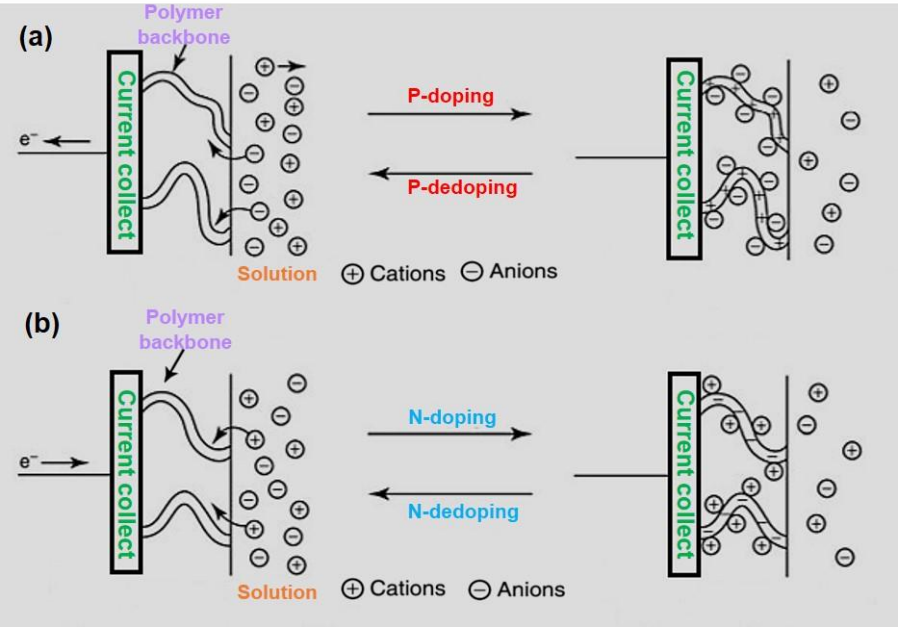

Figure 1-5 Schematic illustration of the conductive polymer's energy storage mechanism with different states: (a) p-doping upon oxidization and (b) n-doping upon reduction, respectively. Reproduced with permission.[71] Copyright 1994, Elsevier.

1.2.1.2 Electrolyte

Generally, electrolyte is consisted by a solvent and a dissolved chemical with dissociated cations and anions, thus making the electrolyte electrically conductive. Currently, aqueous electrolytes, organic electrolytes and ionic liquids are the most popularly used electrolytes. In SCs electrolyte ions migrate between cathode and anode in the internal circuit during charge/discharge process, which are the conductive connection between these two electrodes. Therefore, it is noted that electrolyte is directly related to the

supercapacitor's characteristics such as operating voltage, operating temperature range, equivalent series resistance and capacitance. There are several basic requirements for the electrolytes used for SCs. First, it should have a high ion conductivity over the temperature range of supercapacitor operation. Aqueous electrolytes typically have higher conductivity (100 to 1000 mS/cm) compared with those of organic electrolytes (10 to 60 mS/cm) and ionic liquids (a few mS/cm), which results in small equivalent series resistance (ESR), desirable for high power devices. [39, 76-79] Second, it should possess large electrochemical stability window (ESW), which extends the cell voltage. Aqueous electrolytes display a small ESW due to the decomposition of water (1.23 V),[39] which is much smaller than the one obtained from organic electrolytes (around 3 V) or ionic liquids (around 4.5 V).[76] Moreover, the electrolyte should possess inert chemical property and does not chemically react with other materials to ensure long-term stability of SCs. In addition, its viscosity should be low enough to wet the electrodes, which benefits to the increase of the specific capacitance and the improvement of rate capability of SCs.

Based on the above-mentioned, an ideal electrolyte should contain many characteristics such as good electrochemical stability, high conductivity, low viscosity, good wettability, low volatility, and low cost. Currently, it is difficult to find an ideal electrolyte with so many excellent characteristics, thus meeting the requirements in real applications. Besides, the gel electrolytes are also developed by incorporating the above-mentioned electrolyte into a polymer matrix, which is beneficial for the design of all-solid-state SCs.

1.2.1.3 Separator

The separator soaked in electrolyte physically separates cathode and anode electrodes to avoid their direct contact, thus preventing short circuit. [80] In this case, the separator material should contain the following characteristics. First, the separator should be very thin with porous structure which can effectively isolate electron but allow ions to flow through easily during the charge/discharge process, thereby minimizing the ESR and boosting the performance of device. [81, 82] Second, a promising separator should have the capability to uptake a large amount of electrolyte, which enables it with high ionic conductivity. Third, the separator should have enough mechanical strength, which is closely related to the porosity. When the porosity of the separator reaches to over a certain value, the corresponding tensile strength of the separator gradually decreases. Therefore, there is a trade-off between the mechanical strength and the porosity of the separator. Apart from these properties, separator should be chemical inert and does not react with the electrode as well as stable in the entire potential range. Furthermore, for safety purpose, separator should withstand a certain high temperature.

Currently, many materials have been used to fabricate the separator such as non-woven fibers, polymers, natural substrates.[83] In the lab, filtration paper can be temporally used as separator for SCs. In addition, some nonwoven porous polymeric films, woven glass fibers, and porous woven ceramic fibers can also be used as separator. Generally, ceramic or glass fiber separators are suitable for aqueous electrolytes while polymer or paper separators are used for non-aqueous electrolytes. [39]

1.2.2 Energy storage mechanism of supercapacitors

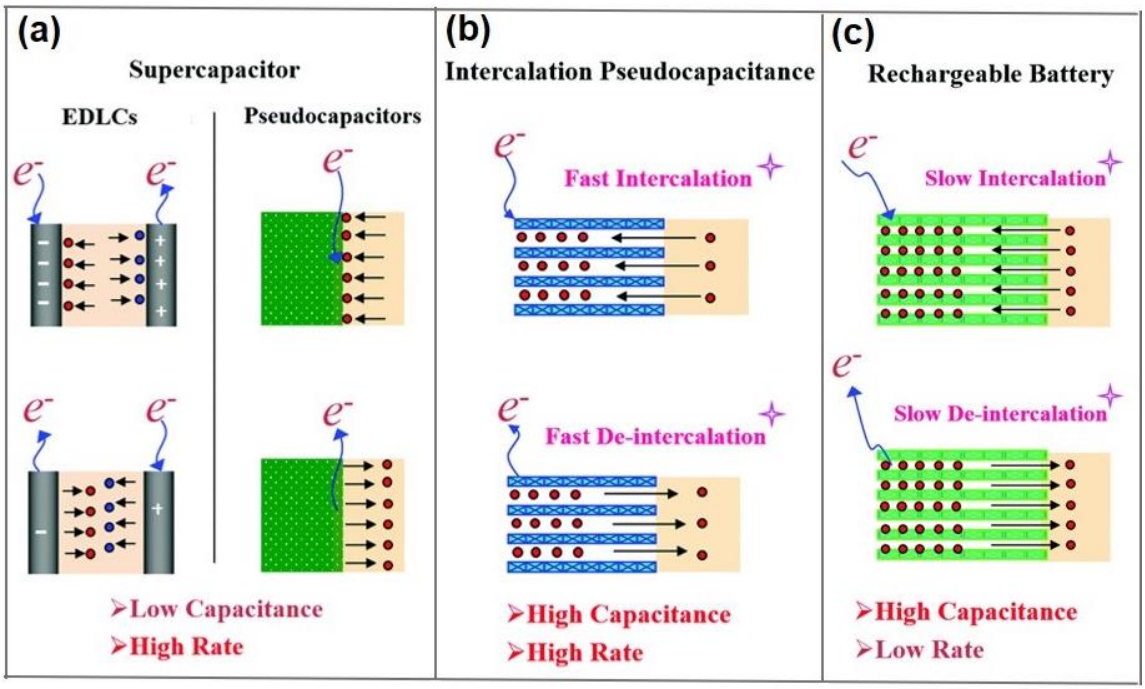

Figure 1-6 Schematic illustration of charge storage mechanism of different device/material: (a) Supercapacitor, (b) Intercalation pseudocapacitive material, and (c) Rechargeable battery, respectively. Reproduced with permission.[84] Copyright 2016, The Royal Society of Chemistry.

The capacitance of SCs strongly rely on the surface reactions of electrode materials (**Figure 1-6a**), including the adsorption/desorption of ions at the electrode/electrolyte interface (i.e., EDLCs) and the fast surface redox reactions (i.e., pseudo-capacitors). [44,72,84] Based on the energy storage mechanism, SCs can be divided into three categories: EDLCs, pseudocapacitors, and hybrid SCs. Moreover, to make more clarity, the energy storage mechanism of SCs is also compared with that of material with intercalation pseudo-capacitance behavior and rechargeable batteries (**Figure 1-6**).

1.2.2.1 Electric double layer capacitors (EDLCs)

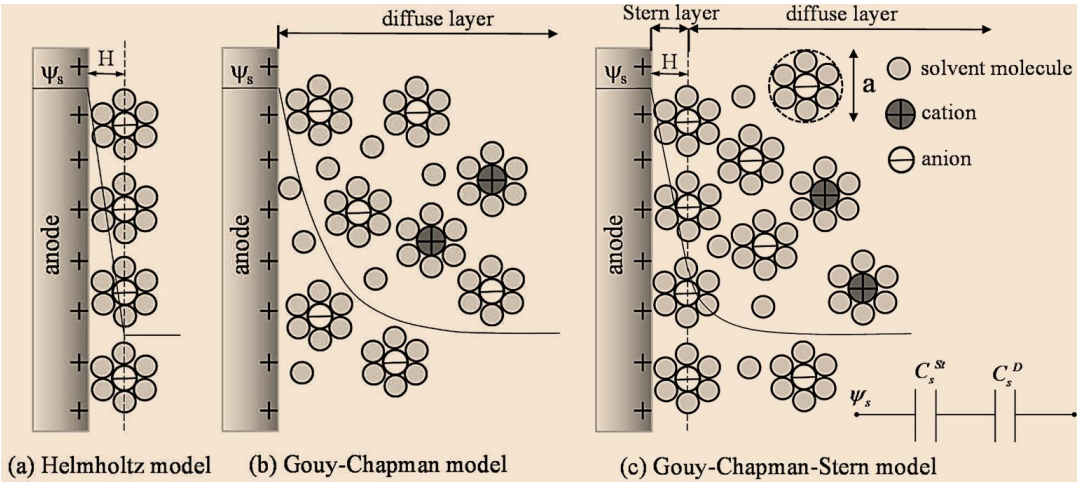

Figure 1-7 Schematic illustration of three classic electric double layer (EDL) structure proposed: (a) Helmholtz model, (b) Gouy-Chapman model, and (c) Gouy-Chapman-Stern model, respectively. Reproduced with permission.[85] Copyright 2017, American Chemical Society.

There are three famous models developed by the scientists to describe the EDL structure (**Figure 1-7**): Helmholtz model, Gouy-Chapman model, and Gouy-Chapman-Stern model, [85] respectively. However, the Helmholtz model only considers two layers of opposite charge formed at the electrode/electrolyte interface with a distance equaling the hydrated ions radius (**Figure 1-7a**). On the contrary, the Gouy-Chapman model just thinks that the ions with an opposite charge are loosely distributed in a region (**Figure 1-7b**), where the thickness is much larger than the radius of hydrated ions. Both reveal the EDL structure from different angles, but they cannot comprehensively and accurately reflect the real EDL structure. In this case, Gouy–Chapman–Stern model has been proposed by combining the Helmholtz model with the Gouy–Chapman model (**Figure 1-7c**). Compared with the previous two models, the Gouy–Chapman model has been proved to be a good description of the EDL structure and been widely accepted by the researchers until now.

Based on this theory, the capacitance in these EDLCs is stored as an accumulation of charge in the electric double layer formed at the interface between the high surface area electrode and the electrolyte. Therefore, the storage capacity of EDLCs is boosted by a large contact area of the electrode/electrolyte. Currently, carbon materials (e.g., AC, porous carbon) are ideal EDL electrode materials owing to their large surface area, high electrical conductivity, and low density. [39,86]

1.2.2.2 Pseudo-capacitors

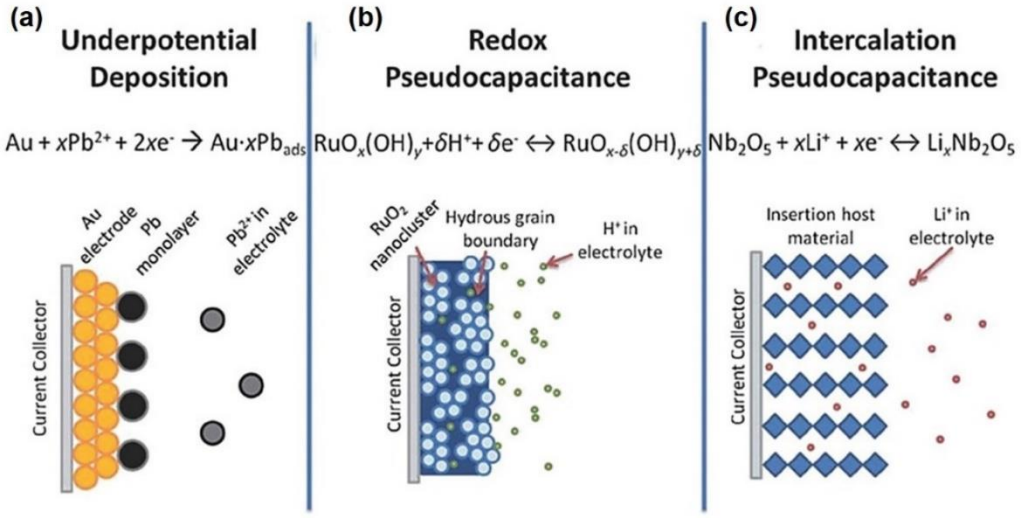

Figure 1-8 Schematic illustration of three different types of faradic mechanisms: (a) underpotential deposition, (b) redox pseudocapacitance, (c) intercalation pseudocapacitance. Reproduced with permission.[50] Copyright 2017, WILEY-VCH.

For pseudocapacitors, the energy is stored through the Faraday process, which is associated with the highly reversible surface or near-surface redox reaction of the active material at electrode/electrolyte interface.[39] Based on the capacitive features appearing in pseudocapacitors, there are three types of faradaic mechanisms (**Figure 1-8**).[87] Among them, the underpotential deposition involves the adsorption and reduction of metal ions or protons

on the surface of noble metal at a potential less negative than the equilibrium potential,[50,88] while the redox pseudocapacitance occurs on the surface of electrode material and is accompanied by ion adsorption and charge transportion.[89] Intercalation pseudocapacitance mainly comes from the cations which are intercalated into the host materials accompanied by a faradaic charge-transfer with no crystallographic phase change.[90] Typically, the charge state of the pseudocapacitive materials changes continuously with the potential because their electrical response is almost the same as that of the EDLCs.[39]

Among these reported materials, transition metal oxides/hydroxides and CPs are mostly used electrode materials with redox pseudocapacitive behavior. Notably, the electrode material for pseudocapacitors can be identified for an intrinsic pseudocapacitive material or an extrinsic pseudocapacitive material based on the characteristic of charge storage mechanism.[91, 92] For the intrinsic pseudocapacitive material, it exhibits pseudocapacitive behavior in a broad range of particle size and morphologies while for the extrinsic material it only appears the pseudocapacitive behavior under the nanosized material. [39] In addition, it is easy to distinguish pseudocapacitive materials and battery-type materials based on their different kinetics. As reported, the former is controlled by a surface-related process while the latter is forbidden by a diffusion-controlled process. [39, 92]

Furthermore, it is worth to mentioned that Faradic behavior accompanies with EDLC behavior in some pseudocapacitive materials. This means that the capacitance contribution of these materials is mainly from the pseudocapacitive charge storage mechanism, but there is still a small partial of the contribution from the double layer capacitance. Generally, the pseudocapacitive materials can provide higher capacitances than that of carbon materials, but they are greatly limited by their poor electrical conductivity and easily damaged

structure.[15,86] Consequently, the relatively poor rate capability and unsatisfactory cycle life are the major issues of pseudocapacitive materials. [39]

1.2.2.3 Hybrid capacitors

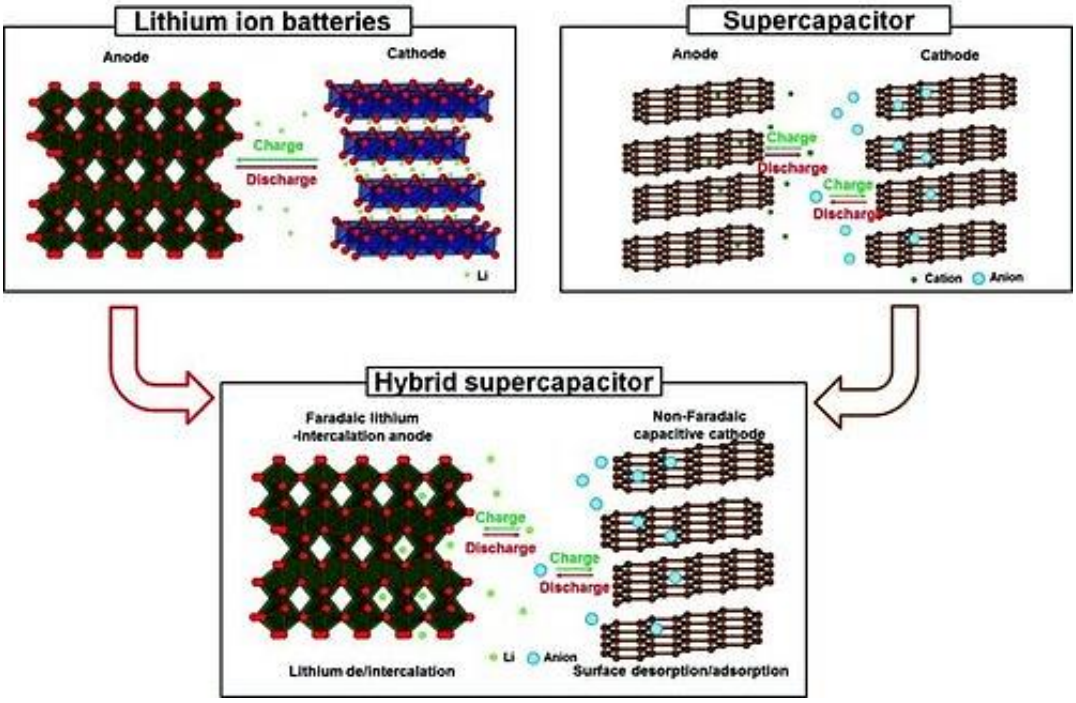

Figure 1-9 Illustration of configuration of lithium ion hybrid supercapacitors. Reproduced with permission.[97] Copyright 2010, WILEY-VCH.

Despite many efforts made, the energy density of conventional SCs is still unsatisfactory compared with that of batteries and fuel cells, which is due to its low specific capacitance and narrow operating voltage. In this context, hybrid capacitors as a new concept of capacitor have been proposed, which are consisted by a capacitor-type electrode storing the energy through electrostatic adsorption/desorption and a battery-type electrode

storing the energy through Faradaic reaction.[93-95] By combining the advantages of each part, hybrid SCs can achieve higher energy density than that of EDLCs without sacrificing power density and cycle life. A representative example of such an energy storage device is the lithium-ion hybrid supercapacitors (LIHSs) (**Figure 1-9**).[39] In the charge process of LIHSs, Li^+ from the electrolyte is inserted into the battery-type anode, thus delivering a higher capacitance, while at the same time anion such as PF^{6-} is stored at or near the surface of carbon-based cathode, thus enabling a high-power capability.[96]

Under these circumstances, it seems that LIHSs are a promising candidate to match these new demands of high-performance devices with both high energy and power densities. However, there are some critical problems which need to be solved before their practical applications. In general, the surface adsorption/desorption process (Cathode part) is much faster than the Li^+ intercalation/de-intercalation reaction (Anode part), thus the faradaic process is suppressed,[97] resulting in poor rate capability and low energy density. To address these issues, it is very necessary to develop new anode materials to overcome the sluggish kinetics of Li^+ diffusion in the bulk and the accompanying volumetric expansion during the intercalation/de-intercalation processes.[98] In this case, intrinsic high-rate battery anodes such as hard carbon, amorphous carbon, TiO_2, $Li_4Ti_5O_{12}$, and Nb_2O_5 have been employed as LIHSs anodes.[96, 99] Particularly, their performance can be further improved by combining the above alternative anode materials with advanced carbonaceous materials (e.g., graphene, amorphous carbon, and CNTs).[97, 100] On the other hand, the capacitor-type cathode (e.g., AC, CNTs, graphene) suffers from low energy density because of inappropriate pore size distribution and limited charge storage.[97, 101] In a word, the unsatisfactory electrochemical

performance of LIHSs (e.g., the relatively low energy density and the poor cycle stability) are mainly attributed to the different energy storage mechanism in the capacitor-type cathode and the battery-type anode as well as the imbalance of charge-storage capacity between them. In this case, the development of high-performance capacitor-type cathode materials and anode materials is an effective and straightforward strategy to achieve high-performance LIHSs.

1.3 Motivation and organization of thesis

Owing to their unsatisfactory electrochemical performance (e.g., low energy density, short cycle life for pseudocapacitors) and their intrinsic drawbacks (e.g., large size, heavy weight, and rigid nature), traditional SCs are not suitable for these new and higher requirements of electric vehicles and next-generation consumer electronics, especially portable/wearable electronic devices. To address these challenges and meet these new requirements, it strongly depends on the development of new concept SCs by adopting new synthesis and preparation techniques, exploring new alternative electrode materials, and innovating the configuration of devices. In this case, this thesis is thereby motivated by these strong desires to design and construct novel and high-performance SCs with unique electrode structure and configurations. In addition, the corresponding literature review and research progress of each project (e.g., LIHSs, fiber-shaped MSCs, in-plane MSCs) has also been summarized in the introduction part in **Chapter 3-5**, which helps to understand the significance of our projects and the contribution we made.

The main objectives of this thesis are described as follows: (1) synthesize advanced electrode materials by rational design and assembly for the construction of novel high-

performance SCs; (2) adopt the new configuration by combining the different energy storage mechanism of the anode and cathode materials to boost the electrochemical performance of SCs; (3) reveal the structure-property-performance relationship of these new nanomaterials and understand the underlaying reason behind the excellent electrochemical performance as well as the capacity decay; (4) contribute to some innovative solutions for the development of new-concept and next-generation SCs. Therefore, much attention of this thesis has paid to the rational synthesis of electrode materials, the design and assembly of the devices, and the physical and chemical characterization of related nanomaterials as well as corresponding electrochemical performance evaluation. The breakdown of the project tasks in this thesis is shown in **Figure 1-10**.

In a short, the whole thesis includes six chapters, and the brief description of each chapter is shown as follows. **Chapter 1** introduces some general ideas of SCs related to the background, fundamental, current research progress, challenge and motivation as well as scope of the thesis. **Chapter 2** lists some important characterization and measurement techniques used in the thesis, with in depth discussion provided in subsequent Chapter 3-5. **Chapter 3** mainly focuses on the improvement of the performance of SCs by innovating the design of new lithium ion hybrid capacitors and combining the rational design and assembly of nanocomposite materials. **Chapter 4** introduces a proof-of-concept of a fiber-shaped MSCs, especial the strategy for the construction of flexible fiber-shaped electrode. Meanwhile, the electrochemical performance of the obtained device and its corresponding mechanical flexibility are evaluated. **Chapter 5** highlights a new and effective strategy for the design of in-plane MSCs constructed by 2D quantum dots for both positive and negative electrode materials. The electrochemical performance of the positive electrode and negative

electrode as well as the device are investigated, while at the same time the reasons behind the excellent electrochemical performance are revealed in depth. Finally, **Chapter 6** summarizes the important results and conclusions achieved and some personal ideas on the future direction that the work may continue to investigate.

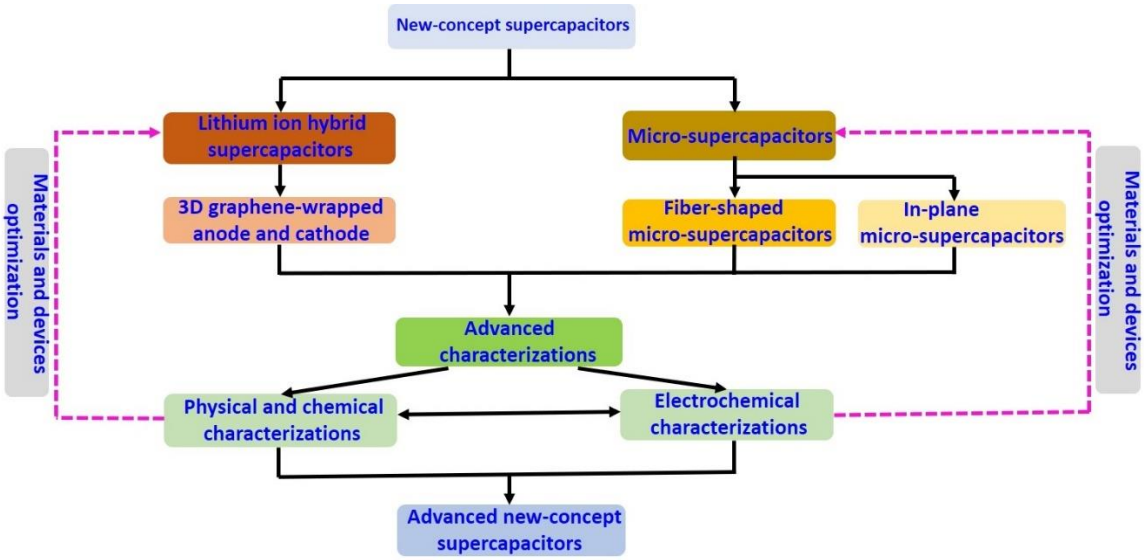

Figure 1-10 Schematic of the project workflow.

Chapter 2: Characterization techniques

In this chapter, some advanced characterization techniques including physicochemical techniques and electrochemical techniques are briefly introduced. The former mainly include scanning electron microscopy (SEM), transmission electron microscopy (TEM), Raman spectroscopy, X-ray powder diffraction (XRD), X-ray photoelectron spectroscopy (XPS), energy-dispersive X-ray spectroscopy (EDS), gas sorption analysis, which are used to study the unique morphology, structure and composition of the obtained intermediate and final product as well as the sample after electrochemical testing. These essential and important characterizations facilitate to understand the structure-property-performance relationship of these electrode nanomaterials and reveal the underlaying reason behind the excellent electrochemical performance. The electrochemical techniques such as cyclic voltammetry (CV), chronopotentiometry (charge/discharge curves), chronoamperometry, electrochemical impedance spectra (EIS) are employed to investigate the electrochemical reaction, mechanism and kinetics of the electrode materials as well as the possible failure mechanism. In a word, these advanced characterization techniques presented here could provide more detail information about the electrode materials as well as the devices, which are beneficial for the understanding of the fundamental scientific knowledge of the electrode materials.

2.1 Physicochemical characterization

Physicochemical techniques applied in the projects are used to study the key microstructural features of electrode materials such as chemical composition, crystallinity,

surface topography, shape, grain size, porosity, which have significant impacts on the properties as well as electrochemical performance. Therefore, it is very necessary to investigate the electrode materials with these advanced techniques, thus qualifying these electrode materials for use in SCs. In this case, some basic principle and knowledge associated with these techniques are briefly introduced in this section.

2.1.1 Scanning electron microscopy (SEM)

As a widely used technique, SEM is employed to investigate the morphology and microstructural feature of nanomaterials. The SEM principle is based on capturing different signals emitted from the surface of the sample when the electrons interact with the sample. Among them, secondary electron-based imaging is the most commonly used because the volume of interaction with the sample is the shallowest and smallest, and has high resolution and magnification.[102] Except for the information of morphology and surface microstructure, SEM combining with the EDX apparatus can also identify the chemical components of materials. In this thesis, SEM is employed to characterize the nanostructure, composition and morphology of electrode materials and intermediates as well as the assembled devices.

2.1.2 Transmission electron microscopy (TEM)

Transmission electron microscopy (TEM) is an indispensable tool to reveal the physical properties, structure, and composition of nanomaterials in the size range of few nanometers to hundred nanometers. When the electron beam passes through the sample, it interacts with the sample to obtain TEM image, which is enlarged and focused by the objective lens.

It should be emphasized that various characteristics of the material can be obtained by TEM characterization through proper analysis. First, it is easily to determine the shape, size,

and surface morphology of the sample. Moreover, since the acceleration voltage of TEM (100-300 kV) is higher than that of SEM (5-20 kV), TEM can provide a higher resolution image of nanomaterial than SEM, thus beneficial for the study of the inner or ultra-fine nanostructure and providing more detailed structure information (e.g., defects, dislocations, voids). Additionally, when used in combination with other spectroscopic methods (such as EDS) incorporated in TEM, it can be conducted to check the elemental composition and examine the chemical bonding of materials. Besides, the selected area electron diffraction (SAED) pattern obtained from TEM is performed to study the crystal structure of nanomaterials.

2.1.3 Energy dispersive X-ray spectroscopy (EDS)

Energy dispersive X-ray spectroscopy (EDS) is a chemical analysis technique, usually integrated with SEM and TEM, to analyze the elemental components as well as their corresponding contents in sample. Basically, EDS detects the characteristic X-rays emitted from the sample during electron beam bombardment. When the electron at the outer energy level jumps into the electron hole at the lower energy level after the pristine electron is ejected by the electron beam. Therefore, based on the characteristic X-rays obtained, EDS is employed to identify the elements. Additionally, by combining with other image techniques, it can also be used to investigate the distribution of elements, especially the samples with unique structure and morphology.

2.1.4 X-ray photoelectron spectroscopy (XPS)

X-ray photoelectron spectroscopy (XPS) as a surface analysis technique (with the depth less than 10 nm from the surface) is performed to quantitatively characterize the elemental

component and chemical state of the elements in the sample. The basic principle of XPS is to irradiate the sample with monochromatic X-rays, resulting in the emission of photoelectrons, and then the binding energy of which are measured. Since each element (except hydrogen and helium) has its own characteristic peak in XPS spectrum, the energy and intensity of these peaks can be used to identify the element in different chemical environments and oxidation states. Particularly, the variation in binding energy, satellite peak, and multiple splitting are the most common features observed in XPS spectroscopy, reflecting changes in the oxidation states. In addition, XPS can also be performed to identify impurity in materials.

2.1.5 X-ray powder diffraction (XRD)

X-ray powder diffraction (XRD) is considered to be a quick and easy technique to identify the crystal structure, unit cell, and atomic spacing of nanomaterials. When the monochromatic X-rays from the cathode ray tube interact with the sample, the XRD pattern can be obtained only when the crystal plane spacing and interference condition in the powder satisfy Bragg's Law:

$$n\lambda = 2d\ sin\theta \qquad (2\text{-}1)$$

where n is the order of the spectrum, λ is the wavelength of incident X-rays, d is the spacing between diffracting planes, and θ is the diffraction angle. By comparing with the standard diffraction pattern, the chemical composition of the resulting production can be easily identified. Furthermore, the average particle size can also be obtained from the XRD pattern with the assistance of Scherrer–Debye equation.

2.1.6 Raman spectroscopy

Raman spectroscopy is an analytical characterization technique widely used in the chemical and physical science to study nanomaterials and nanoscale surfaces. Raman spectroscopy uses a phenomenon called the Raman effect, which occurs when the electric dipole of a molecule interacts with a photon. This interaction utilizes the inelastic scattering of light, which can be used to determine the composition and properties (e.g., phases, crystalline, defect, size, shape) of the sample. In this thesis, Raman spectroscopy is used to study the defects of graphene and its derivatives as well as other electrode materials.

2.1.7 Gas adsorption analysis

Gas adsorption analysis is a very common method for measuring the specific surface area and determining the pore size of nanomaterials, which is based on the adsorption characteristic of gas on solid surfaces. According to the theoretical model of gas adsorption, the specific surface area and pore-size distribution of nanomaterials can be obtained. An adsorption-desorption isotherm is usually obtained by plotting the volume of gas adsorbed *vs.* the relative pressure. According to the Brunauer-Emmett-Teller (BET) theory, the specific surface area of the sample can be obtained by supposing the monolayer of gas molecules when the relative pressure is in the range of 0 to 1. According to the shape of adsorption-desorption isotherm, the pore structure could be classified and identified: micropores (< 2 nm), mesopores (2 - 50 nm), and macropores (≥ 50 nm). Obviously, gas adsorption analysis is a very useful characterization technique to obtain some important physical and chemical information of samples.

2.2 Electrochemical characterization

Electrochemical characterization is conducted to reveal the electrochemical behavior of the electrode materials under different electrochemical conditions. Currently, steady-state and transient techniques are carried out to investigate the electrochemical properties of electrode materials. Particularly, in transient experiments, the electrochemical system is disturbed from the steady state, and the relaxation of the response (e.g., current, potential, charge, impedance) of the system is detected as a function of time, which can be used to understand the basic electrochemical principles, such as charge transfer, ion diffusion, and interfacial behavior. In this thesis, several classic electrochemical characterization techniques such as cyclic voltammetry (CV), galvanic charge/discharge (GCD) and electrochemical impedance spectroscopy (EIS) are used to evaluate the performance of electrode materials and devices as well as the energy storage mechanism.

2.2.1 Electrochemical testing systems

Generally, there are two kinds of electrode testing system in electrochemical cells: three-electrode system and two electrode system. For a three-electrode system (**Figure 2-1**), the prepared electrode is served as working electrode, while the saturated calomel electrode (SCE) and platinum electrode (Pt) are used as reference electrode and counter electrode, respectively. Here, it should be mentioned that the active materials (such as powder materials) are coated on the current collector (e.g., nickel foam, gold foil, stainless steel foil/mesh) or directly used as a working electrode (e.g., graphene foam/film, other free-standing electrodes). The electrolyte may be aqueous solutions, organic solvents and ionic liquids as well as gel electrolytes, which depend on the electrode materials and the research

systems. For a two-electrode system (**Figure 2-1**), it consists of two electrodes (cathode and anode) with a separator in between, which is saturated with the electrolyte. Here, it should be mentioned that the detail electrode preparation process and testing condition are described in experimental part in each chapter.

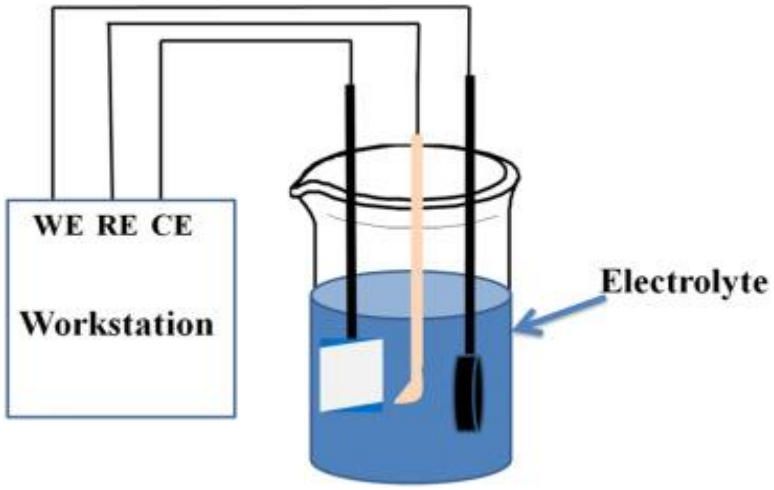

Figure 2-1 Illustration of three-electrode system for electrochemical performance characterization. Reproduced with permission.[103] Copyright 2017, Elsevier.

2.2.2 Electrochemical performance evaluation

In order to evaluate the electrochemical performance of electrode materials or devices, several important parameters need to be defined, including specific capacitance, operating voltage, equivalent series resistance, power density, energy density. Currently, there are multiple methods to calculate these parameters, but in this section, we will introduce the most common methods based on cyclic voltammetry (CV), galvanic charge/discharge (GCD) and electrochemical impedance spectroscopy (EIS).

2.2.2.1 Cyclic Voltammetry (CV)

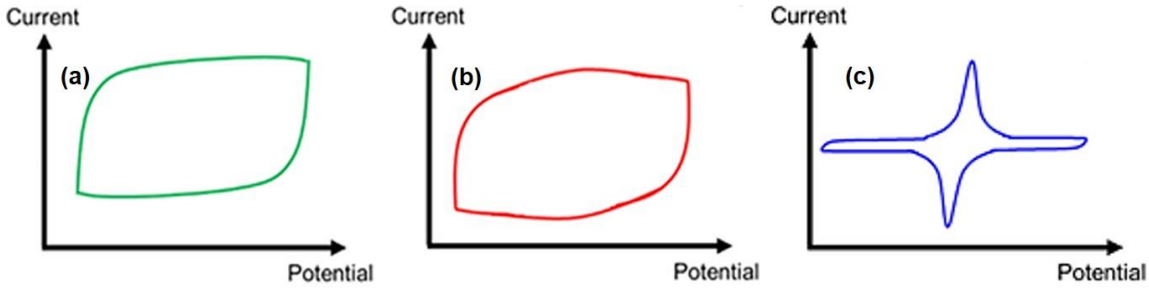

Figure 2-2 Schematic of CV curves of electrode materials with different electrochemical behavior: (a) electrical double layer capacitive behavior, (b) pseudocapacitive behavior, and (c) battery-like behavior, respectively. Reproduced with permission.[104] Copyright 2020, WILEY-VCH.

Cyclic voltammetry (CV) is a potentiodynamic electrochemical measurement technique used to analyze the redox characteristics of samples. The CV measurement is done by linearly sweeping the potential of the working electrode at a certain scan rate within the desired potential window, then it is swept in the opposite direction back to the initial potential. Typically, the CV curve of ideal supercapacitor is a perfect rectangle shape, but most CV curves always deviate from the ideal shape because of the existing of redox reactions on the interface (**Figure 2-2**). In this case, it is easy to judge the capacitor behavior of SCs based on the shape of CV curve. Moreover, the shape of the CV curve, especially the peaks and peak locations, provides key insight into the characteristic of the material's redox property (such as oxidation/reduction). In addition, CV can also be used to evaluate the cycle life of SCs and calculate the specific capacitance (C) based on the following Equation:

$$C = \frac{1}{v \cdot m \cdot (V_f - V_i)} \int_{V_i}^{V_f} I(V)\, dV \qquad (2\text{-}2)$$

Where *v*, *I*(*V*), *m*, *V* (*V* = V_f -V_i) are the scan rate ($mV \cdot s^{-1}$), the response current (A), the mass loading of active material (g), the potential window (V), respectively.

2.2.2.2 Chronopotentiometry (CP)

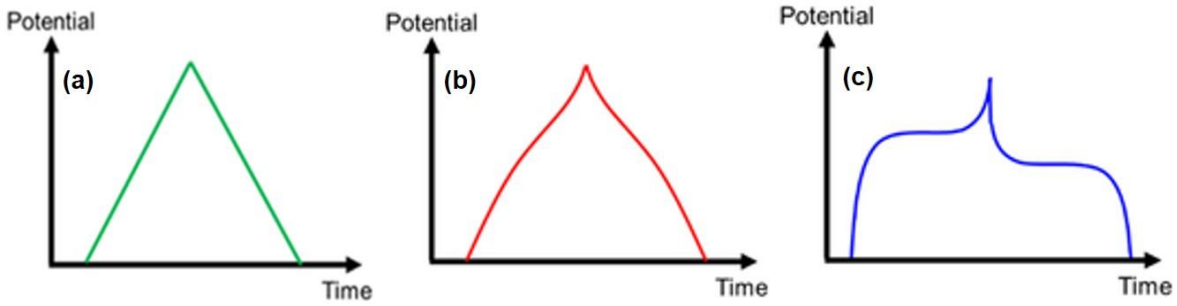

Figure 2-3 Schematic of charge/discharge profiles of electrode materials with different electrochemical behavior: (a) electrical double layer capacitive behavior, (b) pseudocapacitive behavior, and (c) battery-like behavior, respectively. Reproduced with permission.[104] Copyright 2020, WILEY-VCH.

In chronopotentiometry (CP), there is an applied current pulse to the working electrode while its corresponding potential relative to the reference electrode is measured as a function of time. Notably, the electrode potential changes linearly with time (**Figure 2-3**) when a constant anode/cathode current is applied to the electrode. This technique can be employed not only to study the mechanism and kinetics of the chemical reactions, but also as a general-purpose galvanostatic technique in many applications, such as electroplating and measuring the charge/discharge curves of supercapacitors (or batteries). Based on the CP test, the specific capacitance (C) can be measured by Equation 2-3:

$$C = \frac{I \cdot \Delta t}{m \cdot \Delta V} \qquad (2\text{-}3)$$

Meanwhile, the energy (E) and power (P) densities are calculated based on Equation 2-4 and Equation 2-5, respectively:

$$E = \frac{C \cdot \Delta V^2}{7200} \quad (2\text{-}4)$$

$$P = \frac{E \cdot 3600}{\Delta t} \quad (2\text{-}5)$$

Where I, Δt, ΔV, and m are the current density ($A \cdot g^{-1}$), the discharge time (s), the voltage (V), and the mass loading (g), respectively.

It should be mentioned that, the specific capacitance is associated with many parameters, such as current density, mass of active material, voltage and discharge time. Furthermore, the capacitor behavior of the electrode material can be judged by the symmetry of the charge/discharge curve, where the more symmetric the curve, the better the capacitor behavior of the electrode material. Besides, the cycle stability of the electrode or device can also be evaluated through multiple cycles of the constant current charge/discharge process.

2.2.2.3 Electrochemical impedance spectroscopy (EIS)

Electrochemical impedance spectroscopy (EIS) is another useful technique that uses small amplitude alternating current signals to detect the impedance characteristics of a cell. The alternating current signal is scanned over a wide frequency range to generate an impedance spectrum for the electrochemical cell under test. Here, the amplitude of the excitation signal is very small so that the system is almost in the equilibrium state. In this case, EIS technique is employed to evaluate the electrochemical system (e.g., supercapacitors, batteries, fuel cell, photovoltaics, and coating) without being significantly affected. Many important parameters including the equivalent series resistance, charge transfer kinetic and ion diffusion process as well as frequency response can be reflected by

Nyquist plot and Bode plot (**Figure 2-4**). The values of these elements can be obtained by equivalent circuit simulation.

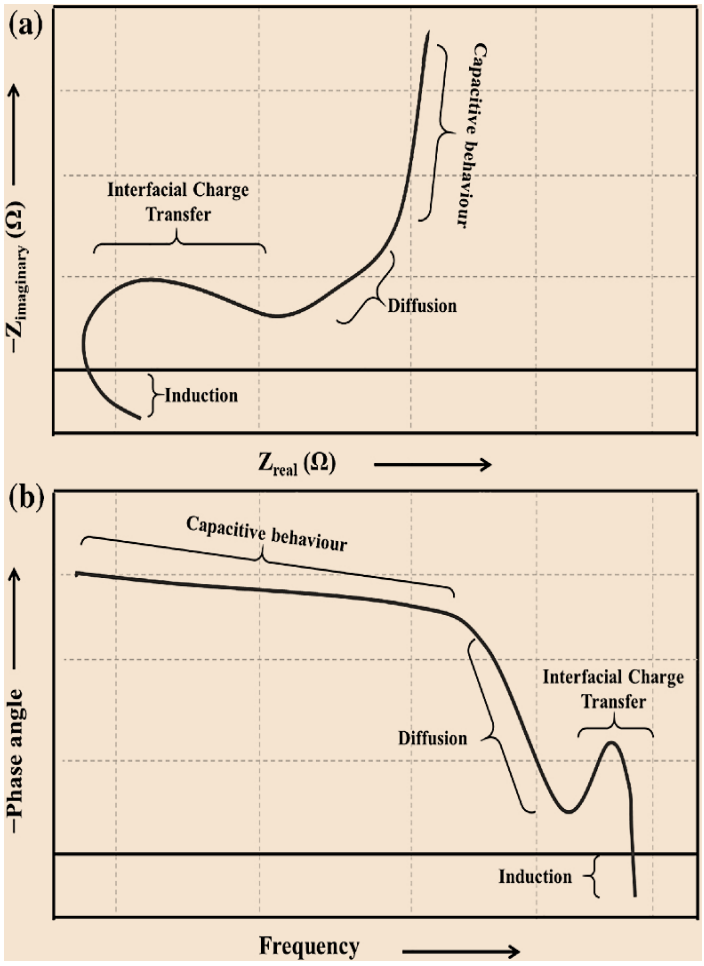

Figure 2-4 Schematic of (a) Nyquist and (b) Bode plots of SCs. Reproduced with permission.[105] Copyright 2018, Springer.

2.2.2.4 Cycle stability

Cycle stability is also an important parameter for evaluating the practical application of SCs. It should be mentioned that one cycle means the electrode or device is fully charged/discharged at a constant current density. In laboratory-scale testing, thousands of

cycles are performed to evaluate cycle stability. Particularly, it is easy to judge the cycle stability of the electrode or device by comparing the initial capacitance and the corresponding capacitance after the cycling test. Generally, electrical double layer capacitive materials (e.g., AC, CNTs) storing charges physically at the surface of the electrodes allow SCs to exceed the cycle life of batteries (a few thousand cycles), while pseudocapacitive materials (e.g., metal oxides, CPs) storing the energy by highly reversible redox reactions leads to unsatisfactory cycle stability. [39] It is expected that the as-prepared electrode materials exhibit excellent cycle stability, but the capacitance of the material usually decays after thousands of cycles to some extent, which may be due to many reasons such as structure change, corrosion of the electrode materials, electrolyte decomposition.

2.2.2.5 Self-discharge

Self-discharge performance is another important parameter that should be considered in the real applications of SCs. Self-discharge of the SCs is associated with the spontaneous decrease of the voltage or capacity when the SCs is not connected to any electric load. Here, the charged SCs are in the high-energy state, so the self-discharge driving force mainly comes from thermodynamic instability. Generally, there are three self-discharge mechanisms for SCs: diffusion control process, potential driving process, and ohmic leakage, respectively. [106] Obviously, all these self-charge process will result in a decrease in open circuit voltage and a degradation of the energy stored in SCs. As reported, the diffusion control process is related to the movement of the electrolyte ions adsorbed on the electrode materials because of the concentration gradient at the electrode/electrolyte interface, which can be described as the following equation: [106, 107]

$$V = V_{initial} - m \cdot t^{1/2} \quad (2\text{-}6)$$

The potential driving process is arising from the redox reaction at the electrode/electrolyte interface because of the impurity of electrolyte or the overcharge of electrode, which obeys the following equation: [106, 107]

$$V = V_{initial} \cdot e^{-t/\tau} \quad (2\text{-}7)$$

Additionally, the ohmic leakage is caused by the internal resistance between the anode and cathode electrodes, which is based on the following equation: [106, 107]

$$V = V_{initial} \cdot e^{-t/RC} \quad (2\text{-}8)$$

Where V, $V_{initial}$, m, t, τ, R, and C are the voltage of SCs, the started voltage of self-charge, the diffusion parameter, the storage time, the time constant, the ohmic resistance, and the capacitance of SCs, respectively.

The self-discharge behavior is dependent on many factors, such the surface state of electrode (e.g., the element valence, functional groups, impurities), electrolyte, separator, and operating condition (e.g., temperature, humidity) as well as manufacturing technology.[106, 107] Currently, many strategies are employed to solve the self-discharge behavior, such as modifying electrodes, using ion-exchange membrane as separator, introducing surfactants into electrolyte,[107] but there are still huge challenges to explore effective methods to reduce the self-discharge of SCs and improve their applications. It is worth mentioning that the self-discharge behavior of SCs is not discussed in this thesis because we mainly focus on the design of advanced electrode materials and devices, but it will be investigated in future work.

Chapter 3: Design and construction of high-performance Li-ion hybrid supercapacitors based on 3D graphene-foam composites

This chapter is reprinted from the manuscript published in *ACS Applied Materials & Interfaces*.

W. Liu, J. Li, K. Feng, A. Sy, Y. Liu, L. Lim, G. Lui, R. Tjanda, L. Rasenthiram, G. Chiu, A. Yu. "Advanced Li-ion hybrid supercapacitors based on 3D graphene−foam composites". *ACS Appl. Mater. Interfaces*, **2016**, *8*, 25941-25953.

3.1 Introduction

Currently, energy storage and conversion technology has become a key research and development focus because of fossil energy depletion and global warming.[108, 109] Additionally, the growing complexity of portable electronic devices and emerging popularity of electric vehicles have greatly boosted the new demand for more advanced energy storage devices.[110] However, the development of energy storage devices lags behind these new and high demands. Recently, Li-ion hybrid supercapacitors (LIHSs) have been proposed as a new type of energy storage device, [111, 112] which is expected to enhance both energy and power densities based on the synergistic effect of a battery-type anode and a capacitor-type cathode. To date, numerous efforts have been devoted to constructing the LIHSs of which the majorities are constituted by a battery-type anode (such as TiN, VN, Nb_2O_5, and $Li_4Ti_5O_{12}$) and an active carbon (AC) cathode.[113-120] However, the obtained performances of these devices are still unsatisfactory, because the synergistic effect based on

the anode with high energy storage and the cathode with high power delivery is limited in this asymmetric configuration due to their different storage mechanisms.[112, 121, 122] In this case, it is very necessary to design new anode and cathode materials with excellent electrochemical performance using facile method while organically combining the advantages of both these anode and cathode materials to endow the as-obtained LIHSs with desirable electrochemical performance.

As reported, metal oxides, such as Fe_2O_3, [123] V_2O_5, [124] SnO_2, [125] Co_3O_4, [126, 127] TiO_2 [128, 129] and MoO_3 [130, 131] are popularly used as anode materials due to high theoretical capacity, low cost, abundance in nature, and environment friendly. In particular, MoO_3 has a unique layered structure, which provides facile access of ions and allows intercalation and storage of a large number of ions in its lattice.[130, 131] Nevertheless, its poor conductivity and local structural collapse during charge/discharge process result in poor kinetics and/or a serious capacity fading after several tens of cycles, especially under high current density.[110, 130-133] To address these issues, one effective and practicable strategy is to prepare nanostructured active materials with desirable morphology and size, especially one-dimensional (1D) nanobelt with a high aspect ratio which allows for fast lithium ion insertion and extraction while provide good electron transport between belts.[134-136] Additionally, the introduction of conductive carbon materials is regarded as another effective strategy to improve the electrochemical performance of metal oxides. Among the carbonaceous materials, graphene nanosheets (GNSs) have attracted tremendous attention due to its large specific surface area, high electrical conductivity, and excellent chemical and environmental stability.[137, 138] Particularly, three-dimensional (3D) graphene foam with well interconnected porous microstructure, high elasticity and mechanical stability, excellent electrochemical stability,

and high conductivity, is ideal to serve as the scaffold for the fabrication of hybrid electrodes.[139, 140]

Unlike that of research activities in anode materials, very little effort has been devoted to developing new cathode materials. However, the energy density of LIHSs is mostly limited by the cathode part in the asymmetrical configuration due to the enormous discrepancy between the specific capacity of cathode and anode. Therefore, exploiting alternative cathode materials, which can be appropriately coupled with the main advantage of anode materials to deliver high energy and power densities, is also highly desired. Very recently, nitrogen-doped carbon materials derived from nitrogen-enriched precursors are considered as promising candidates due to their excellent electrical conductivity and the co-contribution of capacitance from both electrical double layer and faradic reactions.[141, 142] Among the nitrogen-enriched precursors, polyaniline (PANI) is one of promising conductive polymer to produce nitrogen-doped carbon attributed to its simple synthesis, good chemical stability, and high content of nitrogen. [141, 142]

Based on the abovementioned considerations, in this work, 3D MoO_3/GNSs foam and 3D PANI/GNSs foam derived carbon are successfully prepared and employed as the anode and cathode material of the LIHSs (**Figure 3-1**), respectively. From the viewpoint of material design, it is expected to effectively take advantage of each component and endow the composite materials with more new functions based on the synergistic effects. Encouragingly, the rational design of the continuous network structure makes 3D MoO_3/GNSs foam and 3D PANI/GNSs foam derived carbon as the promising candidate for anode and cathode material, respectively. First-principle calculation is carried out to yield insights into the origins of the enhanced electrochemical performance of 3D MoO_3/GNSs

foam, which reveals that the introduction of GNSs dramatically reduces the diffusion energy barrier of Li^+. More importantly, by employing these two graphene foam-modified materials, the as-prepared LIHSs exhibits a wide operating voltage range (up to 3.8 V), a long-term cycle stability (with 90% capacity retention after 3000 cycles), and an improved high energy density of 128.3 $Wh \cdot kg^{-1}$ (with the power density of 182.2 $W \cdot kg^{-1}$), which also remains of 44.1 $Wh \cdot kg^{-1}$ at high power density of 13.5 $kW \cdot kg^{-1}$.

3.2 Experimental

3.2.1 Materials synthesis

Synthesis of 3D MoO_3/GNSs foam: All the chemical reagents were analytical grade and used as received without further purification. Graphene oxide (GO) was synthesized by a modified Hummers method. [143] The MoO_3 nanobelts (**Figure 3-1c** and **Figure 3-S1**) were synthesized according to the reported literature.[130]

The fabrication of 3D MoO_3/GNSs foam (**Figure 3-1e**) was as follows. Firstly, the dispersion of reduced graphene nanosheets (GNSs) was modified by positively charged poly(diallyldimethylammonium chloride) (PDDA). Then, MoO_3 nanobelts were added into the homogeneous positively charged GNSs dispersion. Next, the resultant solution was transferred to an autoclave kept at 200 °C for 12 h, and then cooled down to room temperature. The production was collected using centrifugation and dried under vacuum at 60 °C overnight. MoO_3/GNSs composites with different GO content (GO: MoO_3 ratios of 1:9, 2:8 and 3:7, respectively.) were prepared using the same procedure, and the as-prepared MoO_3/GO composite were denoted as MoO_3/GNSs-1, MoO_3/GNSs-2 and MoO_3/GNSs-3,

respectively. The weight percentage of GNSs in the MoO_3/GNSs composite was determined by calculating the TGA curve as shown in **Figure 3-S2**.

Synthesis of 3D PANI/GNSs foam derived carbon: The polyaniline (PANI) nanotube (**Figure 3-1d** and **Figure 3-S3**) was prepared by oxidative polymerization of aniline in aqueous solution.[144] A typical synthesis procedure of 3D PANI/GNSs foam derived carbon (**Figure 3-1f**) was as follows. First, 100 mg of the as-prepared PANI nanotube was dissolved in 25 mL of deionized water with ultrasonication for 15 min. Second, the obtained dispersion was poured into a beaker containing graphene oxide solution with moderate stirring, and then transferred to an autoclave kept at 180 °C. After the reaction was complete, the resultant precipitate was filtered with ethanol-washing, followed by drying under vacuum at 60 °C. Then, PANI/GNSs composite were pyrolyzed at 800 °C under argon atmosphere. Afterward, the obtained sample was impregnated using KOH aqueous solution and then treated at 700 °C under argon atmosphere. After being cooled down to room temperature, the obtained sample was neutralized by 5% HCl solution followed by drying at 60 °C. PANI/GNSs sample with different GO content (GO: PANI ratios of 1:19, 1:9 and 2:8, respectively.) were prepared using the same procedure but with different amounts of GO. The GO content in the PANI/GNSs composite was 5, 10 and 20 wt%, and the sample was denoted as PANI/GNSs-1, PANI/GNSs-2 and PANI/GNSs-3, respectively.

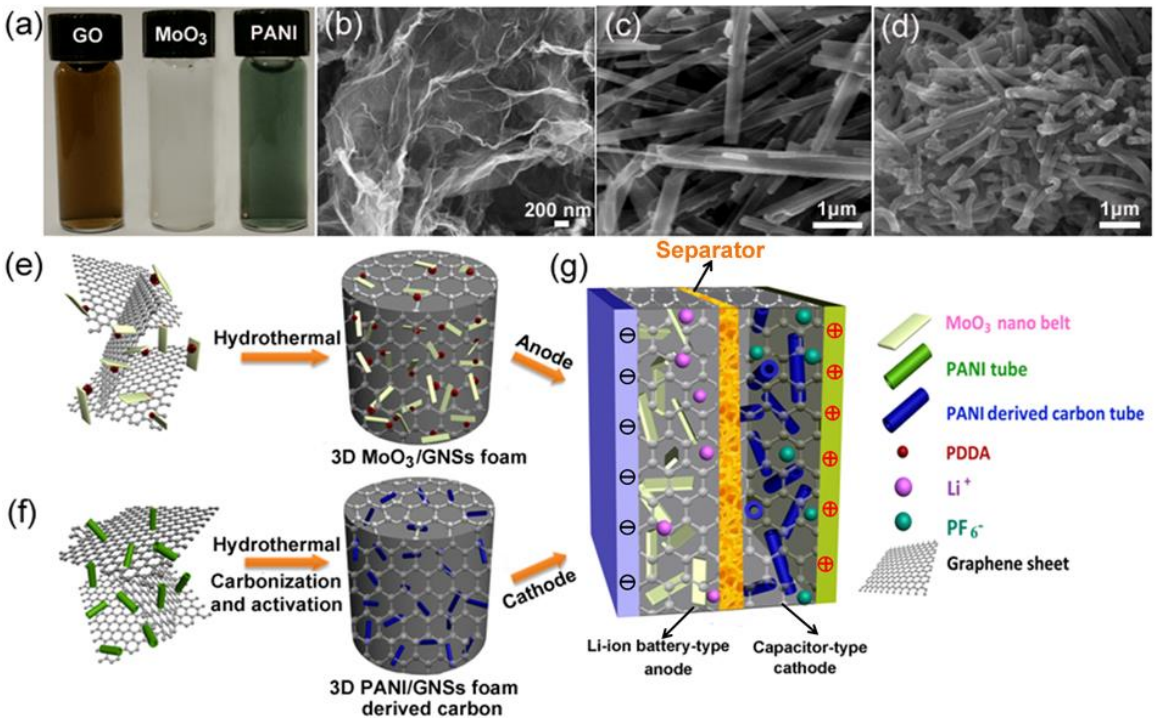

Figure 3-1 (a) Digital photograph of the as-prepared graphene oxide (GO), MoO_3 nanobelt, and PANI solution, respectively. SEM images of (b) GNSs, (c) MoO_3 nanobelt, and (d) PANI nanotube, respectively. Schematic illustration of the preparation of (e) 3D MoO_3/GNSs foam and (f) PANI/GNSs foam derived carbon. (g) Schematic of the charging mechanism of LIHSs constructed by 3D MoO_3/GNSs foam anode and 3D PANI/GNSs foam derived carbon cathode.

3.2.2 Morphological and structural characterization

The morphology of the obtained samples was characterized by a LEO 1350 field emission scanning electron microscope (SEM). Transmission electron microscopy (TEM) images were taken using a JEOL 2010F transmission electron microscope with an accelerating voltage of 100 kV. The phases and crystallite structures of the samples were characterized by X-ray diffraction (XRD, MiniFlex 600, Rigaku) with Cu Kα radiation source (λ=

0.154178 nm) in the 2θ ranging from 10 to 80°. The chemical compositions and states of the samples were investigated by X-ray photoelectron spectroscopy (XPS) on a Thermo Scientific K-Alpha spectrometer. Raman spectra were obtained on a Senterra Raman detection system (Bruker Optics) using a 532 nm laser. Nitrogen adsorption–desorption isotherm measurement was carried out on a Micrometitics ASAP 2020 volumetric adsorption analyzer at 77 K. Thermogravimetric analysis (TGA) was performed on a TA instrument Q500 system from room temperature to 800 °C with a ramp rate of 10 °C·min^{-1}.

3.2.3 Electrode preparation and electrochemical characterizations

The fabrication processes of anode and cathode electrode were as follows. The anode was prepared by mixing MoO_3/GNSs or MoO_3 active material, Super P carbon and polyvinylidene fluoride (PVDF) dissolved in N-methyl-2-pyrrolidinone (NMP) with a mass ratio of 80:10:10. Then, the obtained slurry was coated onto copper foil, and punched into circular discs. After being dried at 120 °C in a vacuum, the electrodes were transferred into a glove box for cell assembly. The mass of active materials was about 1-1.5 mg·cm^{-2}. For the cathode, 90 wt% PANI/GNSs derived carbon and 10 wt% polytetrafluoroethylene (PTFE) were mixed uniformly. Next, the mixture was pressed into thin sheet and punched into circular discs. After that, these obtained electrodes were dried at 120 °C in a vacuum and transferred into a glove box. Here, Al foil is used as the current collector of the cathode.

For half-cell test (coin cell), Li metal foil and 1 M $LiPF_6$ dissolved in 1:1 v/v mixture of ethylene carbonate/diethyl carbonate (EC/DEC) were used as the counter electrode and the electrolyte, respectively. LIHSs (coin cell) were assembled in glove box with pre-activated MoO_3/GNSs as anode and PANI/GNSs derived carbon as cathode using the same electrolyte,

and the mass ratio between cathode and anode was 14:1. Cyclic voltammogram (CV) tests were carried out on a VMP3 potentiostat/galvanostat (Bio-Logic LLC, Knoxville, TN) at different voltage ranges (0.01-3.0 V *vs.* Li/Li^+ for anode, 3.0-4.5 V *vs.* Li/Li^+ for cathode, and 0.0-3.8 V for hybrid cell, respectively). Galvanostatic charge/discharge test was performed by NEWARE BTS-CT3008 (Neware Technology, Ltd., Shenzhen, China) at different current densities with the same voltage range of CV test. EIS measurement was carried out on a CHI660D with an AC voltage of 5 mV amplitude in the frequency range of 100 KHz to 0.05Hz. All electrochemical measurements were performed at room temperature.

The specific capacitance ($C_{Specific}$) obtained from the CV curve was based on Equation 3-1:

$$C_{Specific} = \frac{1}{\nu \cdot (V_f - V_i)} \int_{V_i}^{V_f} I(V) dV \qquad (3\text{-}1)$$

The specific capacitance ($C_{Specific}$) was also calculated from the discharge curve by the Equation 3-2:

$$C_{Specific} = \frac{I \cdot \Delta t}{m \cdot (V_f - V_i)} \qquad (3\text{-}2)$$

The conversion between the specific capacitance and capacity was based on Equation 3-3:

$$C_{Capacity} = \frac{C_{Specific} \cdot (V_f - V_i)}{3.6} \qquad (3\text{-}3)$$

Meanwhile, the volumetric energy density (E) and power density (P) were defined based on Equation 3-4 and Equation 3-5, respectively:

$$E = \frac{C_{Specific} \cdot \Delta V^2}{3.6} \quad (3\text{-}4)$$

$$P = \frac{E \cdot 3600}{\Delta t} \quad (3\text{-}5)$$

where v is the scan rate ($mV \cdot s^{-1}$), V_f *and* V_i are the potential limits of the voltammetric curve, $I(V)$ is the voltammetric discharging current (A), I is the current density ($A \cdot g^{-1}$), m is the mass of the active material (g), $C_{Specific}$ is the specific capacitance ($F \cdot g^{-1}$), $C_{Capacity}$ is the capacity of the device ($mAh \cdot g^{-1}$), E is the energy density ($Wh \cdot kg^{-1}$) and P is the power density ($W \cdot kg^{-1}$).

3.2.4 DFT calculations

The simulation calculations were performed under density functional theory (DFT) using the BAND program, in which the Slater type triple-zeta polarization basis sets were used. The generalized gradient approximation functional of Perdew-Burke-Ernzerhof was used to deal with the exchange and correlation energy terms. The diffusion barriers of Li migration in GNSs and MoO_3/GNSs (GNSs with and without defect) composite were investigated by the nudged elastic band method. All calculations were performed with a 2 × 2-unit cell, and all atomic positions and lattice constants were optimized by the conjugate gradient method.

To model the experimental composite, the interface structure of graphene and the MoO_3 (010) surface is constructed. MoO_3 (010) surface is selected because it is one of the most exposed facets in MoO_3/GNSs composite, as confirmed by the XRD result (Figure 2f). The MoO_3 synthesized in this work have an orthorhombic lattice system of the space group P_{bnm} with lattice parameters: a = 3.962 Å, b = 13.867 Å and c = 3.696 Å. In the present study,

the bottom atomic layer of the slab was fixed in its bulk position, whereas the remaining atomic layers and the adsorbed species were set free to relax. Based on fully relaxed structure, potential curves along Li atom bulk diffusion pathway were calculated to evaluate the Li diffusion in the MoO_3/GNSs composite. Note that GNSs with and without defects were used in the present study for comparison. In order to describe the interactions between the MoO_3 and GNSs, the adhesion energy (E_{ad}) of GNSs on MoO_3 surface were defined by the following equation:

$$E_{ad} = E_{\mathrm{MoO_3-GNSs}} - E_{\mathrm{GNSs}} - E_{\mathrm{MoO_3}} \qquad (3\text{-}6)$$

where $E_{\mathrm{MoO_3-GNSs}}$, E_{GNSs}, and $E_{\mathrm{MoO_3}}$ are the energies of the MoO_3-bound to the GNSs structure, the GNSs, and the MoO_3, respectively.

3.3 Results and discussion

3.3.1 3D GNSs/MoO_3 nanocomposite as anode material

The morphology and microstructure of the MoO_3/GNSs-2 nanocomposite is identified by SEM, TEM, and XRD, respectively. **Figure 3-2a** show the digital photograph of as-prepared MoO_3/GNSs-2 nanocomposite with three-dimensional (3D) foam structure after the hydrothermal reaction. SEM image (**Figure 3-2b**) of MoO_3/GNSs-2 nanocomposite shows that the GNSs-MoO_3 nanobelts well interconnect with each other and form an open macrospores structure. This unique structure ensures good electrolyte accessibility during charge/discharge process. High-resolution SEM image (**Figure 3-2c**) shows that MoO_3 nanobelts have the widths of 100-200 nm and lengths of 1-4 μm, and are well wrapped by ultrathin GNSs, which facilitates to improve electric conductivity and suspend the stress from volume change of MoO_3 nanobelts during charge/discharge process to some extent.

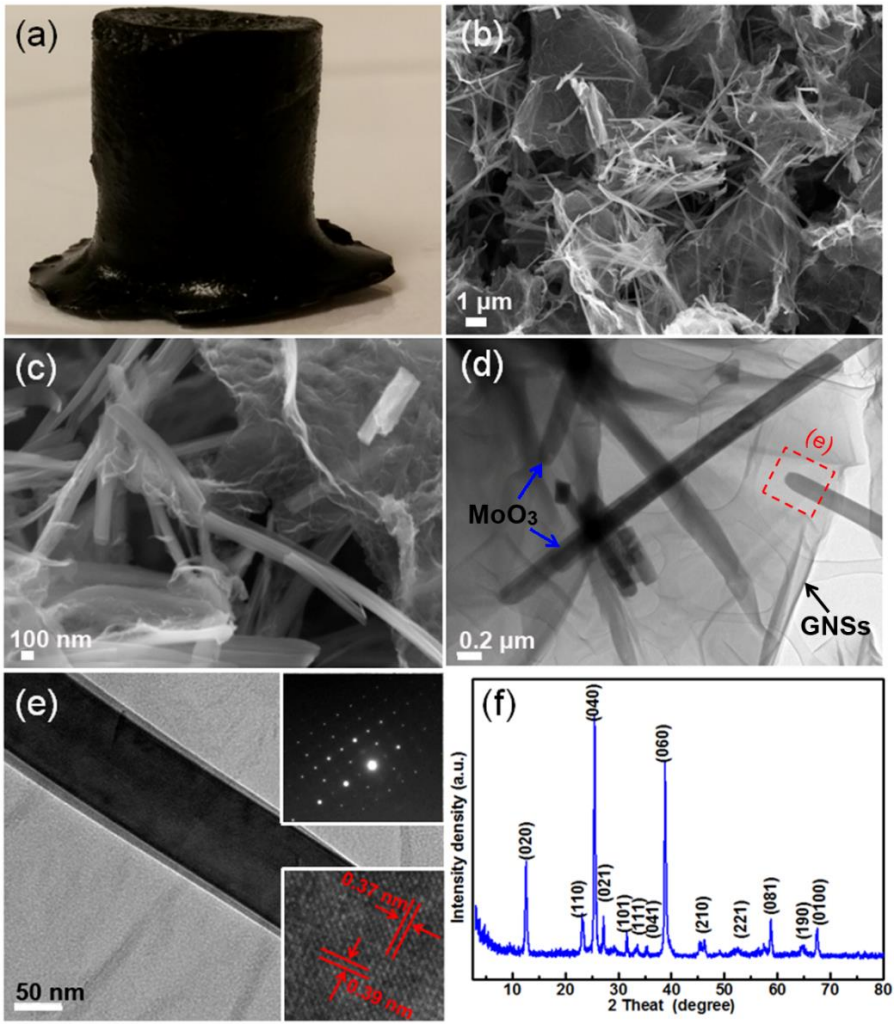

Figure 3-2 (a) Photograph, (b) low-magnification SEM image, (c) high-magnification SEM image, (d) low-resolution TEM image, (e) high-resolution TEM image, and (f) XRD spectrum of the as-obtained 3D MoO_3/GNSs-2 nanocomposite.

TEM image (**Figure 3-2d**) demonstrates that the MoO_3 nanobelts are firmly anchored by transparent and wrinkle GNSs after strong ultrasonic treatment, indicating a strong integration of MoO_3 nanobelts with GNSs, which benefits to the improvement of rate performance and cycling performance due to the good conductivity of GNSs. **Figure 3-2e** show the lattice fringe widths of 0.39 and 0.37 nm, corresponding to the (100) and (001)

planes of the orthorhombic MoO_3, [145-147] respectively. Selected area electron diffraction (SAED) (up inset in **Figure 3-2e**) reveals that the MoO_3 nanobelts have highly crystalline orthorhombic structure and prefer to grow along [001]. [145-147] X-ray diffraction (XRD) spectrum of the MoO_3/GNSs-2 nanocomposite is plotted in **Figure 3-2f**. No impurity peaks are detected, and all of the other diffraction peaks are attributed to the α-MoO_3 (JCPDS card No.05-0508), suggesting the high phase purity of the obtained MoO_3 nanobelts.[110, 148] Furthermore, no peaks of GNSs are observed, which may be due to the very low content of GNSs and the disordered distribution of GNSs in the MoO_3/GNSs-2 nanocomposite as well as the overlapping of the (002) diffraction peak of GNSs with the strong (040) diffraction peak of MoO_3 nanobelts.

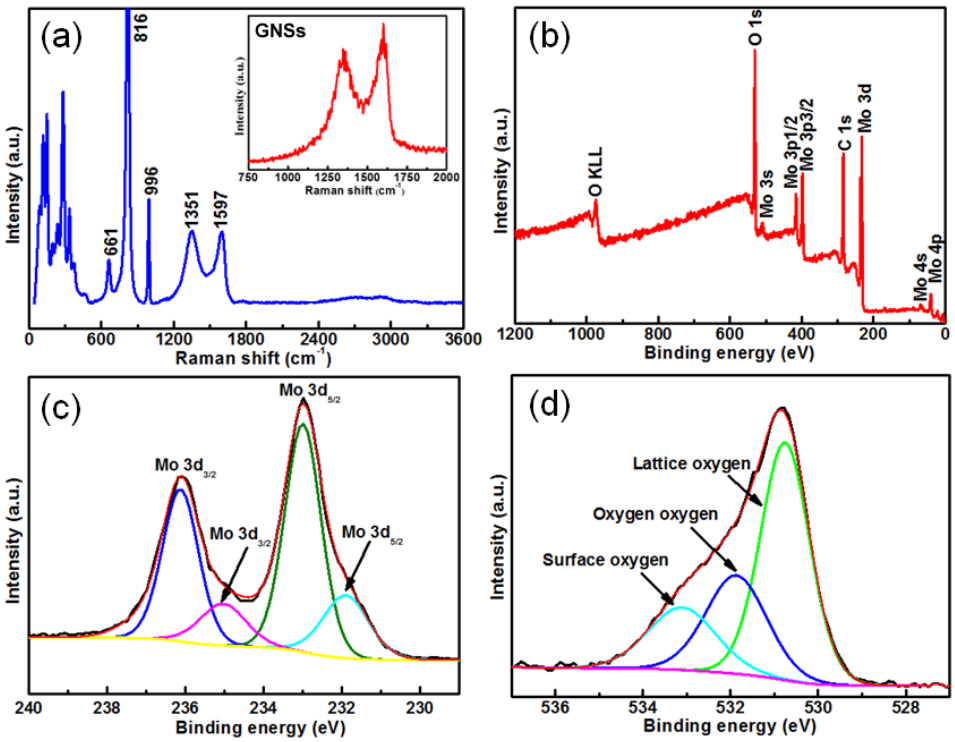

Figure 3-3 (a) Raman spectrum and XPS spectrum of the as-synthesized MoO_3/GNSs-2 nanocomposite: (b) survey, (c) Mo 3d, and (d) O 1s. Inset is the Raman spectroscopy of GNSs.

Raman and X-ray photoelectron spectroscopy (XPS) spectra are performed to further reveal the microstructure of the as-prepared MoO_3/GNSs-2 nanocomposite. **Figure 3-3a** shows the Raman spectrum of MoO_3/GNSs-2 nanocomposite. The characteristic peaks at 1350 cm^{-1} and 1581 cm^{-1} are attributed to the D and G bands of GNSs, respectively. Notably, the I_D/I_G ratio (1.06) of GNSs in the hybrid nanomaterial is slightly higher than that (0.86) of pure GNSs, demonstrating some other functional groups formed between GNSs and MoO_3 after hydrothermal reaction. Furthermore, except for the characteristic peaks of GNSs (D and G bands), other typical peaks at 995, 818, 666, 469, 377, 365, 336, 289, 245, 217, 195, and 157 cm^{-1} are in good accordance to those of α-MoO_3 reported elsewhere.[147, 149, 150] Additionally, the surface information and valence states of elements in the MoO_3/GNSs-2 nanocomposite are characterized by XPS. The survey spectrum (**Figure 3-3b**) shows the presence of Mo, C, and O elements in the as-prepared sample. Mo 3d spectrum is well fitted by two 3d doublets (**Figure 3-3c**), indicating the existence of two different chemical valences. The major peaks with the binding energy of 232.8 eV and 236.0 eV are attributed to the Mo^{+6}, [151] while other minor peaks with the binding energy of 231.8 eV and 235.0 eV corresponds to the Mo^{+5}. [152] As reported, the existence of Mo^{5+} is caused by the deficiency of O^{2-} in the crystal structure of MoO_3 and enhances its electrical conductivity.[133] The O1s peak of MoO_3/GNSs-2 nanocomposite is also fitted by the Gaussian distribution (**Figure 3-3d**). The binding energies at 530.1, 531.5, and 532.9 eV are related to the lattice oxygen, the chemically absorbed oxygen, and the oxygen vacancies, [149, 153] respectively. XPS result reveals the coexistence of adsorbed oxygen and lattice oxygen in the as-synthesized sample, which may enable MoO_3 nanobelts to strongly integrate with the GNSs through noncovalent bonding. Additionally, the MoO_3/GNSs-2 nanocomposite possesses a high specific

Brunauer–Emmet–Teller (BET) surface area of 33.7 $m^2 \cdot g^{-1}$ with the pore size ranging from several nanometer to several hundred nanometers (**Figure 3-S4**), which benefit to the increasing of the electrochemically active surfaces for the access of electrolyte ions. According to the above analysis, the MoO_3 nanobelts wrapped by ultra-thin GNSs, along with the improved conductivity and the unique 3D network structure would endow 3D MoO_3/GNSs-2 composite electrode with enhanced electrochemical performance as anode materials.

To investigate the electrochemical performance of the optimized 3D MoO_3/GNSs-2 composite electrode (**Figure 3-S5**), CV test is firstly performed at various scan rates from 0.1 to 100 $mV \cdot s^{-1}$ (**Figure 3-S6**). The broad cathodic and anodic peaks of 3D MoO_3/GNSs-2 composite at 1.26/1.32 and 2.17/2.25 V (**Figure 3-4a**) result from the reaction: $MoO_3 + 6Li^+ + 6e^- \leftrightarrow Mo + 3Li_2O$, which are attributed to Li^+ insertion/extraction and the phase transition process of Li_xMo alloy and MoO_3. [154] Moreover, it is observed that CV curves generally overlap after the first cycle (**Figure 3-S7**), indicating the good reversibility of lithium ion insertion/extraction in the MoO_3/GNSs-2 composite.

Generally, the current (*i*, A) follows a power-law relationship with the sweep rate (*v*, $mV \cdot s^{-1}$) at a fixed potential: [155, 156]

$$i = av^b \qquad (3\text{-}7)$$

where *a* and *b* are adjustable parameters. Based on the obtained value of *b*, it is feasible to distinguish between the capacitive contribution ($b = 1$) and the diffusion-limited contribution ($b = 0.5$). Therefore, the Li^+ intercalation kinetics could be analyzed by plotting log (*i*) *versus* log (*v*) for cathodic or anodic peak current. As shown in **Figure 3-4b**, the *b* value of the MoO_3/GNSs-2 composite is 0.85 for cathodic current peaks at the scan rates ranging

from 0.1 to 10 $mV \cdot s^{-1}$, indicating the kinetic of Li^+ insertion process in MoO_3/GNSs-2 nanocomposite is almost surfaced-controlled and quite fast with a typical capacitive behavior. To further distinguish quantitatively the total capacitor coming from the capacitive contribution and the diffusion-limited contribution, [157, 158] it is based on the following equation:

$$i = k_1 v + k_2 v^{1/2} \quad (3\text{-}8)$$

where k_1 and k_2 are suitable values. Obviously, the current at a fixed potential is a combination of adsorption/deabsorption process ($k_1 v$) and diffusion-controlled process ($k_2 v^{1/2}$). By plotting $i/v^{1/2}$ *versus* $v^{1/2}$, the value of k_1 and k_2 can be obtained by the slope of straight line and the corresponding intercept point with vertical axis, respectively, and then quantitatively evaluated the capacitive contribution and the diffusion-limited contribution in the total capacity of MoO_3/GNSs-2 nanocomposite (**Figure 3-S8).** Comparing the shaded area ($k_1 v$) with the experimental result (red solid line) in **Figure 3-4c**, it is noted that about 72% of the total current of the MoO_3/GNSs-2 nanocomposite comes from the capacitive energy storage mechanism. Although the diffusion-related charge storage increases with the decrease of scan rates (**Figure 3-4d**), it is still a relatively small portion of the total charge. Furthermore, it is observed that the specific capacity of the MoO_3/GNSs-2 nanocomposite gradually decreases with the increase of the current densities from 100 to 2000 $mA \cdot g^{-1}$ (**Figure 3-4e**), and quickly recovers with the current density back to 100 $mA \cdot g^{-1}$, illustrating the excellent rate capability and the good tolerance to the high charge/discharge current density. Additionally, the MoO_3/GNSs-2 nanocomposite displays 93% retention after 200 charge/discharge cycles and almost 100% Coulombic efficiency in each cycle (**Figure 3-4f**), indicating good cycle stability.

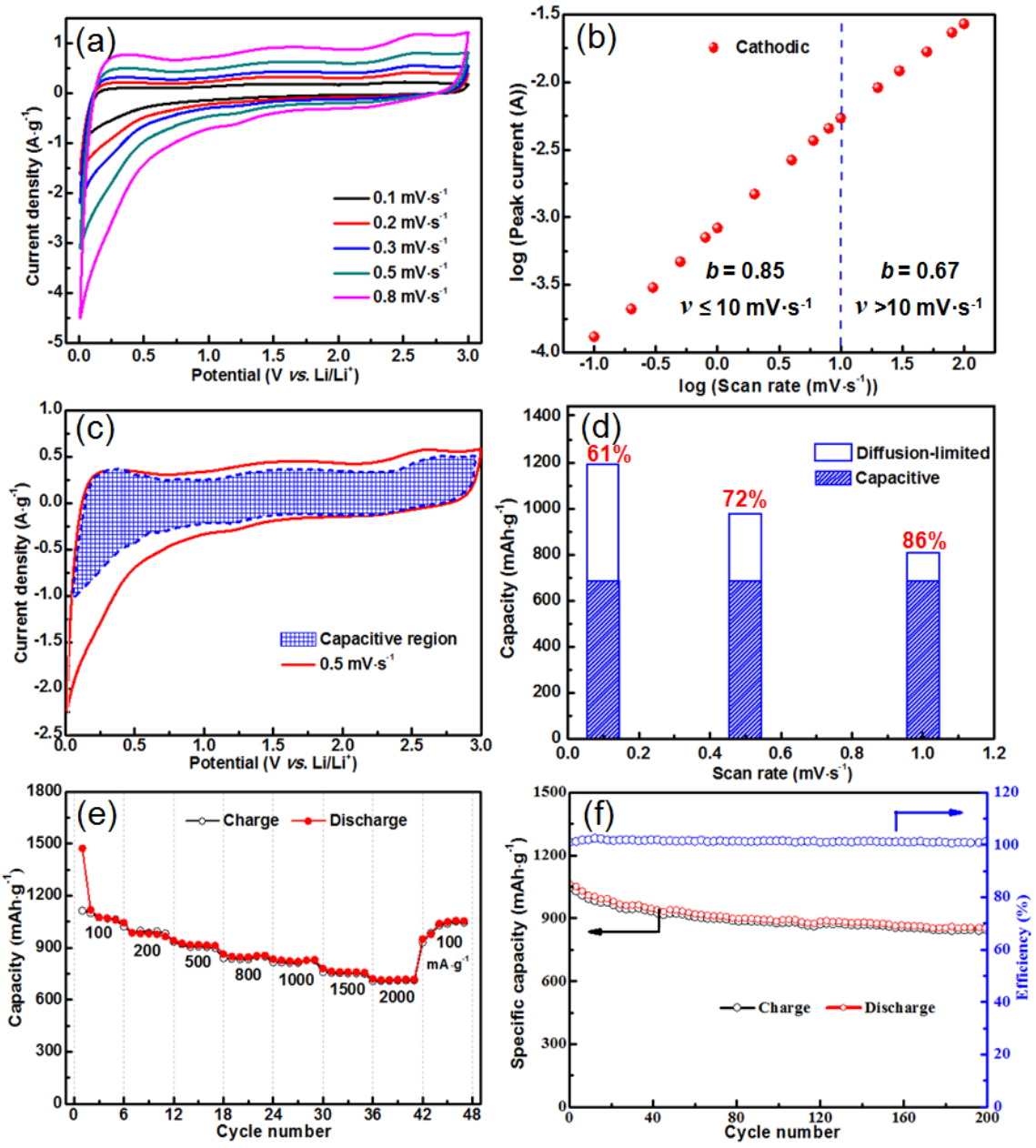

Figure 3-4 (a) CV curves of MoO_3/GNSs-2 composite tested at different scan rates, (b) determination of the *b* value of cathodic peak current with the scan rates from 0.1 to 100 $mV \cdot s^{-1}$, (c) CV curves with separation between total current (red solid line) and capacitive current (blue shaded region) at 0.5 $mV \cdot s^{-1}$, (d) the total capacitance of MoO_3/GNSs-2 composite derived from the capacitive and diffusion-limited elements, (e) rate capability at different current densities from 100 to 2000 $mA \cdot g^{-1}$, and (f) the corresponding cycle stability at 500 $mA \cdot g^{-1}$.

In order to explain the enhanced electrochemical performance of MoO_3/GNSs, we have investigated the diffusion process of Li atom in pristine MoO_3, MoO_3/GNSs-P (without defect), and MoO_3/GNSs (with defect), respectively. The adhesion energy for GNSs on MoO_3 is calculated to be -3.18 eV and -3.37 eV for MoO_3/GNSs-P and MoO_3/GNSs, respectively, indicating that the MoO_3/GNSs hybrid structures are quite stable. Here, we have considered three configurations of Li atom diffusion including Li atom first occupying surface adsorption site (A), subsurface insertion site (B) and the bulk insertion site (C). The optimized adsorption sites of Li atom in pristine MoO_3 and MoO_3/GNSs (GNSs with and without defect) composite and their relative diffusion barriers are plotted in **Figure 3-5**. It can be observed that the relative diffusion barrier of Li atom adsorbed at the surface layer of MoO_3 surface with GNSs modified (MoO_3/GNSs) is 0.82 eV, which is much smaller than that of pristine MoO_3 (3.73 eV) and MoO_3/GNSs-P (1.02 eV). This is because that the intercalated Li atom interacts with both GNSs and MoO_3 layer, reducing the Li diffusion barrier. However, the Li diffusion barriers of the MoO_3/GNSs, along the diffusion path from subsurface insertion site (B) to bulk adsorption site (C), are only slightly smaller than that on the pristine MoO_3 and MoO_3/GNSs-P, revealing that the equilibrium geometries are ruled by the MoO_3 layer. Based on the relative diffusion barriers of Li atom in different configurations, it could be reasonably concluded that Li atom adsorption at the MoO_3 surface is significantly enhanced due to GNSs modification, but the Li diffusion barriers of the pristine MoO_3, MoO_3/GNSs-P and MoO_3/GNSs, along the diffusion path from subsurface insertion site (B) to bulk adsorption site (C), are ruled by the MoO_3 layer, and almost isn’t affected by the introduction of GNSs. These calculation results are beneficial

for understanding the microscopic origin of the synergistic mechanism of MoO_3 and GNSs as the anode materials with enhanced performances.

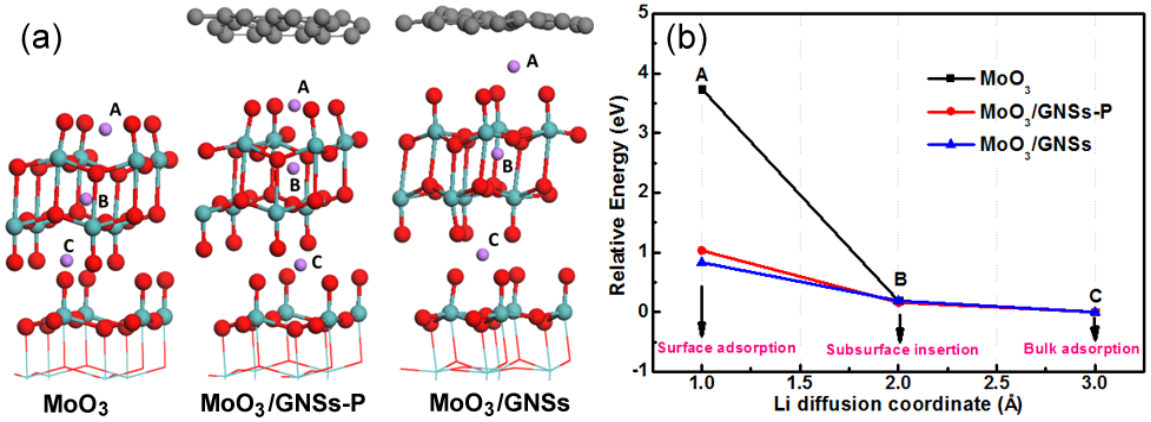

Figure 3-5 (a) The optimized adsorption sites of the Li atom diffusion path in pristine MoO_3, MoO_3/GNSs-P (without defect), MoO_3/GNSs (with defect) composite structure, and (b) the corresponding relative potential energy of Li atom at each site.

In brief, the significantly enhanced electrochemical performances are ascribed to the well-organized interleaved 3D structure and the synergistic effect between GNSs and MoO_3 nanobelts. Firstly, GNSs with high electronic conductivity provides useful pathways for electron mobility and can effectively reduce the diffusion energy barriers of Li atom adsorbed on MoO_3 nanobelt surface. Moreover, GNSs could inhibit the agglomeration of the MoO_3 nanobelts and serve as physical protection layer, thus improving the utilization of MoO_3 nanobelts, maintaining its original structure and achieving a high reversible capacity. Secondly, one-dimensional (1D) MoO_3 nanobelts with height and width in the micrometer and length in the micrometer range combine the advantages of nanomaterials and micromaterials. The nanometer size height and width benefit to fast lithium ion insertion and extraction, while the micrometer size length is good for electron transport between wires.

Thirdly, the as-formed 3D network constructed by GNSs and 1D MoO_3 nanobelts creates interconnected channels which are not only favorable for fast electron transport, but also achieving a large exposed exterior surface to enhance reactivity between electrode and electrolyte. As mentioned above such extraordinary properties of MoO_3/GNSs-2 nanocomposite makes it as a promising anode material.

3.3.2 3D PANI/GNSs derived carbon as cathode material

The surface morphology and microstructure of the as-prepared cathode material is performed by SEM, TEM and XRD. The PANI/GNSs-2 carbon materials are derived from 3D PANI/GO composite (**Figure 3-6a**) as the precursor, using the hydrothermal reaction and the following carbonization and activation process. As shown in **Figure 3-6b**, the PANI/GNSs-2 derived carbon has a macro-porous morphology with the network. HRSEM image (**Figure 3-6c**) further reveals that the PANI nanotube is fully encapsulated by the ultrathin GNSs. It should be mentioned that the PANI nanotube is formed by the adsorption of phenazine-containing nucleation centers on oligomer nano-crystallites. [159] Notably, the structure of the PANI is retained after carbonization and activation process, which is attributed to the cross-linking reaction beneficial for maintaining the structure stability of the supramolecular.[159, 160] From the low resolution TEM image (**Figure 3-6d**), the PANI possess nanotubular structure with the diameter of 90-150 nm and the length of 0.5-2 μm. HRTEM (**Figure 3-6e**) indicates that PANI nanotube with the inner diameter of 20-45 nm are uniformly and completely encapsulated by transparent and wrinkle GNSs. The unique nanotube structure can provide a larger electrode/electrolyte interface area, which effectively increases the electro-active region and shortens ion diffusion length during the

charge/discharge process. SAED pattern (inset in **Figure 3-6e**) reveals the amorphous and disordered structure of the PANI/GNSs-2 derived carbon.

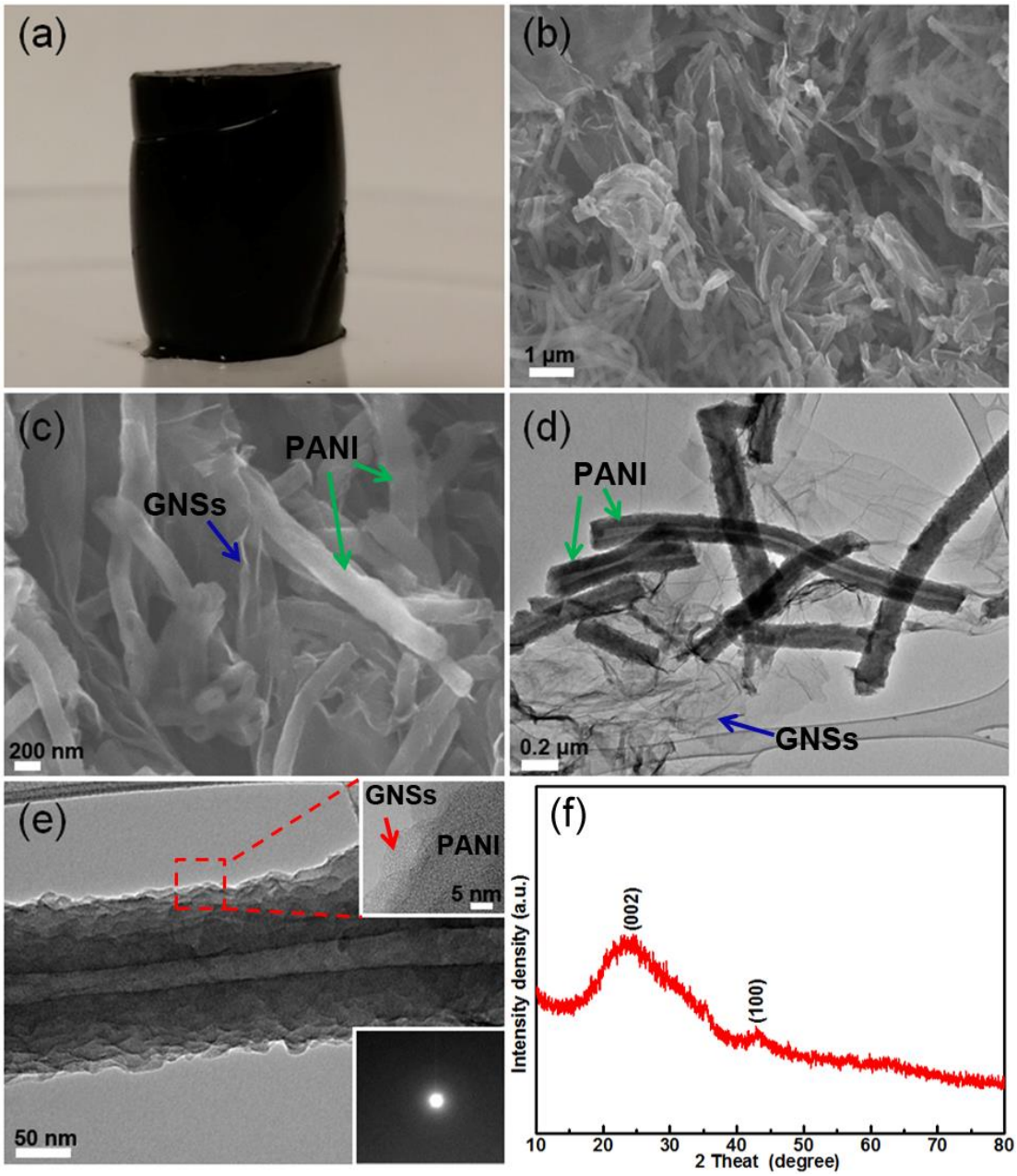

Figure 3-6 (a) Photograph, (b) low-magnification SEM image, (c) high-magnification SEM image, (d) low-resolution TEM image, (e) high-resolution TEM image, and (f) XRD spectrum of PANI/GNSs-2 derived carbon. The inset shows the corresponding HRTEM image (Top) and SAED pattern (Down).

XRD pattern (**Figure 3-6f**) of the PANI/GNSs-2 derived carbon show two representative broaden peaks at 22° and 43°, which are attributed to the (002) and (100) diffractions of amorphous graphitic carbon,[161, 162] respectively, indicating a much disordered and amorphous structure of the hybrid material. Additionally, the as-prepared PANI/GNSs-2 derived carbon possesses the large specific surface area of 2230 $m^2 \cdot g^{-1}$ with the average pore size of 2.70 nm (**Figure 3-S9**), which can provide more sufficient contact area of electrolyte and benefit to the rapid transport of electrolyte ions during the charge/discharge process. Therefore, it is reasonable to induce that the PANI/GNSs-2 derived carbon would be a promising cathode material based on the above-mentioned.

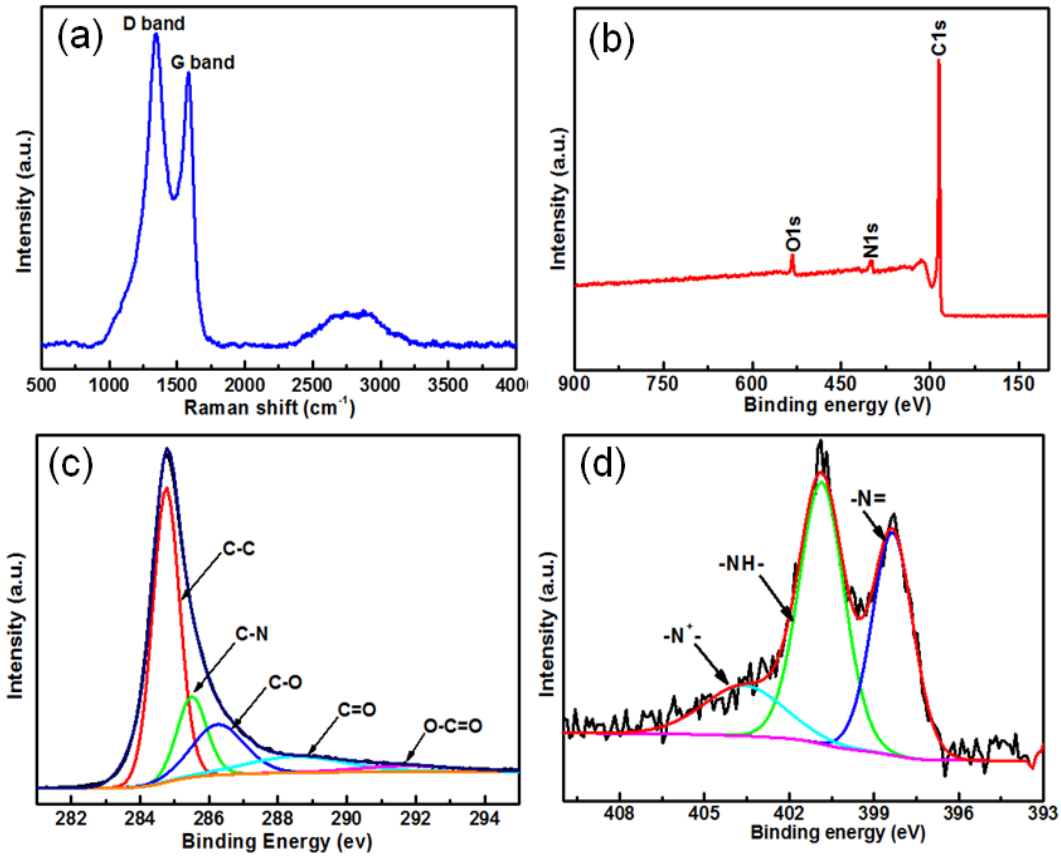

Figure 3-7 (a) Raman spectrum and XPS spectrum of the as-synthesized PANI/GNSs-2 foam derived carbon material: (b) survey, (c) C 1s, and (d) N 1s.

The structure information of the as-prepared sample is further performed by Raman and XPS. **Figure 3-7a** shows the Raman spectrum of PANI/GNSs-2 foam derived carbon. Based on the relative intensities of the D band (1350 cm^{-1}) and G band (1581 cm^{-1}), it indicates the obtained material with the disordered nature, consistence with the corresponding results of TEM and XRD. XPS survey (**Figure 3-7b**) confirms the co-existence of C, N, and O elements in the obtained production. The deconvolution peaks of the C1s spectrum (**Figure 3-7c**) are resolved into five components: C–C group (284.8 eV), C–N group (285.4 eV), C–O group (286.5 eV), C=O group (288.3 eV), and O–C=O group (291.1 eV), respectively. **Figure 3-7d** indicates the existence of three different electronic states of the nitrogen: the benzenoid amine (–NH–) at 399.6 eV, the quinoid amine (–N=) at 398.8 eV, and the nitrogen cationic radical ($N^{+}\cdot$) at 401.2 eV, [162] respectively. Owing to the hydrothermal reduction accompanied by the carbonization and activation process, the GNSs/PANI derived carbon not only possess a unique porous structure, but also have fascinating chemical modification features with N- and O-functionalities on the surface. All these results indicate that the 3D structure as well as the large specific surface area would endow the PANI/GNSs derived carbon with better electrochemical performance.

The electrochemical performance of the 3D PANI/GNSs-2 derived carbon electrode with the optimized ratio of 1:9 (**Figure 3-S10**) are investigated by CV and galvanostatic charge/discharge tests. The testing potential is fixed from 3.0 V to 4.5V. The formation of EDLC at the electrode/electrolyte interface during charge/discharge process is based on the adsorption and desorption of anion (PF_6^{-}) over the surface of the PANI/GNSs-2 derived carbon electrode. CV curves (**Figure 3-8a**) of the PANI/GNSs-2 derived carbon electrode exhibit typical rectangular shape, indicating good capacitor behavior and fast charge

propagation at the electrode surface. Importantly, CV curves keep near rectangular shapes with slightly distorted even at high scan rate, demonstrating the rapid diffusion of PF_6^- into the PANI/GNSs-2 derived carbon. Meanwhile, a linear dependence was observed between the current densities (anodic current density and cathodic current density) and scan rates ranging from 5 to 100 $mV \cdot s^{-1}$ (**Figure 3-8b**), further supporting that charge storage mechanism of the PANI/GNSs-2 derived carbon is the fast surface adsorption/desorption process.

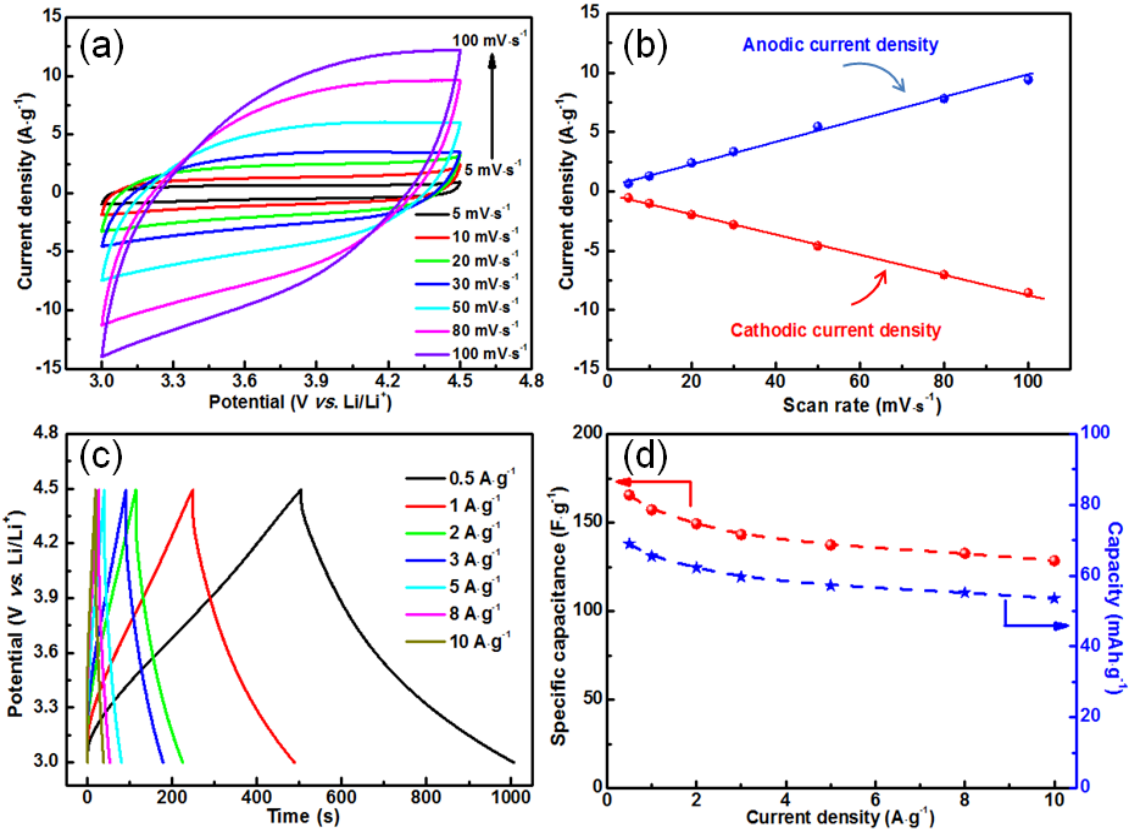

Figure 3-8 (a) CV test of the PANI/GNSs-2 derived carbon electrode at different scan rates, (b) plot of anodic and cathodic current density versus scan rates, (c) galvanostatic charge/discharge curves at different current densities from 0.5 to 10 $A \cdot g^{-1}$, and (d) the relationship between specific capacitance/capacity and current densities.

Figure 3-8c presents the galvanostatic charge/discharge curves of the PANI/GNSs-2 derived carbon electrode under different current densities. A linear relationship between the potential and time is observed, indicating good electric double layer behavior, which agrees well with the results obtained from CV curves. Based on the discharge curves, the specific capacitance of the PANI/GNSs-2 derived carbon electrode at the current density of 0.5, 1, 2, 3, 5, 8, 10 $A \cdot g^{-1}$ are 167.5, 157.1, 148.3, 143.6, 137.7, 132.6, and 126.2 $F \cdot g^{-1}$, respectively. **Figure 3-8d** shows the variation of specific capacitance/capacity with different current densities. The PANI/GNSs-2 derived carbon electrode shows the specific capacitance as high as 167.5 $F \cdot g^{-1}$ at 0.5 $A \cdot g^{-1}$. After conversion, the capacity of the PANI/GNSs-2 derived carbon electrode is 67.8 $mAh \cdot g^{-1}$ at 0.5 $A \cdot g^{-1}$, which is comparable or better than those of AC in reported references (35 $mAh \cdot g^{-1}$ at 0.1 $A \cdot g^{-1}$).[118, 121, 163, 164] Furthermore, it still remain more than 75.3 % capacitance retention at 10 $A \cdot g^{-1}$ compared with that at 0.5 $A \cdot g^{-1}$, indicating its good rate capability. More importantly, there is only 6% capacitance loss of the PANI/GNSs-2 derived carbon after 3000 cycles at 2 $A \cdot g^{-1}$ (**Figure 3-S11**), indicating an excellent cycle stability. These excellent electrochemical performances presented here suggest that the PANI/GNSs-2 derived carbon could be used as a cathode material in high-performance LIHSs due to its unique surface and structure properties. In this unique 3D structure, PANI derived carbon with unique nanotubular structure provides increased electrode/electrolyte interface area, more electro-active site and short ion diffusion path, which enhance the specific capacitance and the rate capability. Furthermore, 3D GNSs structure facilitates rapid transport of the electrons during charge/discharge process by bridging the adjacent individual PANI derived nanotube together.

3.3.3 LIHSs based on 3D MoO_3/GNSs anode and 3D PANI/GNSs cathode

A hybrid supercapacitor is constructed using the 3D MoO_3/GNSs nanocomposite and the 3D PANI/GNSs derived carbon as anode and cathode, respectively. During the charge process, Li^+ ions intercalate into the MoO_3/GNSs composite, while PF_6^- anions adsorb onto the PANI/GNSs derived carbon/electrolyte interface. Subsequent to the discharge process, Li^+ ions are extracted from the lattice of MoO_3/GNSs composite and PF_6^- anions desorbs from the PANI/GNSs derived carbon/electrolyte interface. The mass loading of each electrode is adjusted by the equation $Q^+ = Q^-$ ($m^+ q^+ = m^- q^-$, where Q and q are the capacity and specific capacitance, respectively, and m is the mass loading of active material). Here, the voltage window of the asymmetric supercapacitors is controlled between 0.0 and 3.8 V.

CV curves (**Figure 3-9a**) of the as-prepared LIHSs show a relative quasi-rectangular shape, indicating that the fast Li^+ intercalation reaction of MoO_3/GNSs-2 composite matches the rapid ion adsorption at the 3D PANI/GNSs-2 derived carbon/electrolyte interface. All the charge/discharge curves of the hybrid cell show the symmetric quasi-triangular shape (**Figure 3-9b**), demonstrating the excellent combination of intercalation reaction and non-faradaic capacitive charge storage, which agrees well with the CV results. Based on the discharging curve, the specific capacitance of the hybrid cell is the 61.7 $F \cdot g^{-1}$ at 0.1 $A \cdot g^{-1}$ and is still maintained at approximately 24.5 $F \cdot g^{-1}$ even at 5 $A \cdot g^{-1}$ (**Figure 3-9c**). This excellent capacitive character of the as-obtained LIHSs are attributed to the synergistic effect between the unique structure of 3D PANI/GNSs-2 derived carbon and 3D MoO_3/GNSs-2 composite, which ensures more sufficient contact region between electrode material and electrolyte and facilitates the rapid electron transport, thus improving the

capacitive behavior. Cycle stability is another important parameter to evaluate the real applications of LIHSs. Encouragingly, the as-prepared LIHSs exhibits a stable cycle performance without significant energy fading after 3000 cycles at 1 $A \cdot g^{-1}$ (~90% of the initial capacitance as shown in **Figure 3-9d**). This prolonged cycling behavior suggests that both 3D MoO_3/GNSs-2 composite and 3D PANI/GNSs-2 derived carbon electrodes are compatible for LIHSs applications in standard inorganic electrolytes.

The electrochemical impedance spectroscopy (EIS) is one of principal methods to evaluate the fundamental behavior of energy storage devices. [165] EIS of the LIHSs after the 1st and 3000th cycle is shown in **Figure 3-9e**. The EIS spectra show the similar form with an arc in the high-frequency region and an inclined line in the low-frequency region. In the high-frequency region, the intersection of the curve at real part (which is equal to R_e) indicates the bulk resistance of the device, and the arc (corresponding to double layer capacitance C_{dl} and charge-transfer resistance R_{ct}) indicates the charge-transfer process at the electrode/electrolyte interface.[166] In the low-frequency region, the slope of the 45° portion of the curve means the Warburg resistance (Z_W), which is related to the diffusion of electrolyte ions in the inner of electrode material.[166, 167] C_L is the limit capacitance.[166, 168] After 3000 cycles, the major difference of EIS spectra is the arc in the high-frequency range and the slope of the 45° portion of the curve. Notably, the charge-transfer resistance of the device increases from 22.6 to 27.2 Ω (**Table 3-S1**), which is probably due to the dissolution of some MoO_3 during the charge/discharge cycling. Moreover, the increased Warburg resistance indicates the increased diffusion and migration pathways of electrolyte ions.

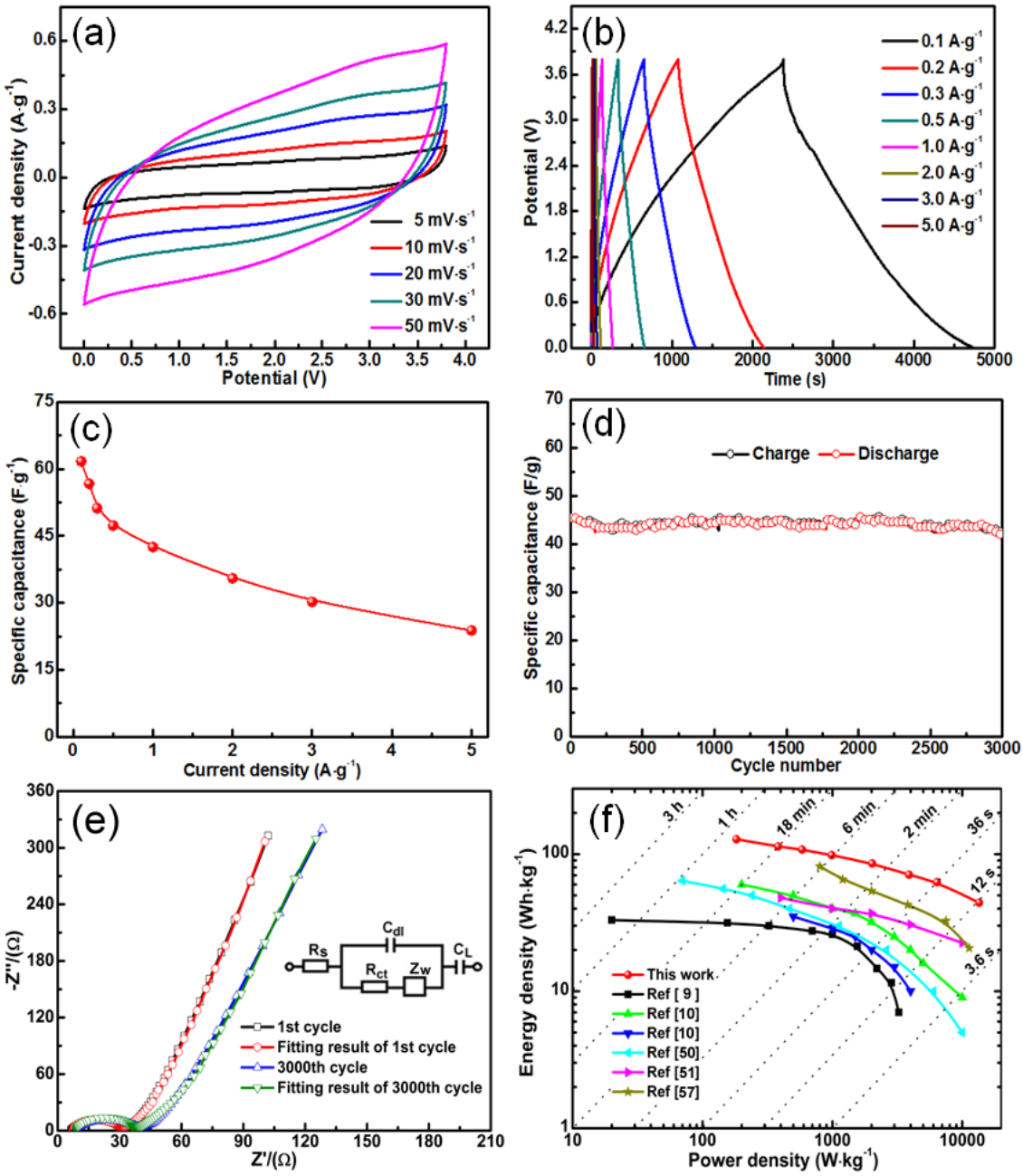

Figure 3-9 (a) CV test of 3D MoO_3/GNSs//3D PANI/GNSs derived carbon LIHSs at various scan rates, (b) galvanostatic charge/discharge under different current densities from 0.1 to 10 $A \cdot g^{-1}$, (c) plot of the specific capacitance versus of current densities, (d) cycle life test at 1 $A \cdot g^{-1}$, (e) Nyquist plot of the as-prepared LIHSs at the frequency ranging from 100 KHz to 0.05 Hz after 1st and 3000th cycle (Inset is the equivalent circuit), (f) the corresponding Ragone plot.

To better prove the excellent performance of the as-prepared LIHSs, the Ragone plot of the hybrid cell is shown in **Figure 3-9f**. The as-prepared LIHSs delivers a high energy density of 128.3 $Wh \cdot kg^{-1}$ at a power density of 182.2 $W \cdot kg^{-1}$. Especially, it still retains an energy density of 44.1 $Wh \cdot kg^{-1}$ at an ultra-high-power density of 13.5 $kW \cdot kg^{-1}$, indicating that the high energy density with good rate capability can be simultaneously obtained. The performance is better than most reported LIHSs devices including CNT/Nb_2O_5//AC,[116] $Li_4Ti_5O_{12}$//AC,[117] $Li_4Ti_5O_{12}$//oligomer derived carbon,[117] *T*-Nb_2O_5@C//MSP-20, [157] *T*-Nb_2O_5/graphene//AC, [158] and TiO_2 nanobelt array//graphene hydrogel.[164] The superior electrochemical performance of the as-prepared LIHSs can be explained by the following aspects. Firstly, the as-prepared 3D MoO_3/GNSs anode material with network structure are not only favorable for fast electron transport, achieving a large exposed exterior surface to enhance reactivity between electrode and electrolyte, but also can effectively reduce the diffusion energy barriers of Li^+ into MoO_3 nanobelt, thus enhancing the Li^+ intercalation/deintercalation process. Secondly, the obtained 3D PANI/GNSs with large specific surface area and appropriate pore size benefits to the transport of the electrolyte ions and provide more active sites, enhancing the energy density and the rate capability.

3.4 Conclusions

In summary, we have constructed a novel high-performance LIHSs by successful integrating the merits of 3D GNSs-wrapped MoO_3 nanobelt foam as anode and 3D GNSs/PANI nanotube foam derived carbon as cathode to both enhance the energy and power densities. The as-prepared 3D MoO_3/GNSs-2 nanocomposite shows enhanced specific capacity (about 1000 $mAh \cdot g^{-1}$ at 100 $mA \cdot g^{-1}$), improved rate performance and long

cyclability. Meanwhile, the well-structured 3D PANI/GNSs-2 derived carbon material fabricated by a facile approach including hydrothermal reaction and a simple carbonization and activation process is used as a cathode electrode material, which exhibits high specific capacitance, good rate capability and long-term cycle stability. Encouraging, by employing these two graphene foam-enhanced materials, the 3D MoO_3/GNSs foam//3D PANI/GNSs foam derived carbon LIHSs possesses a wide operating voltage range from of 0.0 to 3.8 V, a long-term cycle life (with 90% capacity retention after 3000 cycles), and an improved ultrahigh energy density of 128.3 $Wh \cdot kg^{-1}$ (at power density of 182.2 $W \cdot kg^{-1}$), which also remains of 44.1 $Wh \cdot kg^{-1}$ even at high power density of 13.5 $kW \cdot kg^{-1}$. Benefiting from such a subtle design, the LIHSs show superior energy output and better power delivery compared with most reported LIHSs devices. This strategy presented here may open a new door to design and build the novel and high-performance energy storage devices.

3.5 Supporting information

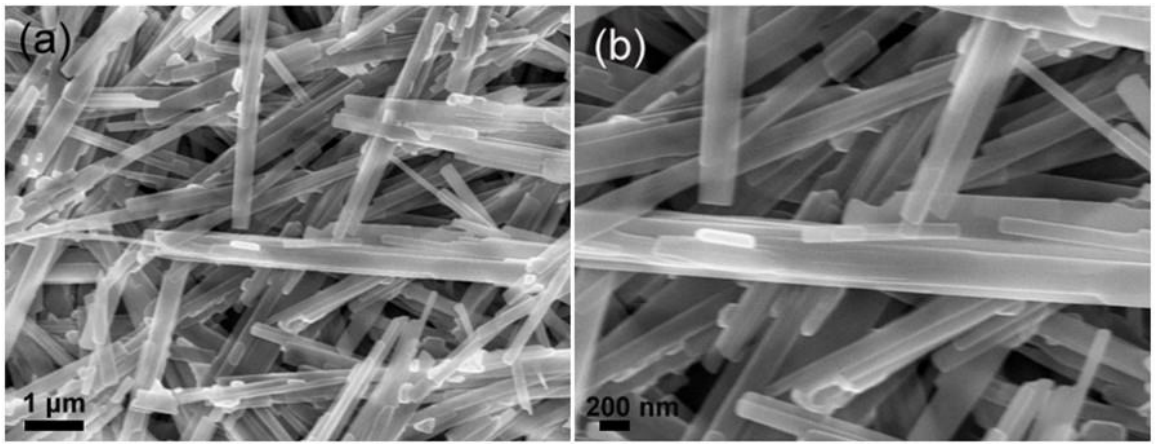

Figure 3-S1 (a) Low-magnification and (b) high-magnification SEM images of MoO_3 nanobelts.

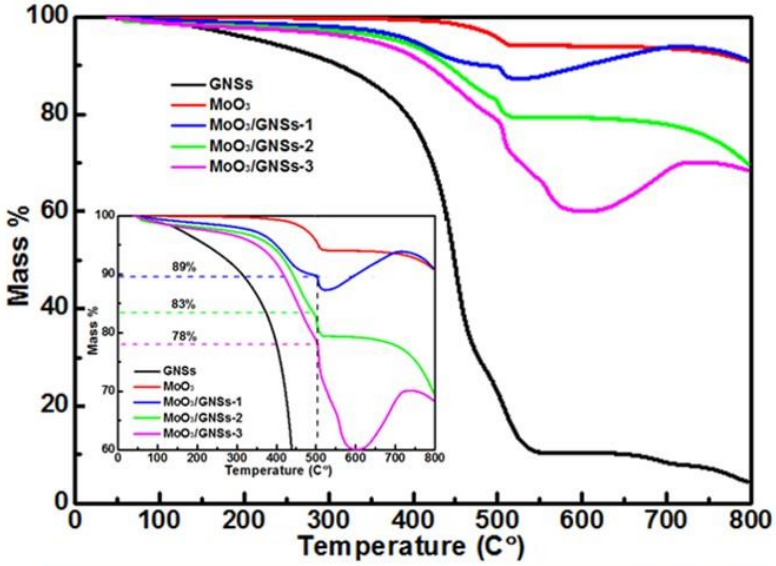

	MoO_3/GNSs-1	MoO_3/GNSs-2	MoO_3/GNSs-3
GNSs (%)	5.86	11.27	17.13
MoO_3 (%)	94.14	88.73	72.87

Figure 3-S2 TG curves of the GNSs, MoO_3, and 3D MoO_3/GNSs nanocomposite with the different content of GNSs.

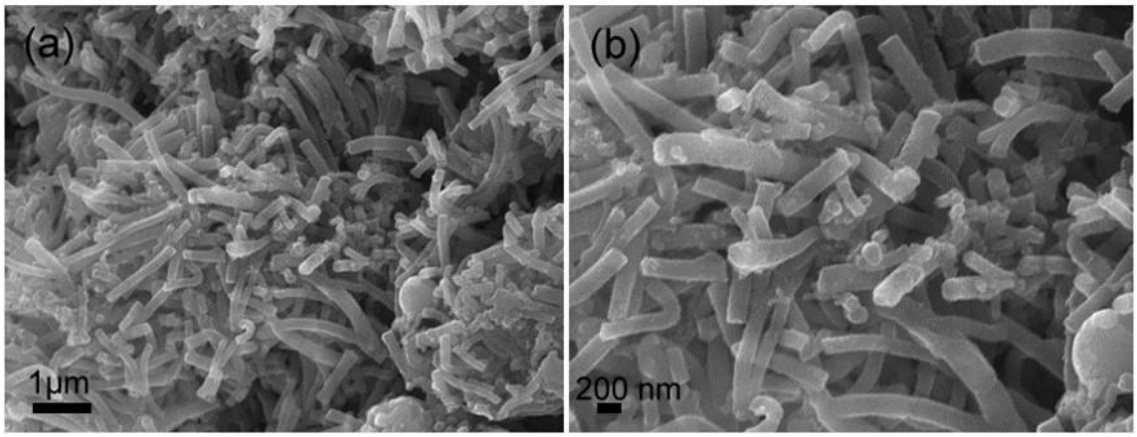

Figure 3-S3 (a) Low-magnification and (b) high-magnification SEM images of PANI nanotubes.

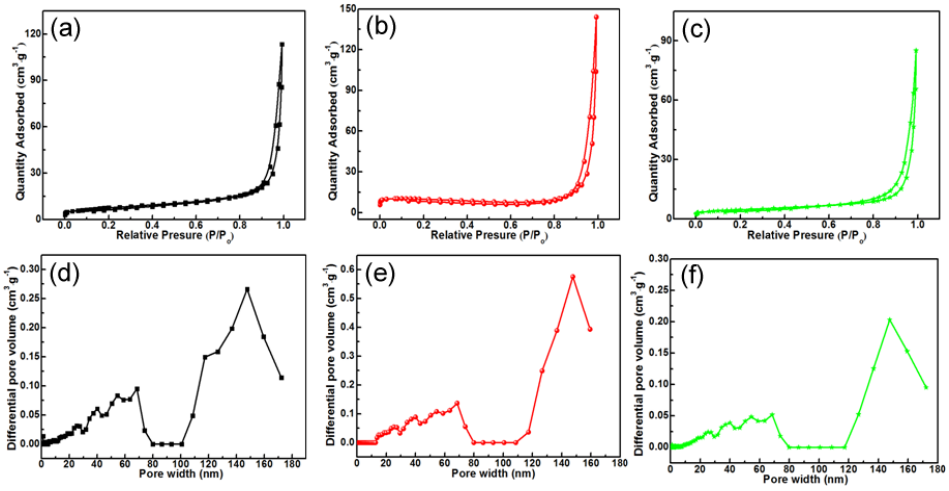

Figure 3-S4 Nitrogen adsorption-desorption isotherms of (a) MoO_3/GNSs-1, (b) MoO_3/GNSs-2, and (c) MoO_3/GNSs-3, respectively; Pore size distribution curves of (d) MoO_3/GNSs-1, (e) MoO_3/GNSs-2, and (f) MoO_3/GNSs-3, respectively.

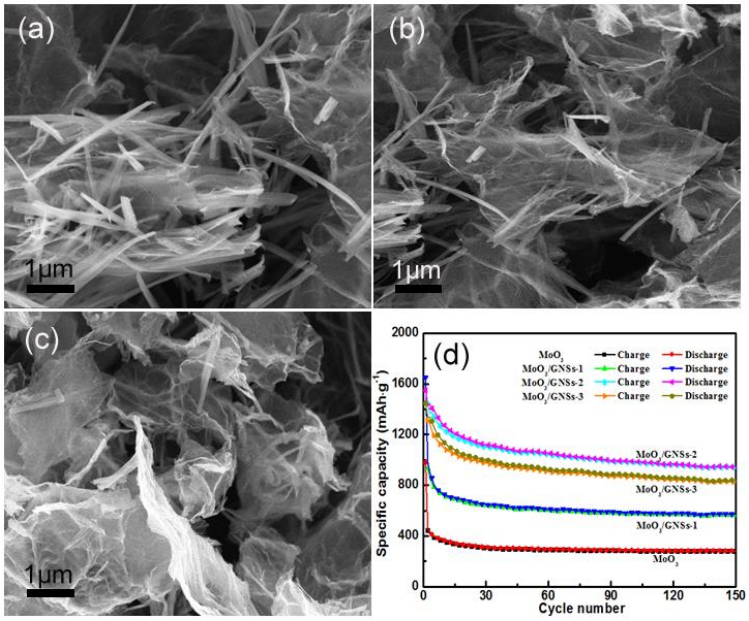

Figure 3-S5 SEM images of MoO_3/GNSs composite with the different content of GNSs: (a) MoO_3/GNSs-1, (b) MoO_3/GNSs-2, (c) MoO_3/GNSs-3, respectively. (d) The corresponding specific capacitance of MoO_3/GNSs composite with the different content of GNSs at 100 $mA \cdot g^{-1}$.

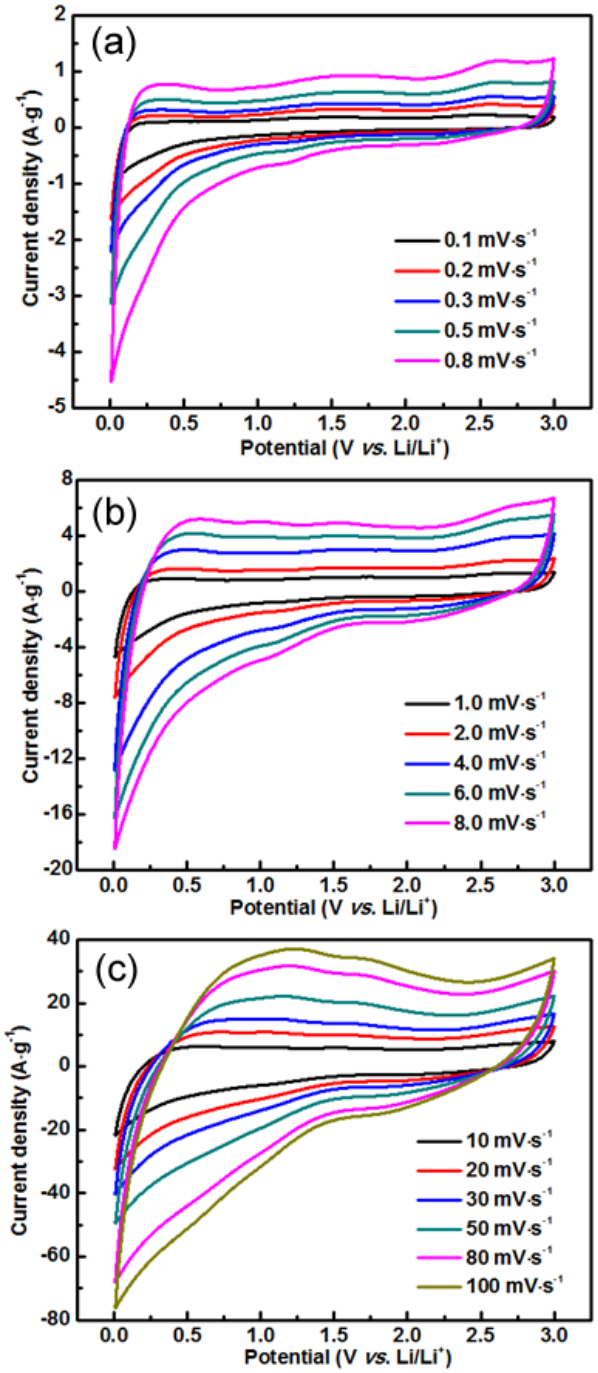

Figure 3-S6 CV curves of MoO_3/GNSs-2 electrode based on half-cell at different scan rates: (a) 0.1 to 0.8 $mV \cdot s^{-1}$, (b) 1.0 to 8.0 $mV \cdot s^{-1}$, (c) 10 to 100 $mV \cdot s^{-1}$, respectively.

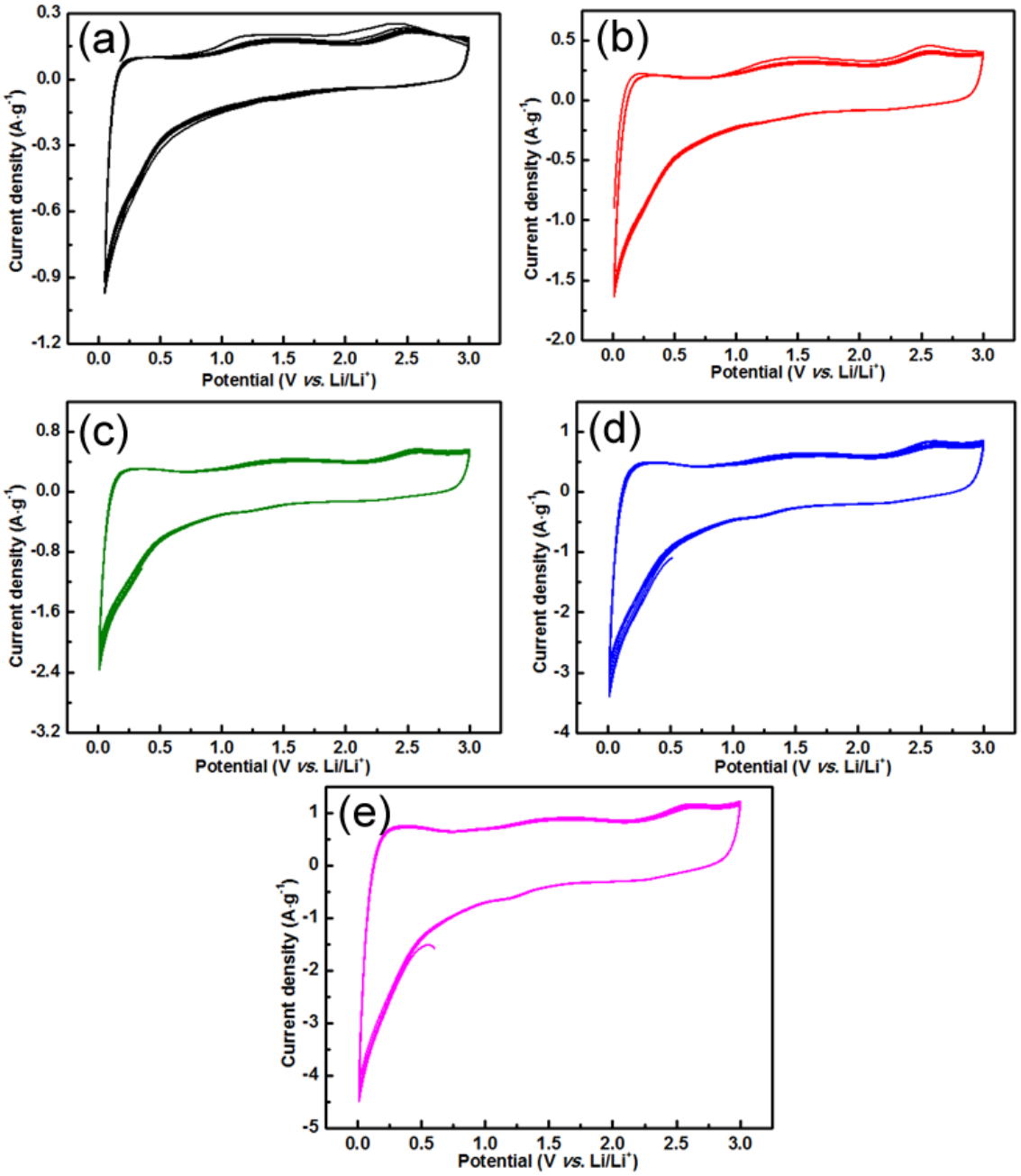

Figure 3-S7 CV curves of MoO_3/GNSs-2 electrode based on half-cell for the first five cycles at the scan rate of: (a) 0.1 $mV \cdot s^{-1}$, (b) 0.2 $mV \cdot s^{-1}$, (c) 0.3 $mV \cdot s^{-1}$, (d) 0.5 $mV \cdot s^{-1}$ and (e) 0.8 $mV \cdot s^{-1}$.

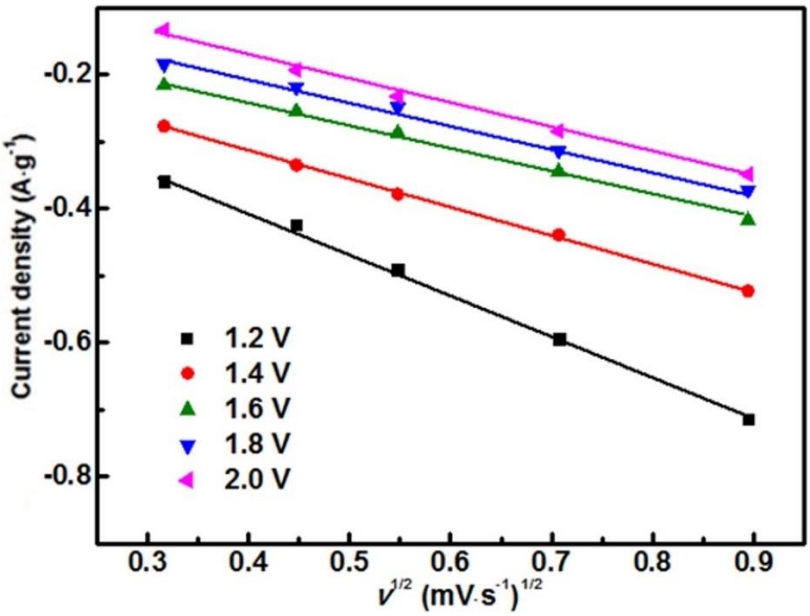

Figure 3-S8 Cathodic peak currents of MoO_3/GNSs-2 composite at various scan rates from 0.1 to 0.8 $mV \cdot s^{-1}$.

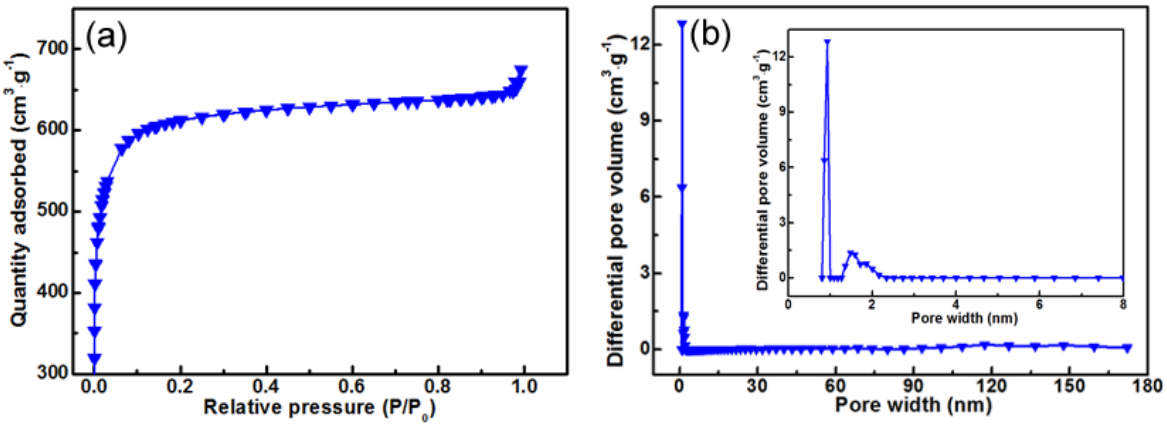

Figure 3-S9 (a) Nitrogen adsorption-desorption isotherms of PANI/GNSs-2 derived carbon and (b) the corresponding pore size distribution.

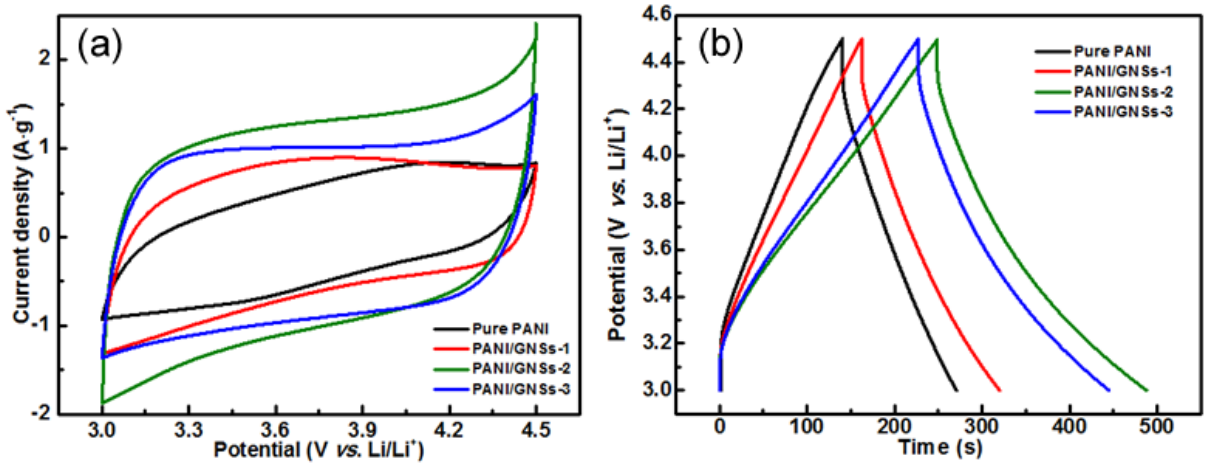

Figure 3-S10 Electrochemical performance of PANI/GNSs-2 derived carbon composite with the different content of GNSs: (a) CV curves at 10 $mV \cdot s^{-1}$, (b) the corresponding charge/discharge curves at 1 $A \cdot g^{-1}$.

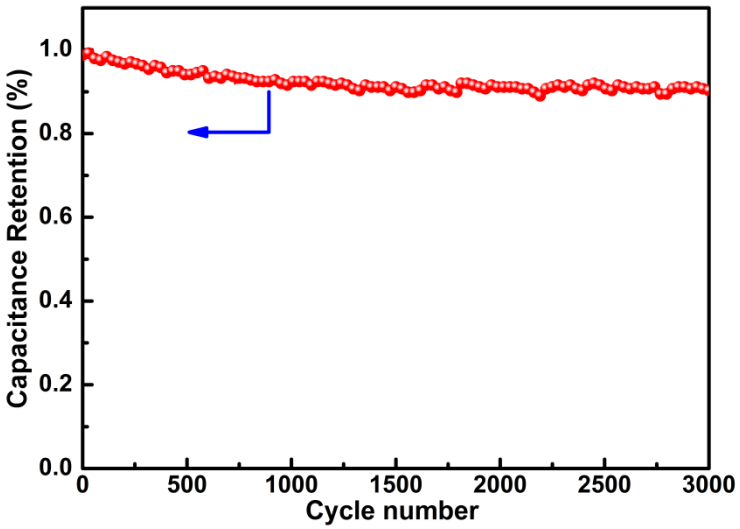

Figure 3-S11 Cycle stability of PANI/GNSs-2 derived carbon after 1st and 3000th cycle at the current density of 2 $A \cdot g^{-1}$.

Table 3-S1 Fitting values of the circuit elements for the experimental impedance spectra based on the proposed equivalent circuit.

	R_s (Ω)	C_{dl} (μF)	R_{ct} (Ω)	σ_w ($\Omega \cdot s^{-1/2}$)	C_L (F)
1st cycle	7.16	8.37	22.59	17.31	0.069
3000th cycle	9.15	7.61	27.19	21.42	0.064

Here, R_s, C_{dl}, R_{ct}, σ_w and C_L are the ohmic resistance of the electrodes and electrolyte, the electric double layer capacitance, the charge transfer resistance at the electrode/electrolyte interface, Warburg impedance coefficient, and the limit capacitance.

Chapter 4: Hair-based flexible knittable supercapacitor with wide operating voltage and ultra-high rate capability

This chapter is reprinted from the manuscript published in *Nano Energy*.

W. Liu, K. Feng, Y. Zhang, T. Yu, L. Han, G. Lui, G. Chiu, P. Fung, A. Yu. "Hair-based flexible knittable supercapacitor with wide operating voltage and ultra-high rate capability". *Nano Energy* **2017**, *34*, 491-499.

4.1 Introduction

Recently, the fast development of wire-shaped portable/wearable electronics has attracted great attention and represented an important trend in modern electronics. [169-172] It has aroused a rising demand for fiber-shaped flexible energy storage devices with good performance, reliability and integration under extensive bending, stretching, and twisting to match these emergent electronic devices.[169-172] Supercapacitors (SCs) have shown great promise as a new type of energy storage devices due to their unique advantages such as excellent rate performance, high power density, and long cycle stability. [171, 172] However, conventional SCs usually could not be well intergated into flexible portable/wearable electronics because of the inflexibilty, large size, heavy weight, and leakage of liquid electrolyte. [173, 174] Fiber-shaped micro-supercapacitors (FMSCs), a new family of SCs, have the attractive features of good flexibilty, small size, and light weight, which make them encouraging candidates for portable/wearable electronics. [175-177]

Electrode materials are the most vital components of FMSCs because they significantly

determine the performance of FMSCs. As reported, fiber-structured electrodes are usually constructed with electrochemically active material and fibrous support. [178] Currently, the state-of-the-art supports are mainly focused on metal wires (such as Ni, Cu, Au and Ti) and carbon-based fibers (such as fibers made from graphene and CNTs). [179-186] Nevertheless, the rigid nature of metal wires makes it difficult to integrate the obtained FMSCs into stretchable and wearable electronics. [179-184] Carbon fibers have been utilized as a substitute, but their low tensile strength, low utilization, and relative complex fabrication process also hinder their wide application in FMSCs. [184-186] Thus, it is highly desired to explore highly flexible, low-cost, and fibrous supports to meet the pressing requirements.

Human hair, a natural fiber with a unique chemical composition, possesses several attractive properties such as high tensile strength, high elastic recovery, and very slow degradation. [187] Furthermore, its squamous surface has a large amount of functional groups which are beneficial for bonding or assembling other components to endow the obtained human hair with some new physicochemical properties. [187] These unique properties make human hair a promising flexible fibrous support and inspire us to adopt it to build flexible FMSCs. However, the restriction is that untreated human hair cannot be directly employed as a current collector due to its poor conductivity. Therefore, it is vital to take full advantage of human hair's attractive properties while developing an effective strategy to address its insulating nature.

Apart from the issues with fibrous supports, the currently reported FMSCs still have unsatisfactory electrochemical performances (such as poor rate capability, narrow potential window, and low energy density). [174, 188] As known, the electrochemical performances of FMSCs are mainly dependent on active materials, the morphology and structure of electrode

materials, and the assemble configuration of FMSCs. [171,174,177,179,182] This useful guideline provides an effective strategy to address these above-mentioned problems of FMSCs by elaborate design and assembly of electrode materials while adopting an asymmetric configuration constructed with appropriate capacitive-type anode and pseudocapacitive-type cathode. In this context, graphene has been selected as active material to build the high-performance flexible FMSCs in this work due to its high theoretic capacitance, outstanding electrical conductivity, high specific surface area, and good flexibility. [189, 190] Furthermore, graphene can be easily combined with other materials and assembled onto various substrates, [191] which further provide the possibility of constructing high-performance flexible asymmetric FMSCs. Meanwhile, MnO_2 has been chosen as cathode material among the pseudocapacitive-type materials due to its high specific capacitance, low cost, and good environment compatibility, but the poor conductivity and low surface area depress its electrochemical performance. [189,190] Hence, it is expected that the organic integration of graphene and MnO_2 with unique structure could improve its performance by the synergistic effect, thus enhancing the electrochemical characteristics of flexible asymmetric FMSCs.

Based on these considerations, we have demonstrated the rational design and assembly of all-solid-state flexible FMSCs that intergate the high flexibility of modified human hair fiber and the excellent electrochemical performance of rGO and three-dimensional (3D) honeycomb-structured MnO_2. Encouragingly, the as-prepared all-solid-state flexible FMSCs show superior electrochemical performance including large operating voltage (1.8 V), excellent rate capability (50000 $mV \cdot s^{-1}$), fast frequency response (τ_0 = 55 ms), high specific capacitance (4.02 $F \cdot cm^{-3}$), high volumetric energy density (1.81 $mWh \cdot cm^{-3}$), and long cycle life.

4.2 Experimental

4.2.1 Preparation of the samples

The fabrication process of the human hair/Ni/rGO electrode is described as follows. First, a bundle of human hair (5 cm in length) was rinsed with distilled de-ionized (DDI) water and ethanol, respectively, followed by drying in air. Second, a thin Ni layer (80 nm) was uniformly coated on human hair fiber by e-beam deposition (denoted human hair/Ni fiber). Third, the obtained human hair/Ni fiber was dipped into 3 $mg \cdot ml^{-1}$ GO suspension for several hours, and then carefully washed with the DDI water. Finally, the obtained fiber was reduced by hydrazine hydrate (denoted human hair/Ni/rGO fiber). Here, GO was synthesized based on the reported literatures. [189, 190]

The human hair/Ni/rGO/MnO_2 electrode was fabricated by dipping human hair/Ni/rGO fiber in solution of 0.1 M $Mn(OAc)_2$ for 3 min, and then quickly transferred into solution of 0.1 M $KMnO_4$ for 3 min. The mass loading of MnO_2 on human hair/Ni/rGO fiber can be easily adjusted by the repeat of the above steps. Finally, the obtained fiber was washed with DDI water and dried in air at 80 °C for 5h (denoted human hair/Ni/rGO/ MnO_2 fiber).

4.2.2 Fabrication of human hair fiber based FMSCs

A mixture of 6 g PVA and 3 g KOH in 100 ml DDI water was stirred at 80 °C for 6h. Afterward, the human hair/Ni/rGO/MnO_2 fiber was dipped into the PVA/KOH gel, and then twisted with the human hair/Ni/rGO fiber electrode. The device was finally solidified at ambient temperature to remove excess water. The PVA/KOH gel acts not only as an ionic electrolyte but also a separator.

4.2.3 Morphological and structural characterization

Scanning electron microscope (SEM, Zeiss Ultra Plus Field SEM) and transmission electron microscope (TEM, FJEOL 2010F) were used to investigate the morphological and the structural characteristics of the obtained samples. X-ray photoelectron spectroscopy (XPS) was measured using a Thermo Scientific K-Alpha spectrometer. Raman spectra was obtained by using a Senterra Raman detection system (Bruker Optics) using a 532 nm laser beam.

4.2.4 Electrochemical characterization

Cyclic voltammetry (CV) tests were done in a wide range of scan rates from 100 to 50000 $mV \cdot s^{-1}$ with a potential window of 1.8 V. Galvanostatic charge/discharge (GCD) tests were measured under various current densities with the same potential window. Electrochemical impedance spectroscopy (EIS) tests were collected with amplitude of 5 mV from 100 kHz to 0.05 Hz at open circuit potential. All electrochemical characterizations of the samples were conducted on a CHI 760E electrochemical workstation.

The capacitance (C_{device}) was obtained from the CV curve by Equation 4-1:

$$C_{device} = \frac{1}{\nu \cdot (V_f - V_i)} \int_{V_i}^{V_f} I(V) dV \quad (4\text{-}1)$$

The volumetric specific capacitance (C_{volume}) was calculated based on Equation 4-2:

$$C_{volume} = \frac{C_{device}}{V} \quad (4\text{-}2)$$

Meanwhile, the volumetric energy density (E) and power density (P) were obtained based on Equation 4-3 and Equation 4-4, respectively:

$$E = \frac{C_{volume} \times \Delta V^2}{2 \times 3600} \quad (4\text{-}3)$$

$$P = \frac{E \times 3600}{t} \quad (4\text{-}4)$$

Where v, $I(V)$, V, ΔV ($\Delta V = V_f - V_i$), t were the scan rate ($mV \cdot s^{-1}$), the discharge current (A), the total volume of two fiber electrodes (cm^3), the potential window (V), and the discharge time (s), respectively.

4.3 Results and discussion

Human hair is a nanostructured biological fiber with a squamous surface (**Figure 4-1a** and **Figure 4-S1**). Also, human hair is rich in disulfide bonds, peptide bonds, and CO– and NH– groups that can form intermolecular interactions (such as hydrogen bonding, π–π accumulation, Vander Waals and electrostatic interactions, **Figure 4-1b**). The structural hierarchy and disulphide cross-linking nature of keratin endow human hair with remarkable mechanical properties, [188] which makes it a promising support for building fiber-shaped flexible electrodes. Graphene oxide (GO) has a highly wrinkled sheet structure (**Figure 4-1c, 1d**) and possesses many oxygen-containing functional groups (**Figure 4-1e** and **Figure 4-S2**), which allows it to easily assemble onto some substrates. [191] Based on the above-mentioned physicochemical properties of human hair and GO, the design and fabrication process of human hair/Ni/rGO/MnO_2 fiber electrode is described as follows (**Figure 4-1f**). First, a thin Ni layer is uniformly coated on human hair by e-beam deposition (**Figure 4-S3**). Second, GO is spontaneously assembled on the human hair/Ni fiber after being immersed in GO solution for several hours. Next, honeycomb structured MnO_2 is grown on human hair/Ni/rGO fiber by chemical bath deposition. Finally, the all-solid-state flexible FMSCs

are obtained by carefully twisting together the human hair/Ni/rGO/MnO_2 fiber electrode wrapped by a layer of gel electrolyte and the human hair/Ni/rGO fiber electrode (**Figure 4-1g** and **Figure 4-S4**).

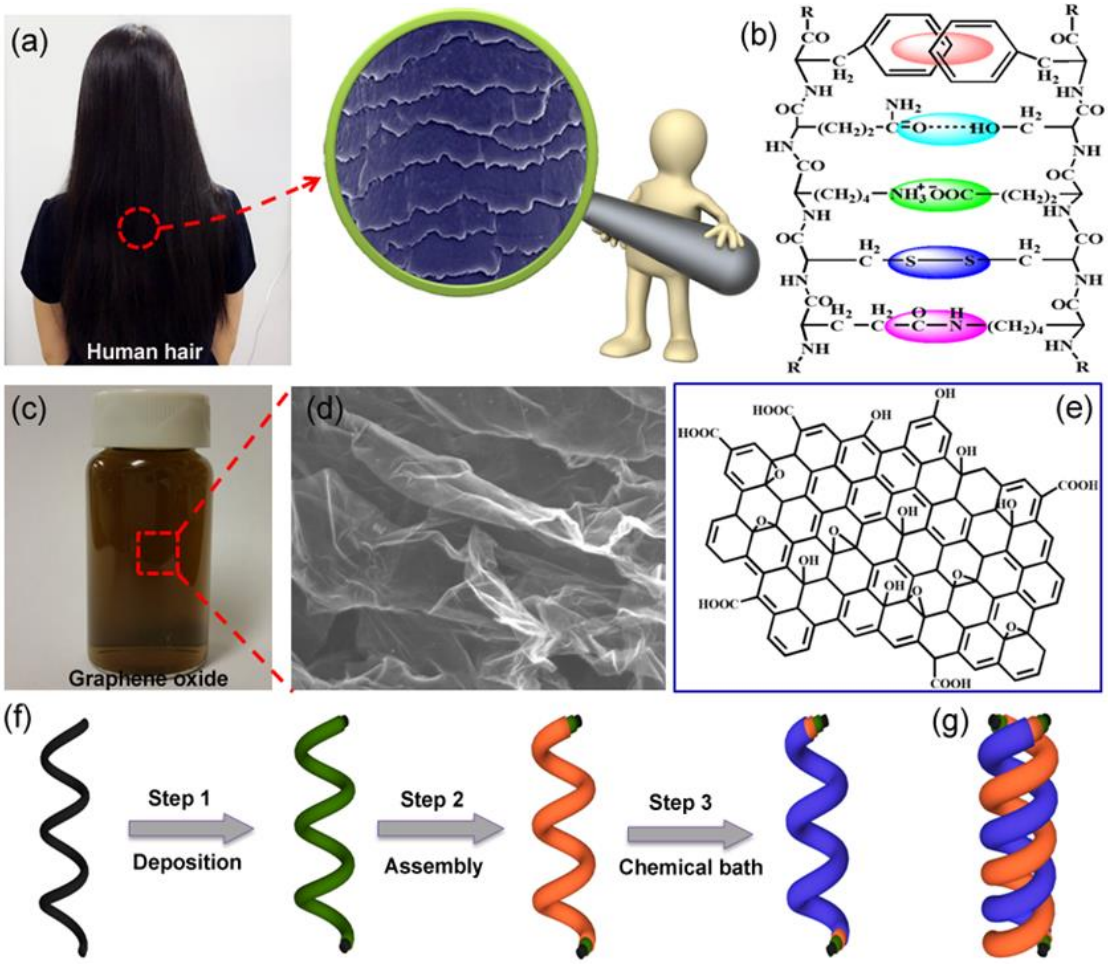

Figure 4-1 (a) Photograph of human hair and (b) Existence of chemical bonds in the hair's cellular structure. (c) Photograph of GO suspension and (d) its corresponding SEM image. (e) Existence of different oxygen functional groups on GO. (f) Schematic of the fabrication process for the human hair/Ni/rGO/MnO_2 fiber electrode. (g) FMSCs constructed by twisting the human hair/Ni/rGO/MnO_2 fiber and human hair/Ni/rGO fiber together.

The morphology and microstructure of typical human hair, human hair/Ni, human hair/Ni/rGO and human hair/Ni/rGO/MnO_2 fibers were characterized by SEM. Human hair has a squamous structure with a diameter from 50 to 100 μm (**Figure 4-2a**). After being uniformly coated with a Ni layer (**Figure 4-2b**), the human hair is highly conductive (0.2 ohm·cm^{-1}) and can be used as a current collector. **Figure 4-2c, 2d** show that the human hair/Ni fiber is tightly wrapped by a layer of rGO, which could provide mechanical stability under deformation and improve rate capability and cycle stability during charge/discharge process. **Figure 4-2e-2g** show the three-dimensional (3D) honeycomb-structured MnO_2 uniformly grown on the human hair/Ni/rGO coaxial fiber (**Figure 4-S5**). The pore sizes of the honeycomb structure range from tens to hundreds of nanometers. Such coaxial human hair/Ni/rGO/MnO_2 fiber with high porosity is beneficial for creating more effective active sites and facilitating the fast access of electrolyte ions into the active material. Moreover, one natural geometrical advantage of the one-dimensional coaxial fiber is to facilitate electron transport over particle electrode materials. [192-194] Elemental mapping (**Figure 4-2h**) shows a uniform distribution of Mn, C and Ni along the whole fiber, giving evidence to the successful preparation of the human hair/Ni/rGO/MnO_2 coaxial fiber. Additionally, the obtained human hair/Ni/rGO/MnO_2 coaxial fiber (**Figure 4-2i**) can be bent, distorted, knotted or stretched without obvious cracking or flaking (**Figure 4-S6**). This result indicates the excellent flexibility of the human hair/Ni/rGO/MnO_2 coaxial fiber and the strong attachment between MnO_2 nanosheets and human hair/Ni/rGO fiber.

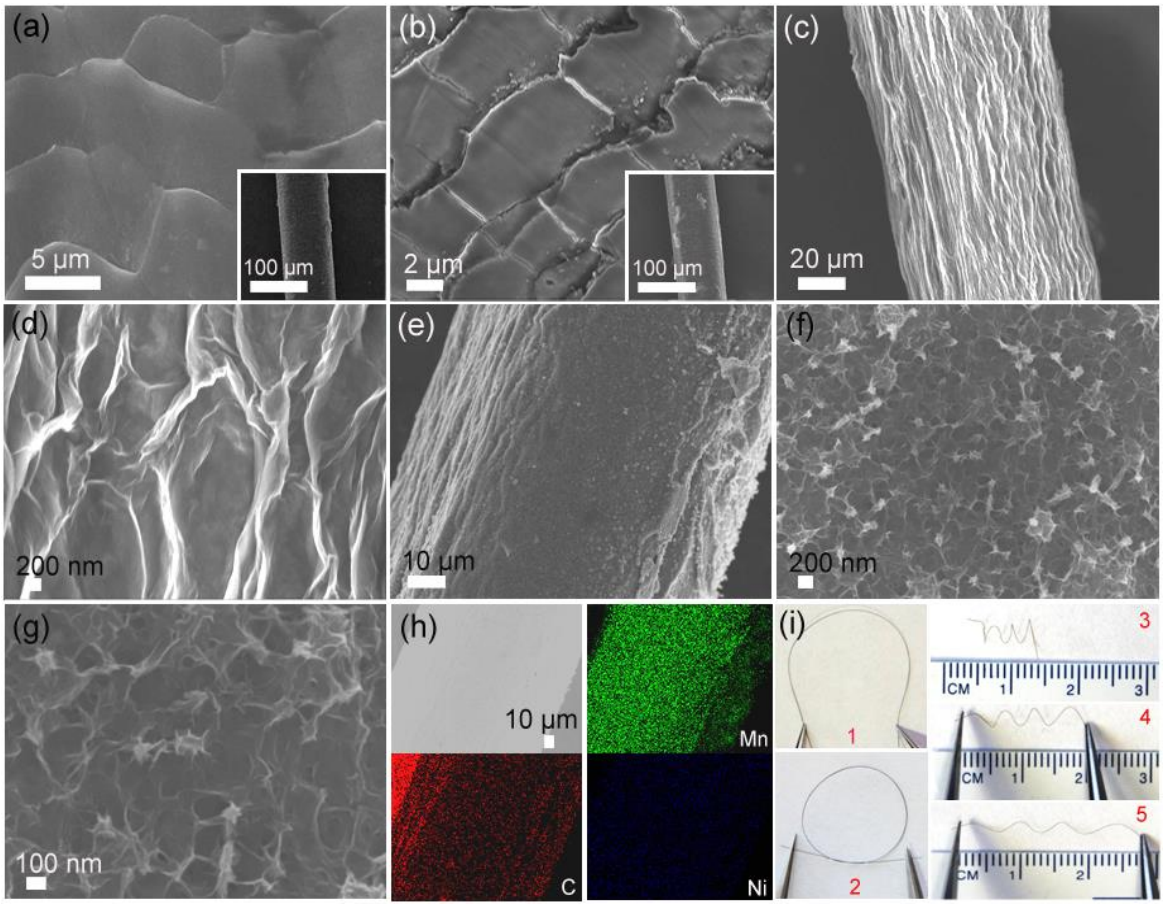

Figure 4-2 Representative SEM images of (a) human hair, (b) human hair/Ni fiber, (c, d) human hair/Ni/rGO fiber, (e-g) human hair/Ni/rGO/MnO_2 fiber. (h) Elemental mapping of Mn, C, Ni elements in a human hair/Ni/rGO/MnO_2 fiber. (i) Photograph of human hair/Ni/rGO/MnO_2 fiber under different mechanical bending, distorting, knotting, and stretching conditions.

TEM images (**Figure 4-3a-c**) demonstrate that the honeycomb-structured MnO_2 scratched down from human hair/Ni/rGO/MnO_2 fiber consists of many ultrathin nanosheets. High-magnification TEM image (**Figure 4-3d**) shows a lattice fringe spacing of 0.25 nm, which is in alignment with the typical (200) crystal plane of birnessite MnO_2.[195, 196] The SAED pattern (**Figure 4-3e**) reveals the polycrystalline nature of the MnO_2 nanosheet.[195, 196] The structure of the human hair/Ni/rGO/MnO_2 fiber is further analyzed using Raman

spectroscopy (**Figure 4-3f**). The D band (1351 cm^{-1}) and G band (1589 cm^{-1}) are associated with rGO, [197, 198] while the major bands at 450–750 cm^{-1} are attributed to the vibrational features of MnO_2. [197, 198]

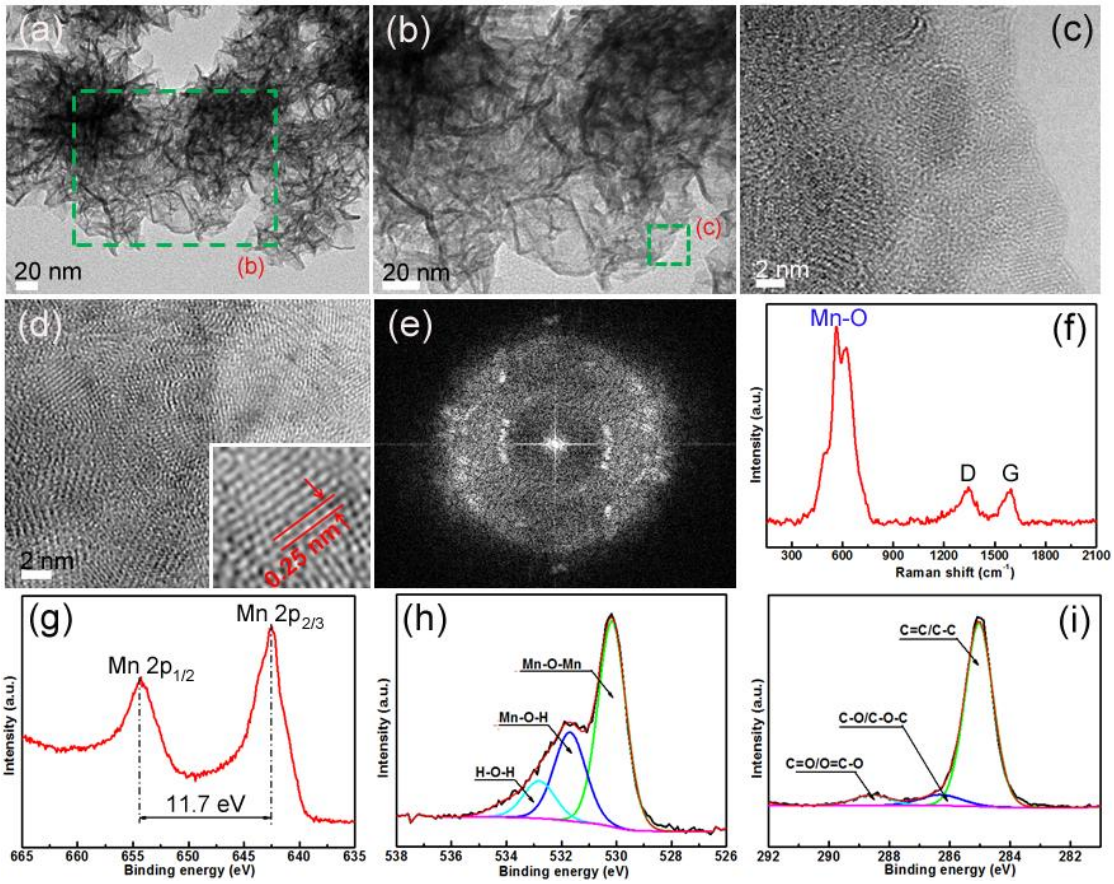

Figure 4-3 (a, b) Low-magnification, (c, d) High-magnification TEM images and (e) Selected-area electron diffraction (SAED) of honeycomb-structured MnO_2 scratched down from human hair/Ni/rGO/MnO_2 fiber, (f) Raman spectra of human hair/Ni/rGO/MnO_2 fiber. XPS spectra of human hair/Ni/rGO/MnO_2 fiber: (g) Mn 2p, (h) C 1s, and (i) O 1s, respectively.

XPS tests were performed to analyze the chemical composition and oxidation state of the sample. The high-resolution spectrum of Mn 2p (**Figure 4-3g**) exhibits two obvious

peaks centered at 642.1 and 653.8 eV, which are attributed to the Mn $2p_{3/2}$ peak and the Mn $2p_{1/2}$ peak, respectively. [196, 199, 200] Moreover, the O 1s spectrum is well fitted into three main peaks centered at 529.7, 530.8, and 531.7 eV (**Figure 4-3h**), which are assigned to various oxygen-containing chemical bonds. [196, 199, 200] These results reveal that the presence of Mn element in the human hair/Ni/rGO/MnO_2 fiber is mainly in the form of Mn(IV). Additionally, the C 1s spectrum is also analyzed and fitted (**Figure 4-3i**): the main peak (284.7 eV) is attributed to graphitic carbon atoms, and the other two weak peaks (286.3 and 288.6 eV) are related to carbon–oxygen bond. [201, 202] It should be noted that these residual oxygen-containing functional groups may enable MnO_2 nanosheets to strongly integrate with rGO.

Evaluation of the electrochemical performance of FMSCs is conducted in a two-electrode system. CV curves of the FMSCs with different operating voltages at 100 $mV \cdot s^{-1}$ are plotted in **Figure 4-4a**. Clearly, the CV curves show rectangular-like shape, and no obvious peak from faradic reaction is observed in each potential region, indicating that the device possesses good capacitive characteristics up to 1.8 V. [203, 204] The operating voltage of the FMSCs is limited to 1.8 V to avoid the appearance of an oxygen evolution tail in the CV curve. Furthermore, with the potential window gradually changing from 0.8 to 1.8 V, the volumetric specific capacitance significantly increases from 2.64 to 4.10 $F \cdot cm^{-3}$. The considerably improved volumetric capacitance is ascribed to the asymmetric configuration presented here, which extend the operating window of the FMSCs due to the reversible nature of the hydrogen electrosorption on the negative electrode. [182, 205, 206] Here, the specific capacitance and other related values presented in this work are calculated based on volume because the mass of the fiber electrode is very low. [203, 204]

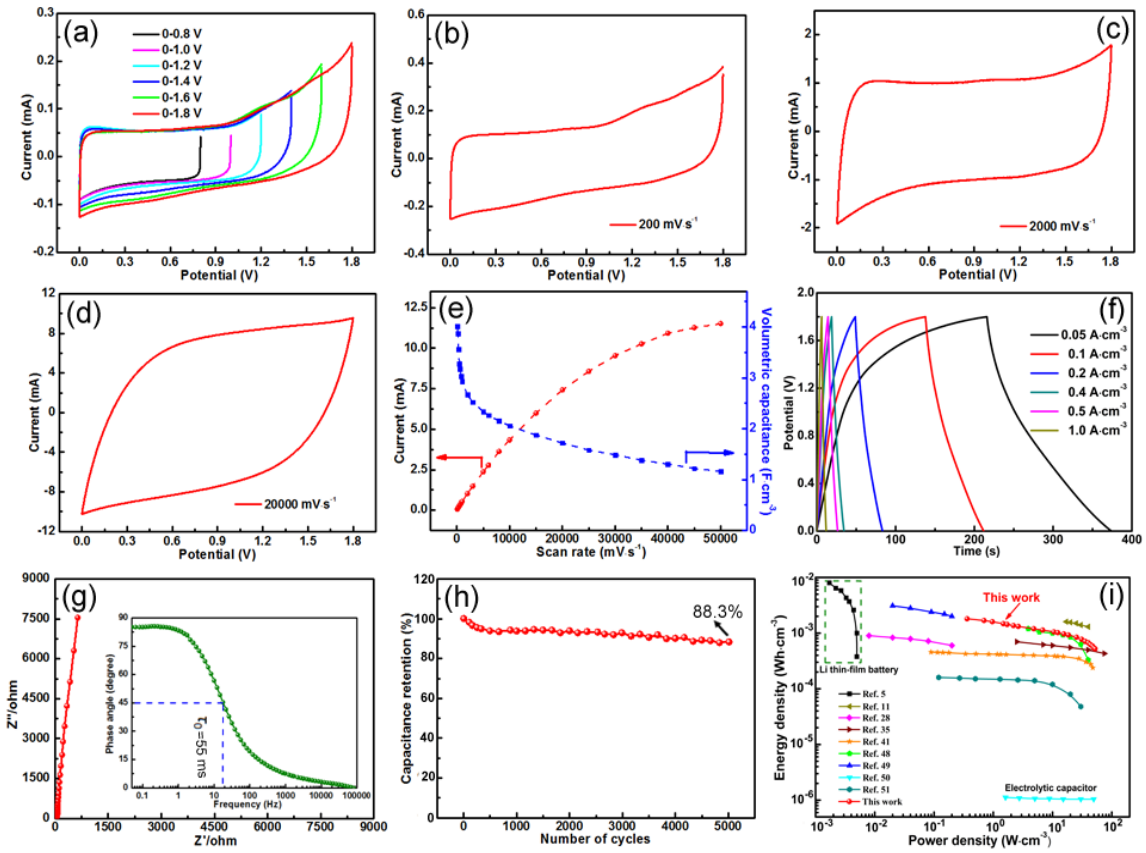

Figure 4-4 Electrochemical performance of the obtained FMSCs device: (a) CV curves recorded under various potential window at 100 $mV \cdot s^{-1}$; CV recorded from of 0 to 1.8 V at: (b) 200 $mV \cdot s^{-1}$, (c) 2000 $mV \cdot s^{-1}$, and (d) 20000 $mV \cdot s^{-1}$, respectively; (e) Discharge currents (left axis) and volumetric capacitances (right axis) versus scan rates; (f) GCD curves at various current densities; (g) Nyquist plot (Inset is the relationship between phase angle and frequency); (h) Capacitance retention plotted versus cycle number; (i) Ragone plot compared with other reported results.

The CV curves of the FMSCs from 100 to 50000 $mV \cdot s^{-1}$ are displayed in Figure 4b-d and **Figure 4-S7**. These CV curves (**Figure 4-4b, 4c**) present a good rectangular-like shape with a rapid current switch upon reversal of voltage, reflecting good double-layer capacitive behavior. [203, 204] Moreover, as shown in **Figure 4-4d**, the FMSCs are still able to maintain a

quasi-rectangular-like shape even at an extremely high 20000 $mV \cdot s^{-1}$ scan rate. This ultra-high-power capability is, to our knowledge, the best performance among the reported FMSCs so far. The ideal capacitive behavior and the excellent rate capability presented here are probably attributed to the synergistic effect of the highly conductive rGO/Ni layer and the honeycomb structure of MnO_2. To further understand the nature of charge storage in the as-prepared FMSCs, the relationship between cathodic currents and scan rates is displayed in **Figure 4-4e**. The cathodic currents show good linear change even up to 10000 $mV \cdot s^{-1}$ indicating a non-diffusion-controlled capacitance process, while it slowly deviates from this linear relationship with further increase of the scan rates, suggesting diffusion-controlled intercalation process at ultra-high scan rates. [207-209]

The dependence of the volumetric specific capacitances of the FMSCs *versus* scan rates is plotted in **Figure 4-4e**. The obtained maximum specific capacitance of the FMSCs is 4.10 $F \cdot cm^{-3}$ at the scan rate of 100 $mV \cdot s^{-1}$, which is comparable or higher than those of other reported FMSCs such as CNT/mesoporous carbon//CNT/mesoporous carbon (0.18 $F \cdot cm^{-3}$), [210] nickel fiber/Co_3O_4 nanowire//carbon fiber/graphene (2.1 $F \cdot cm^{-3}$), [182] MnO_2/carbon fiber//MnO_2/carbon fiber (2.50 $F \cdot cm^{-3}$), [211] MnO_2/graphene/carbon fiber//3D graphene hydrogel/copper wire (2.54 $F \cdot cm^{-3}$), [196] activated carbon fiber tows//activated carbon fiber tows (2.55 $F \cdot cm^{-3}$), [174] MnO_2/carbon nanoparticles/carbon fiber//functionalized carbon nanoparticles/carbon fiber (4.60 $F \cdot cm^{-3}$), [212] and MoS_2-rGO/MWCNT//rGO/MWCNT (5.20 $F \cdot cm^{-3}$). [213] More importantly, the FMSCs still possess a 64% retention rate of its initial capacitance upon increasing the scan rates from 100 to 50000 $mV \cdot s^{-1}$, indicating the excellent rate capability. Furthermore, both the charge and discharge curves show a mathematically proportional relationship with respect to time with no obvious “IR drop”

observed (**Figure 4-4f**), suggesting the good capacitive behavior and the relatively small internal series resistance of the device, [204, 211] respectively. Here, it should be mentioned that the discharge time of the device is not complete proportionate to the discharge current density, which is mainly attributed to insufficient active material involved in the electrochemical reaction, especially high current density. [204, 205] Meanwhile, with the increase of current density from 50 to 1000 $mA \cdot cm^{-3}$ (**Figure 4-S8**), the volumetric capacitances obtained from charge/discharge curves also show a high capacitance retention rate (71% of its volumetric capacitance at 50 $mA \cdot cm^{-3}$), further revealing the characteristic of good rate performance. The high volumetric specific capacitance and the outstanding rate performance of the as-prepared FMSCs could be attributed to the unique structure of the human hair/Ni/rGO/MnO_2 fiber electrode. In this designed hybrid nanostructure, the unique 3D honeycomb structured MnO_2 could increase the contact area between MnO_2 nanosheets and electrolyte and the number of effective active sites. Especially, the ultra-thin nanosheets could shorten the ion diffusion pathways, allowing for fast ion mass transfer during charge/discharge process. Both contribute to the increase of specific capacitance and improve the rate performance of the device. Furthermore, the direct deposition of a thin Ni layer and the assembly of highly conductive rGO on human hair not only obviously improve the electrical conductivity of the hybrid fibrous electrode, but also act as an excellent current collector, which are beneficial for achieving an ultrahigh rate performance.

Additionally, EIS is measured to further reveal the outstanding electrochemical performance of the FMSCs (**Figure 4-4g** and **Figure 4-S9**). The first intersection point of the Nyquist plot with the x-axis possesses a value of 15 Ω which indicates a relatively small equivalent series resistance of the device. In the medium-high frequency region, the absence

of a semicircle suggests efficient ion diffusion and good electrical conductivity. [204, 214] In the low frequency region, the verticality of the sloped line shows characteristic feature of pure capacitive behavior, and the small real resistance value obtained from the line projection onto the x-axis indicates fast electrolyte ion transport behavior in this device. [204, 209] For more information, the relationship between the phase angle and the frequency is shown in the inset of **Figure 4-4g**. The phase angle of the device is close to 90° in the low frequency region, which demonstrates a near-ideal capacitor behavior of this device. [203, 204, 209] Moreover, the relaxation time constant τ_0 ($\tau_0 = 1/f_0$, where f_0 is the characteristic frequency at the phase angle of 45°) is 55 ms, revealing the fast frequency response of the as-prepared FMSCs. [203, 204] Encouragingly, the relaxation time constant presented here is much smaller than that of conventional SCs, [179] comparable with previously reported values of other FMSCs such as polypyrrole (PPy)/MnO_2 nanoflakes/carbon fiber//polypyrrole (PPy)/MnO_2 nanoflakes/carbon fiber (16 ms), [215] MnO_2/carbon fiber//MnO_2/carbon fiber (22 ms), [211] $NiCo_2O_4$/nickel wire//$NiCo_2O_4$/nickel wire (55 ms). [179]

Cycle life is another important aspect to evaluate the performance of FMSCs. It can be observed that our FMSCs still keep 88.3% of their initial capacitance after 5000 cycles (**Figure 4-4h** and **Figure 4-S10**), indicating good cycle stability of the as-prepared FMSCs. Furthermore, Ragone plot is plotted to compare the power and energy densities of the as-prepared FMSCs with other reported results (**Figure 4-4i**). The FMSCs achieve the maximum volumetric energy density of 1.81 $mWh \cdot cm^{-3}$, which is comparable or higher than other published FMSCs such as the $NiCo_2O_4$/nickel wire//$NiCo_2O_4$/nickel wire,[179] MnO_2/graphene/carbon fiber//3D graphene hydrogel/copper wire, [196] PEDOT/MWNT yarn//Pt wire, [216] RGO+CNT@CMC fiber//RGO+CNT@CMC fiber. [217] In addition, the

energy density is also very promising compared with that of commercial electrolytic capacitor and some planar architecture micro-supercapacitors based on rGO and CNT composites, [203, 218] rGO/MnO_2/Ag. [209]

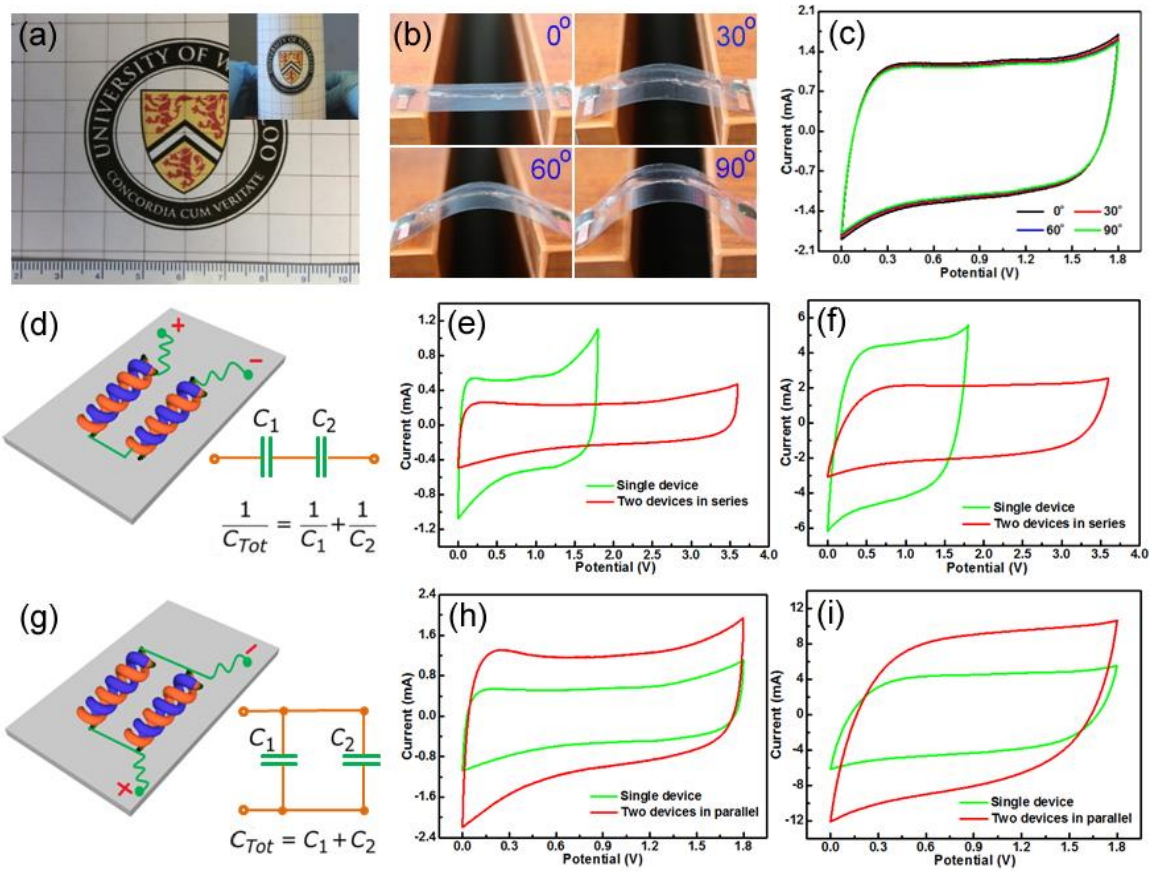

Figure 4-5 (a) Photograph of a network fabric woven from the human hair/Ni/rGO/MnO_2 fiber with dimensions of 6 cm × 8 cm (Inset: bending of the assembled network fabric). (b) Photograph of the as-prepared FMSCs under different bending angles. (c) CV curves of the FMSCs under different bending angles at 5000 $mV \cdot s^{-1}$ (d) Schematic of two FMSCs connected in series and its corresponding CV curves at various scan rates: (e) 1000 $mV \cdot s^{-1}$, (f) 10000 $mV \cdot s^{-1}$. (g) Schematic of two FMSCs connected in parallel and its corresponding CV curves at various scan rates: (h) 1000 $mV \cdot s^{-1}$, (i) 10000 $mV \cdot s^{-1}$.

Another attractive feature of the FMSCs is the knittability and excellent mechanical flexibility. **Figure 4-5a** reveals that the human hair/Ni/rGO/MnO_2 fiber can be woven into a simple textile-shaped framework, and shows good flexibility even bended to 90˚, which demonstrates its promising potential in wearable devices as power source. Importantly, there is little change in the CV curves under different bending states (**Figure 4-5b, 5c**), indicating the good bendability and flexibility of the as-prepared FMSCs device. This is mainly attributed to the excellent mechanical properties of human hair with high tensile strength and good elastic recovery, which provides mechanical stability under deformation and helps maintain cycle stability during charge/discharge process. In addition, it should be mentioned that the good encapsulation of fiber electrode by the PVA/KOH gel electrolyte could prevent the damage of the electrode to some extent, which is also beneficial for improving the bendability and flexibility of the device. Although a single FMSCs device can achieve a large potential window (1.8 V), it still cannot meet some requirements of practical applications. Thus, it is important that connected FMSCs stacks (series or parallel) behave predictably and can achieve their designed output voltage or current, matching that of their host device. **Figure 4-5d** is the schematic diagram of two FMSCs connected in series (**Figure 4-S11a**). Compared with a single FMSCs, the output voltage of two FMSCs in series (3.6 V) is doubled (**Figure 4-5e, 5f**). Figure 5g shows the schematic diagram of two FMSCs devices connected in parallel (**Figure 4-S11b**). As expected, the output current of the two parallel FMSCs is almost twice that of a single device (**Figure 4-5h, 5i**). These results prove that the as-prepared FMSCs follow ideal capacitor voltage/current additions rules for series/parallel connections.

4.4 Conclusions

In summary, high performance all-solid-state flexible FMSCs have been successfully designed and constructed by employing human hair/Ni/rGO/MnO_2 coaxial fiber as cathode and human hair/Ni/rGO coaxial fiber as anode. The resultant FMSCs not only possess the high mechanical flexibility, but also show excellent rate capability, fast frequency responsibility, high energy and power densities, good cyclic stability. This outstanding performance can be explained by the following reasons: 1) human hair/Ni/rGO not only retains the excellent mechanical flexibility of human hair, but also possesses the excellent electrical conductivity served as current collector and backbone for the deposition of nanostructured MnO_2; 2) the honeycomb MnO_2 architecture shortens the diffusion path for electrolyte ions during fast charge/discharge process, making the MnO_2 fully utilized, which can significantly enhance the energy density of the device. In addition, the FMSCs s built based on PVA/KOH gel electrolyte are highly flexible, can be assembled into a stretchable, spring-shaped device, and knitted into fabric for use in portable/wearable electronics. These encouraging results presented here make the FMSCs a promising power source for flexible wearable/stretchable devices and provide a strategic and important reference for the design and construction of high-performance flexible FMSCs.

4.5 Supporting information

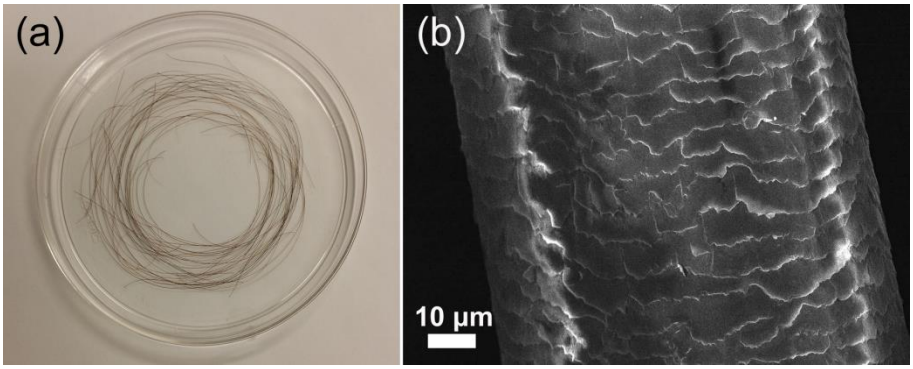

Figure 4-S1 (a) photography of human hair and (b) low-magnification SEM image of human hair fiber.

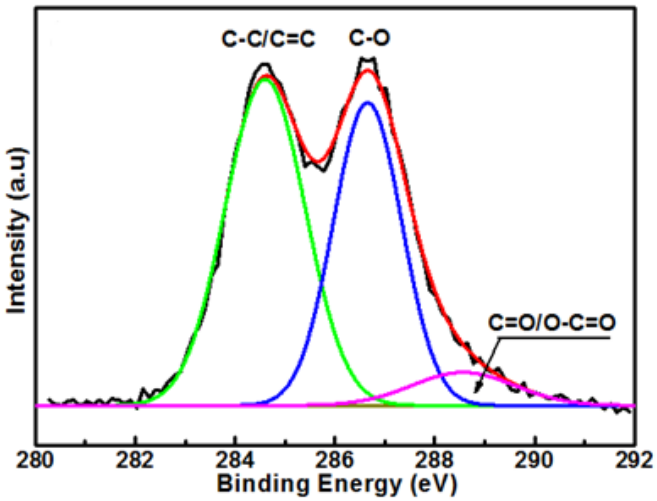

Figure 4-S2 C1s XPS spectra of graphene oxide (GO).

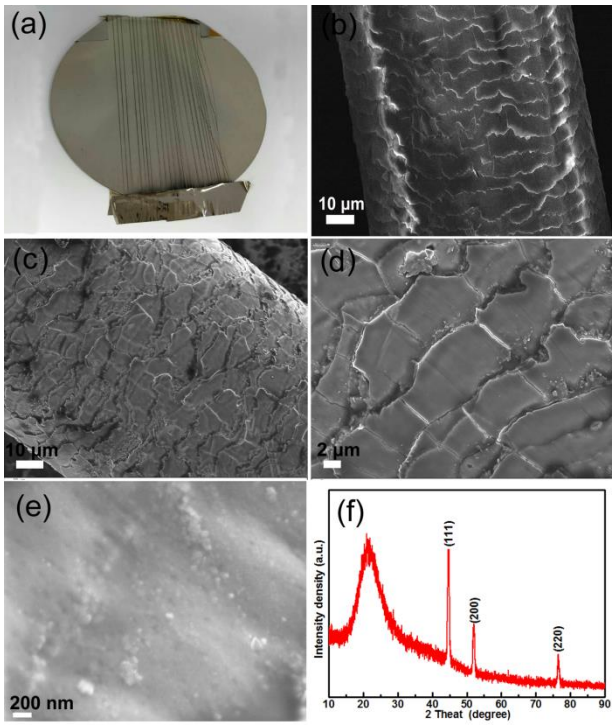

Figure 4-S3 (a) Photography of human hair after the e-beam deposition, (b) SEM image of pure human hair fiber, (c-e) low- and high-resolution SEM images of human hair/Ni fiber, (f) XRD spectrum of human hair/Ni fiber.

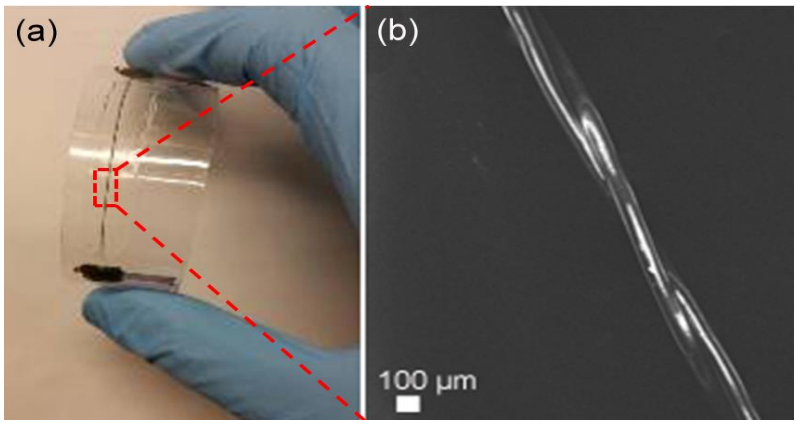

Figure 4-S4 (a) photography of the as-prepared FMSCs device and (b) its corresponding SEM image.

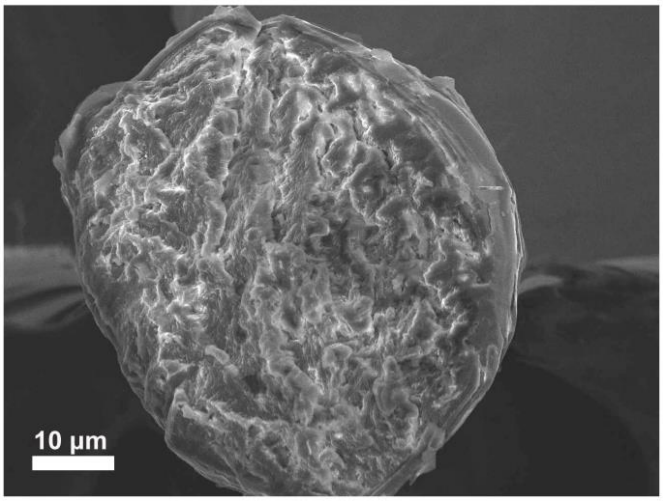

Figure 4-S5 Cross-sectional SEM image of the human hair/Ni/rGO/MnO_2 coaxial fiber.

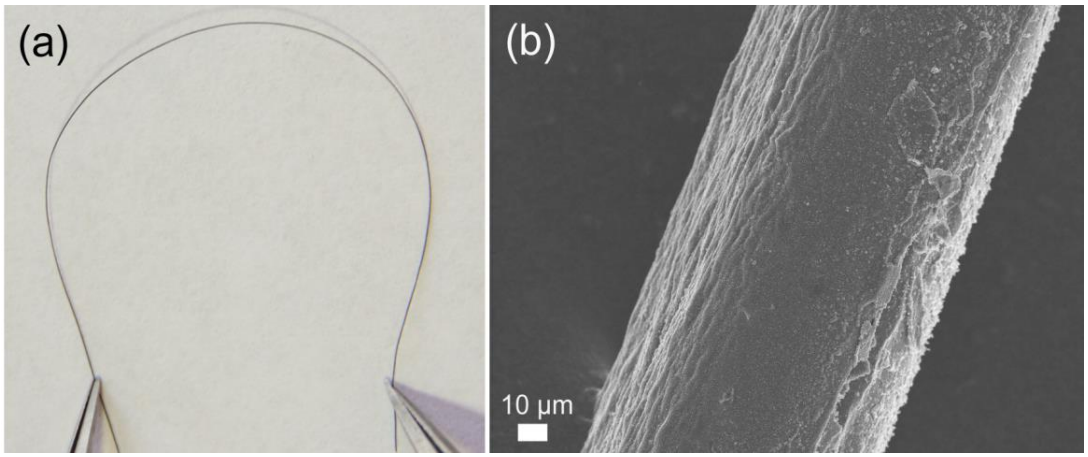

Figure 4-S6 (a) photography of the human hair/Ni/rGO/MnO_2 coaxial fiber under bending state and (b) its corresponding SEM image after the recovery.

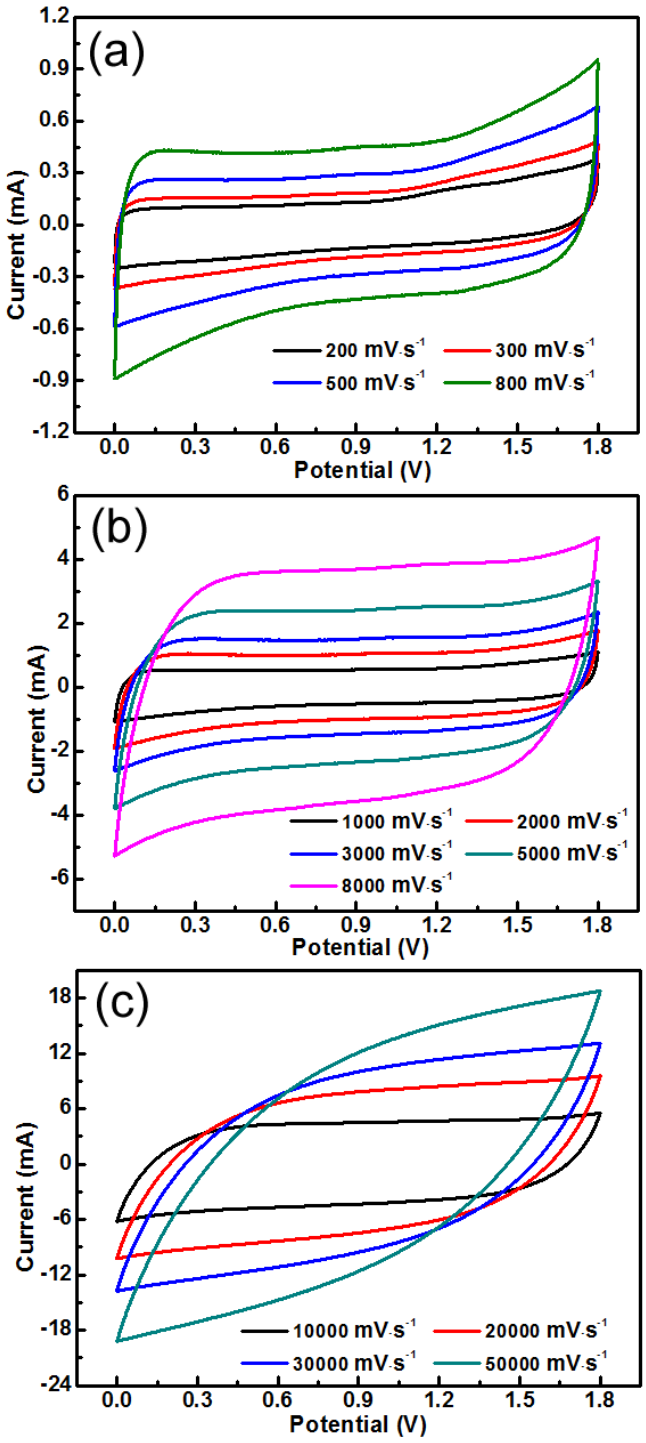

Figure 4-S7 CV curves of the as-prepared FMSCs device at various scan rates: (a) from 200 to 800 $mV \cdot s^{-1}$, (b) from 1000 to 8000 $mV \cdot s^{-1}$, (c) from 10000 to 50000 $mV \cdot s^{-1}$, respectively.

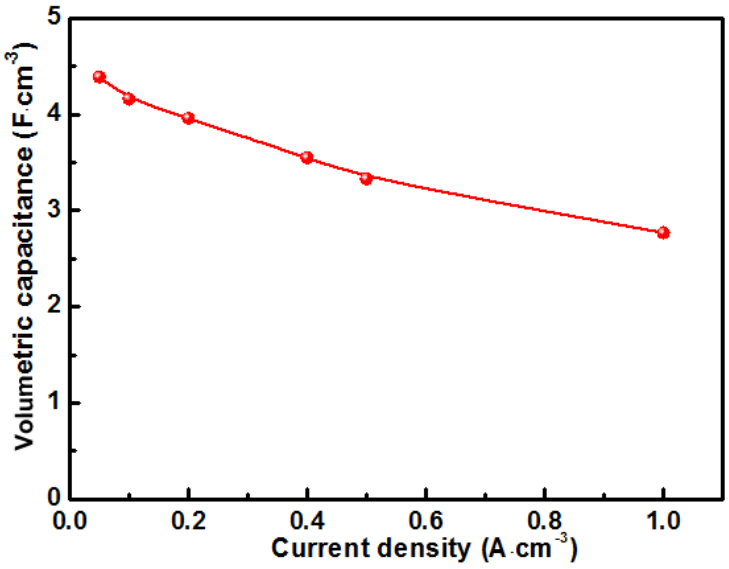

Figure 4-S8 Volumetric capacitance of the as-prepared FMSCs at various current densities from 0.05 to 1.0 A·cm^{-3}.

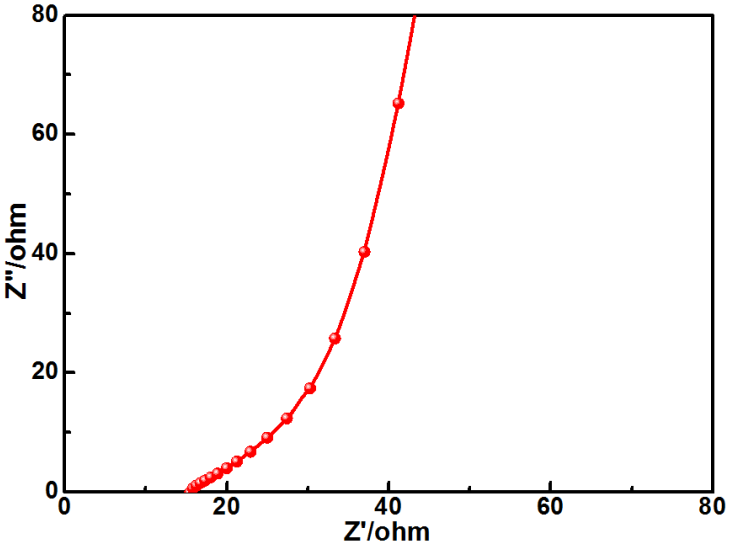

Figure 4-S9 The magnified EIS in the high frequency region of the as-prepared device.

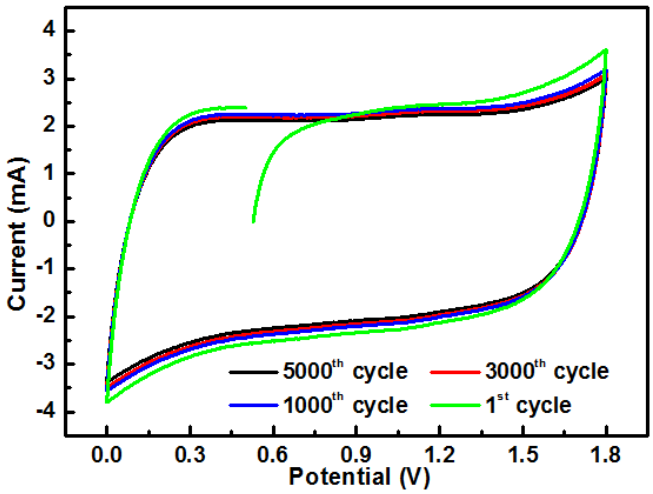

Figure 4-S10 CV curves of the as-prepared FMSCs device under different cycle number.

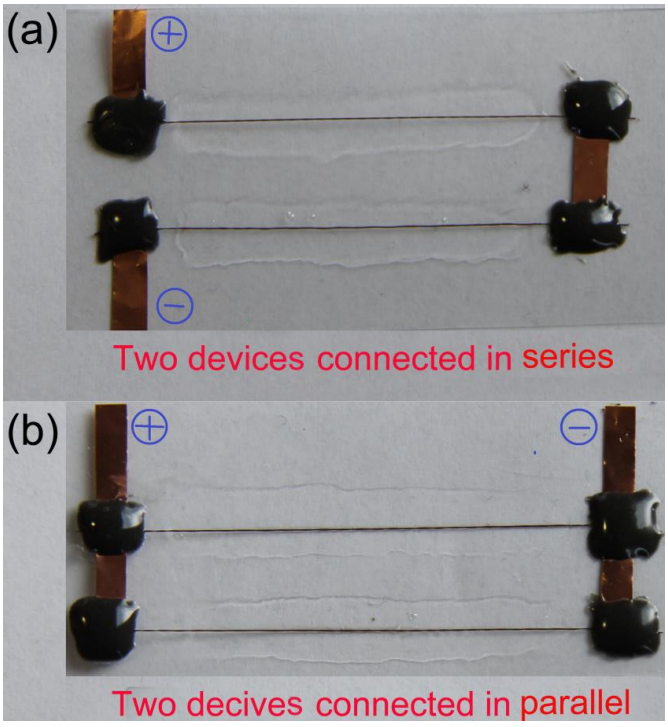

Figure 4-S11 Photography of the as-prepared two FMSCs devices connected in (a) series and (b) parallel, respectively.

Chapter 5: Advanced electrode materials comprising of structure engineered quantum dots for high-performance asymmetric micro-supercapacitors

This chapter is based on the following two works both of which have been published in *Advanced Energy Materials*.

W. Liu, M. Zhang, M. Li, B. Li, W. Zhang, G. Li, M. Xiao, J. Zhu, A. Yu, Z. Chen. "Advanced electrode materials comprising of structure engineered quantum dots for high-performance asymmetric micro-supercapacitors". *Adv. Energy Mater.,* **2020,** *10*, 1903724.

W. Liu, M. Li, G. Jiang, G. Li, J. Zhu, M. Xiao, Y. Zhu, R. Gao, A. Yu, M. Feng, Z. Chen. "Graphene quantum dots-based advanced electrode materials: design, synthesis and their applications in electrochemical energy storage and electrocatalysis". *Adv. Energy Mater.,* **2020**, *10*, 2001275.

5.1 Introduction

With the advent of self-powered nanodevices, implantable medical and portable/wearable electronic devices, innovative research towards new energy storage and conversion devices that are small in size, light-weight, flexible, and other matching features has become increasingly important.[219-225] Among them, in-plane micro-supercapacitors (MSCs) are considered as a promising power source for these emerging modern microelectronic devices because of their impressive advantages such as small dimensions, diversified shapes, good compatibility, superior rate capability, high power density, and long lifespan.[226, 227]

Despite recent progress, the performances of the majority of previously reported MSCs are still insufficient to satisfy the increased demand of the new consumer electronics. It is clear that substantial improvement can be made towards its narrow operating voltages (no more than 1.2 V in aqueous electrolyte), relatively low energy density, slow frequency response capability, and so on. [228, 229] Therefore, much effort has been devoted to improving the electrochemical performance of MSCs by innovating upon their design from various aspects.[230-236] In particular, the development of advanced electrode materials with excellent electrochemical performance by surface and structural engineering is the most reliable and straightforward strategy because the entire performance of cell is highly dependent on the electrode materials. Among these surface and structural engineering strategies, the size-minimization strategy is an effective approach in improving the electrochemical performance of electrode materials because the ion transport time (τ) is proportional to the square of the diffusion length L ($\tau \approx L^2/D$).[237, 238] Considering this, the miniaturized electrode materials with small length scales down to several nanometers (such as quantum dots) can significantly reduce ion diffusion distance, create more active sites, and provide large contact area between electrode and electrolyte, which endow them with unique advantages as electrode materials. In addition to decreasing the size of electrode materials, it is highly desirable to incorporate with other surface and structural engineering strategies during the synthesis process to further boost the super-capacitive performance of these electrode materials due to their strong synergistic effects and novel physicochemical properties induced.

2D materials based quantum dots (QDs) derived from their bulk counterparts can not only exhibit enhanced or novel physicochemical and electronic properties due to quantum

confinement effects, high surface-to-volume ratio, and structural defects,[239,240] but also maintain most intrinsic properties and crystalline structure of the corresponding bulk materials in a certain degree. [239, 240] Therefore, 2D materials based QDs could be ideal candidates for electrode materials of MSCs due to their short ion diffusion time, unique layer structure, large effective surface area, and rich edge planes and defects. Nonetheless, there are only a few reports on QDs based electrode materials for electrochemical energy storage devices, not to mention MSCs. Undoubtedly, it is a meaningful but challenging attempt to construct high-performance asymmetric MSCs using 2D materials based QDs. This is expected to not only take full advantage of the merits of the 2D materials based QDs and the synergistic effects between them, but also effectively solve the above-mentioned problems associated with MSCs.

In this work, surface and structural engineering accomplished by the reduction of size, the introduction of heteroatom element, and the production of structural defects has been employed to design and prepare defect-enriched nitrogen-doped graphene quantum dots (N-GQDs) and molybdenum disulfide quantum dots (MoS_2-QDs). Owing to their unique advantages, the resulting N-GQDs and MoS_2-QDs exhibit remarkable electrochemical performance as negative and positive electrode materials, respectively. Importantly, the obtained GQDs//MoS_2-QDs asymmetric MSCs display a large potential window (1.5 V), a high volumetric capacitance (1.8 $F \cdot cm^{-3}$), a high rate capability (up to 1000 $V \cdot s^{-1}$), a fast frequency response (with a small time-constant of 0.087 ms), and a long cycling stability (89.2 % retention after 10000 cycles). These appreciable electrochemical performances are mainly attributed to the respective merits of 2D N-GQDs and MoS_2-QDs, the 3D hierarchical structure assembled as well as the synergistic effect between them.

5.2 Experimental

5.2.1 Chemicals and materials synthesis

Chemicals: All the reagents purchased from Sigma-Aldrich were of analytical grade and used without further purification. The distilled de-ionized (DDI) water was obtained from a Millipore System.

Fabrication of N-GQDs: N-GQDs were synthesized by a typical solvothermal procedure. Firstly, reduced graphene oxides were prepared by the modified Hummers method and dispersed into DMF with the aid of bath sonication for 30 min. Afterward, the resulting mixture was transferred into an autoclave and kept at 200 °C for 12 h. After cooling down naturally, the mixture was then filtrated and then a brown-colored liquid product is obtained. Finally, the N-GQDs powder product was obtained by removing the DMF with the aid of a rotary evaporator.

Fabrication of MoS_2-QDs: MoS_2-QDs were fabricated by a facile ultrasonication method followed by solvothermal treatment. Firstly, the bulk MoS_2 powder dispersed in DMF was exfoliated by ultra-sonication for 2 h, using a tip sonicator with an output power of 300 W (KQ-3200E, Kunshan Ultrasonic Instruments Co. Ltd., Jiangsu, China). The resulting mixture was then transferred into an autoclave hold at 200 °C for 12 h. After a cooling process, the resulting suspensions were filtrated, and the obtained light-yellow filtrate was then centrifuged at 8000 rpm to further remove large nanosheets. Finally, the filtrate containing MoS_2-QDs was concentrated by a rotary evaporator.

5.2.2 Physicochemical characterizations

Scanning electron microscopy (SEM, LEO 1350) and transmission electron microscopy (TEM, JEOL 2010F) were employed to characterize the detailed morphology and structure of the samples. X-ray diffraction (XRD, MiniFlex 600, Rigaku) is used to reveal the crystal structure and phase of the samples. X-ray photoelectron spectroscopy (XPS) was performed to investigate the chemical compositions and states of the samples. Raman spectra were carried out on a Senterra Raman detection system (Bruker Optics) using a 532 nm laser. Atomic force microscopy (AFM, Cypher scanning probe microscope) was employed using the tapping mode to investigate the thickness of the samples.

5.2.3 Devices preparation and electrochemical characterizations

Preparation of asymmetric micro-supercapacitors: The N-GQDs//MoS_2-QDs asymmetric MSCs were fabricated by the following produces. Firstly, N-GQDs were deposited on one side of the interdigital finger electrodes by electrophoresis deposition in DMF dispersion containing GQDs (3.0 mg) at 80 V for 30 min. After washing with DDI water and drying in vacuum oven overnight, MoS_2-QDs were then assembled on the other side of the interdigital finger electrodes by same method in a DMF dispersion containing MoS_2 quantum dots (3.0 mg) at 80 V for 30 min.

Electrochemical measurements: For full-cell testing, all the electrochemical characterizations were conducted in a two-electrode system. The CV curves were studied with a potential window ranging from 0 to 1.5 V at different scan rates, while the GCD curves were tested at different current densities. The EIS were measured in the frequency ranging from 100 kHz to 0.1 Hz with 5 mV AC amplitude.

The specific capacitance (C) of the MSCs was estimated by the CV curve according to Equation (1):

$$C = \frac{1}{v \cdot V \cdot (V_f - V_i)} \int_{V_i}^{V_f} I(V)\, dV \qquad (F \cdot cm^{-3}) \qquad (5\text{-}1)$$

In addition, the specific capacitance (C) can also be obtained from the GCD curve according to Equation (2):

$$C = \frac{I \cdot \Delta t}{V \cdot \Delta V} \qquad (F \cdot cm^{-3}) \qquad (5\text{-}2)$$

The specific energy and power densities were calculated according to Equation (5-3) and (5-4), respectively:

$$E = \frac{C \cdot \Delta V^2}{7200} \qquad (Wh \cdot cm^{-3}) \qquad (5\text{-}3)$$

$$P = \frac{E \cdot 3600}{\Delta t} \qquad (Wh \cdot cm^{-3}) \qquad (5\text{-}4)$$

Where v, I(V), t, V, ΔV (V= V_f -V_i), E and P are the scan rate ($mV \cdot s^{-1}$), the response current (μA), the discharge time (s), the volume of electrode or device (cm^{-3}), the operating voltage (V), the energy density ($Wh \cdot cm^{-3}$), and the power density ($W \cdot cm^{-3}$), respectively.

5.3 Results and discussion

5.3.1 Characterization of negative electrode materials (N-GQDs)

The morphology and detail structure of N-GQDs are characterized by TEM and AFM, respectively. From low-resolution TEM images (**Figure 5-1a, 1b**), the resulting N-GQDs have a uniform and narrow distribution with size ranging from 1 to 5 nm (**Figure 5-1c**). The N-GQDs (inset of **Figure 5-1b**) possess high crystallinity with a lattice spacing of 0.26 nm,

which is consistent with the crystalline structure of graphite. [241] Moreover, as shown by AFM characterization (**Figure 5-1d-1f**), the thickness of N-GQDs is less than 1.5 nm, suggesting that the as-prepared N-GQDs are 1-3 graphene.[242] Additionally, X-ray photoelectron spectroscopy (XPS) is used to further study the chemical composition and bonding structure of elements in N-GQDs, with nitrogen-doped graphene nanosheets (N-GNSs) as a reference. XPS survey (**Figure 5-S1**) shows the co-existence of C, N, and O elements in the N-GQDs. It is noted that the C1s spectrum is deconvoluted into four peaks, corresponding to C-C (sp^2 C) at 284.8 eV, C-C (sp^3 C) at 286.2 eV, C=O at 287.5 eV, and O=C-O at 288.7 eV, respectively (**Figure 5-1g**). Obviously, the N-GQDs show a larger sp^3/sp^2 ratio (0.63) compared to that of N-GNSs (0.36), indicating the presence of more defects in the resulting N-GQDs. [243] As shown in **Figure 5-1h**, the N1s spectrum is divided into three peaks, which correspond to pyrrolic-N (at 398.6 eV), pyridinic-N (at 400.1 eV), and graphitic-N (at 401.9 eV). It is noted that the relative mount of pyridinic-N in N-GQDs is larger than that in N-GNSs, implying more pseudo-capacitance contribution of N-GQDs as the pyridinic-N is electrochemically reactive.[244, 245] In addition, the O1s spectrum (**Figure 5-1i**) is resolved into three peaks, which are assigned to C=O (531.2 eV), C-O (532.6 eV) and O=C-O (533.8 eV), respectively. Here, the residual oxygen functional groups and the incorporation of N into the carbon framework can not only tune the electron/donor characteristics and create more defects, but also facilitate the surface wettability and increase the contact area between N-GQDs and electrolyte, thus causing the enhancement of their electrochemical performances due to improved electronic conductivity, more active sites, and fast ions diffusion.[246-249]

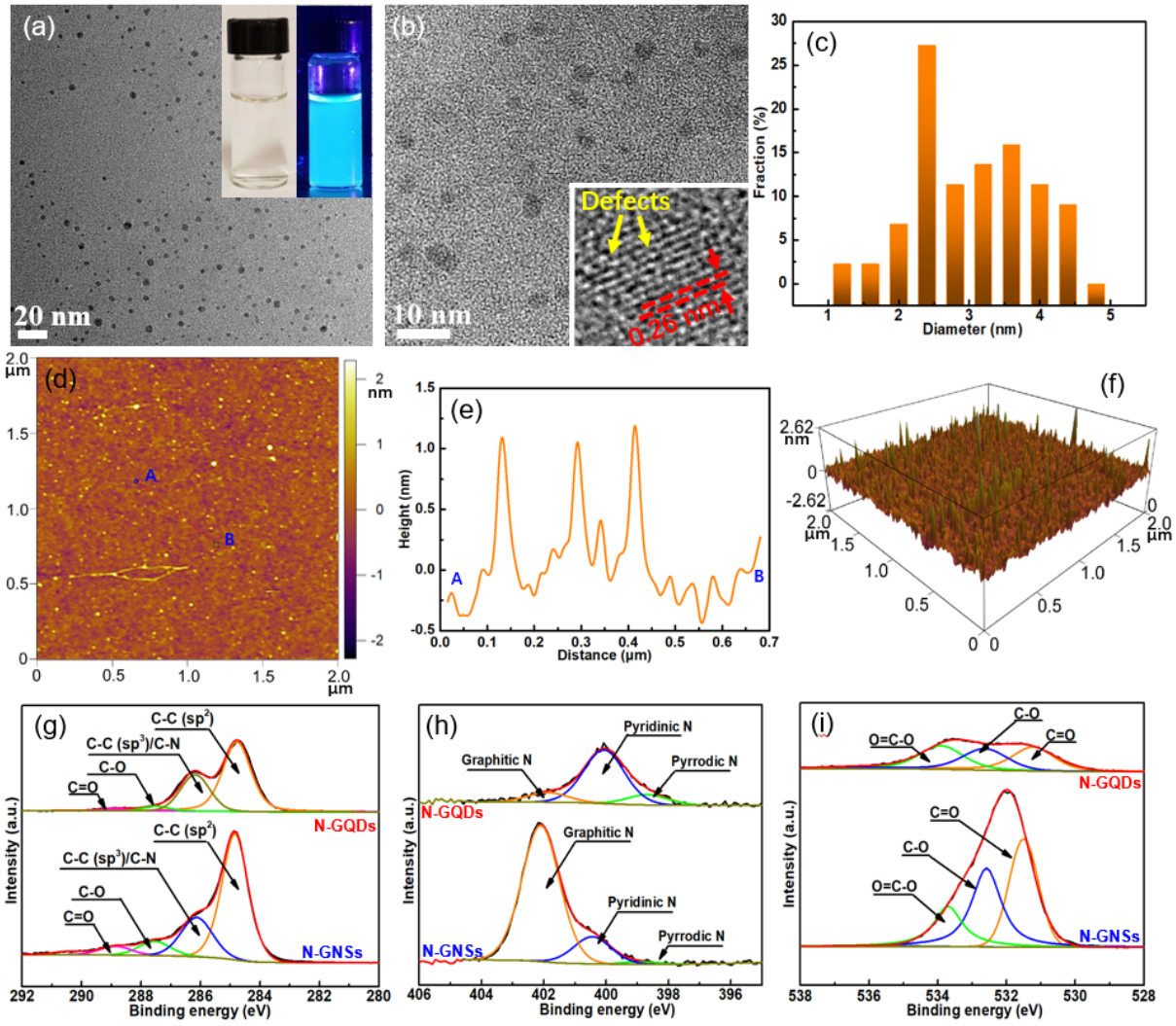

Figure 5-1 (a) Low-resolution TEM image of N-GQDs, (b) high-resolution TEM image of N-GQDs (Inset is the HRTEM lattice fringe.), and (c) its corresponding size distribution. (d) AFM image of N-GQDs and its corresponding (e) height and (f) 3D surface plot of the top-view. XPS spectra of N-GQDs: (g) C 1s, (h) N 1s, and (i) O 1s, respectively. Inset in Figure 5-1a is the photographs of N-GQDs under (left) visible light and (right) UV light, respectively.

The electrochemical performance of N-GQDs is first investigated by cyclic voltammetry (CV) technique at various scan rates and galvanostatic charge/discharge (GCD)

technique. As shown in **Figure 5-2a-c**, the CV curves of the N-GQDs at relatively low scan rates exhibit a rectangular shape, showing a typical characteristic of an ideal electric double-layer capacitor of N-GQDs. [247-250] Particularly, the CV curve (**Figure 5-2d**) still maintains a near-rectangle shape without obvious distortion even at 100 $V \cdot s^{-1}$, suggesting an excellent rate capability of the N-GQDs electrode. Notably, the discharge current shows a good linear relationship with scan rates ranging from 0.1 to 100 $V \cdot s^{-1}$ (**Figure 5-2e**), revealing a fast ion diffusion and a rapid charge transportation of N-GQDs electrode during the electrochemical process.

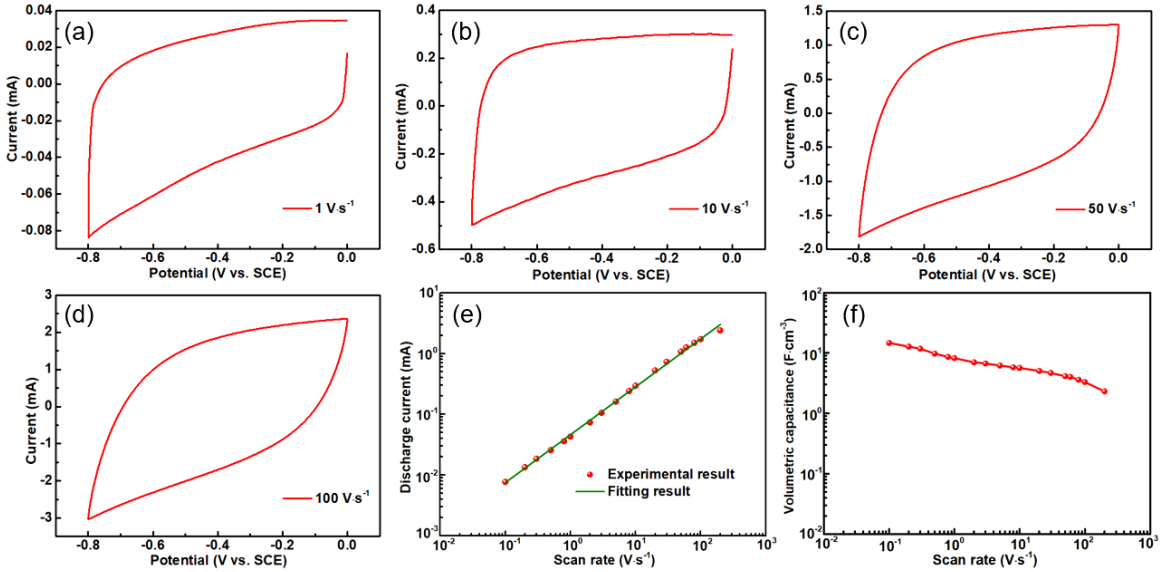

Figure 5-2 CV curves of N-GQDs negative electrode in 0.5 M Na_2SO_4 electrolyte at different scan rates: (a) 1 $V \cdot s^{-1}$, (b) 10 $V \cdot s^{-1}$, (c) 50 $V \cdot s^{-1}$, (d) 100 $V \cdot s^{-1}$, respectively. Evaluation of (e) the discharge current and (f) volumetric capacitance of N-GQDs negative electrode as a function of scan rates.

Meanwhile, its volumetric specific capacitance versus scan rates is displayed in **Figure 5-2f**. It is worth mentioning that the volumetric/area specific capacitance is more accurate

than that of the gravimetric value to estimate the performance of thin-film electrode as the mass loading of electrode is negligible. Notably, the largest volumetric specific capacitance is about 14.7 $F \cdot cm^{-3}$ at 0.1 $V \cdot s^{-1}$, while it still remains as high as 3.3 $F \cdot cm^{-3}$ (at 100 $V \cdot s^{-1}$) when the scan rate is increased by a factor of 1000, implying a high-power output capability of N-GQDs electrode. Moreover, the observed nearly linear and symmetric charge/discharge curves (**Figure 5-S2**) and no obvious "IR drop" further demonstrate its good capacitive behavior, high columbic efficiency, as well as small equivalent internal resistance. The specific capacitance of N-GQDs obtained from charge/discharge curve at 1.6 $A \cdot cm^{-3}$ is about 13.2 $F \cdot cm^{-3}$.

Additionally, the cycling stability, another critical parameter for evaluating the electrochemical performance of electrode material, is evaluated by CV curve at 1 $V \cdot s^{-1}$. It is observed that the N-GQDs electrode maintains 93% of its initial specific capacitance after 6000 repetitive cycles (**Figure 5-S3**), demonstrating its superior cycling life. The outstanding electrochemical performance of the N-GQDs electrode is mainly attributed to the distinctive features of N-GQDs including oxygen-rich functional groups, abundant defects, and good hydrophilicity. These features can provide more active sites, more accessible edges, and large contact area between N-GQDs and electrolyte. Furthermore, its unique 3D interconnected structure assembled, as well as the good contact between N-GQDs and current collector further allow the efficient access of electrolyte, the fast transport of ions/electrons, and the high utilization of the active material.

5.3.2 Characterization of positive electrode materials (MoS_2-QDs)

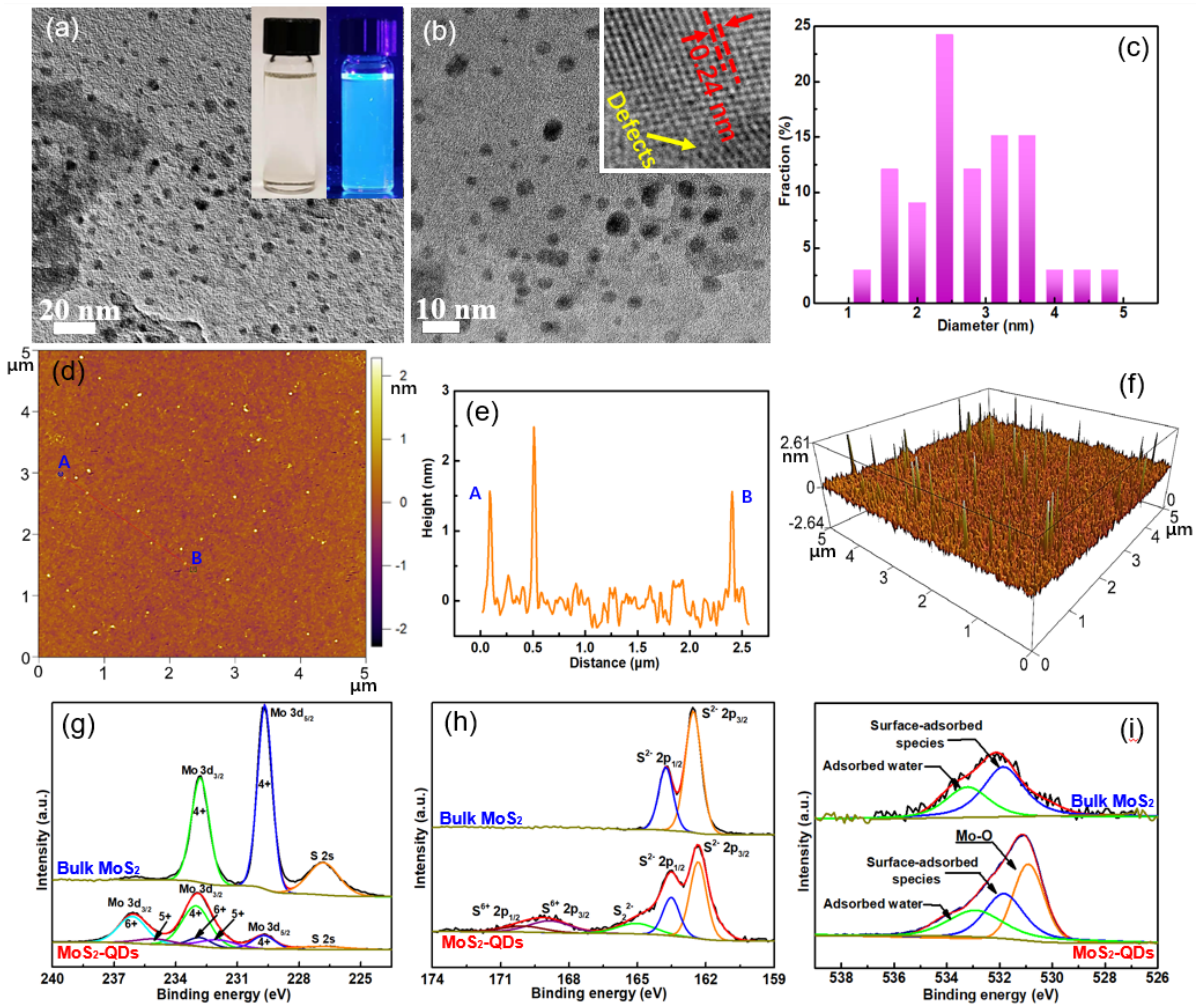

Figure 5-3 (a) Low-resolution TEM image of MoS_2-QDs, (b) high-resolution TEM image of MoS_2-QDs, and (c) its corresponding size distribution. (d) AFM image of MoS_2-QDs and its corresponding (e) height and (f) 3D surface plot of the top-view. XPS spectra of MoS_2-QDs: (g) Mo 3d, (h) S 2p, and (i) O1s, respectively. Inset in Figure 5-3a is the photographs of MoS_2-QDs under (left) visible light and (right) UV light, respectively.

The morphology and structure information of the resulting MoS_2-QDs are investigated by different characterization techniques as shown in **Figure 5-3**. The low resolution TEM images (**Figure 5-3a, 3b**) show that the size of MoS_2-QDs is uniform with a narrow size

distribution ranging from 1 to 5 nm (**Figure 5-3c**). The lattice spacing of MoS_2-QDs is about 0.24 nm (inset of **Figure 5-3b**), which is assigned to the (103) plane of the MoS_2 crystal. As shown in the AFM images (**Figure 5-3d-3f**), the thickness of the obtained MoS_2-QDs is about 1.5 nm, demonstrating their monolayer or few-layer (about 0.8-1.0 nm) nature. Moreover, XRD and Raman spectra are performed to evaluate the crystallinity and structure evolution of the MoS_2-QDs as compared to bulk MoS_2. It is noted that the weak (002) diffraction peak and the disappearance of other representative peaks in MoS_2-QDs diffraction pattern indicate that there are no long-range ordered crystal face and a limited portion of the crystalline lattice involved in diffraction, implying the MoS_2-QDs with ultrafine size and monolayer or few-layer structure (**Figure 5-S4**). [251-254] Furthermore, the Raman peaks of MoS_2-QDs (**Figure 5-S5**) at 380.3 cm^{-1} and 405.4 cm^{-1} are assigned to E^1_{2g} and A^1_g, respectively, and exhibit an apparent blueshift compared to those of bulk MoS_2. This is due to the E^1_{2g} stiffening and A_{1g} softening with the decrease of layer thickness.[255,256]

XPS is used to further clarify the valence state and chemical composition of the MoS_2-QDs. XPS survey (**Figure 5-S6**) confirms the presence of Mo, S and O elements in the resulting MoS_2-QDs. The high-resolution of Mo 3d spectrum (**Figure 5-3g**) shows three major peaks at 229.7, 232.9, and 236.1 eV, corresponding to Mo 3d5/2, Mo 3d3/2, and Mo 3d3/2, respectively. This indicates the dominance of the Mo^{+4} valence state in the product with the co-existence of the Mo^{+5} and Mo^{+6} valence states, indicating that there is a slight oxidation of the Mo^{+4} ions during the solvothermal reaction. [252,253,256] Meanwhile, the binding energy of S 2s (**Figure 5-3h**) slightly shifts from 227 to 226.6 eV, demonstrating that the S valence state in MoS_2 has been affected by the change of Mo valence state. Moreover, the S 2p spectrum confirms that the existing valence states of S in MoS_2-QDs are

S^{-2} and S^{+6}, indicating its small partial oxidization. Notably, the O 1s spectrum (**Figure 5-3i**) is divided into three peaks, which are attributed to the Mo-O bond, the surface-adsorbed species (OH-, O, or oxygen vacancies), and the adsorbed water, implying a partial oxidation of MoS_2-QDs. [252, 257] Such partial oxidation of MoS_2-QDs can introduce rich defects, thus modifying the electronic properties of MoS_2-QDs and producing more active surface area, which benefits to the enhancement of electrochemical performance.

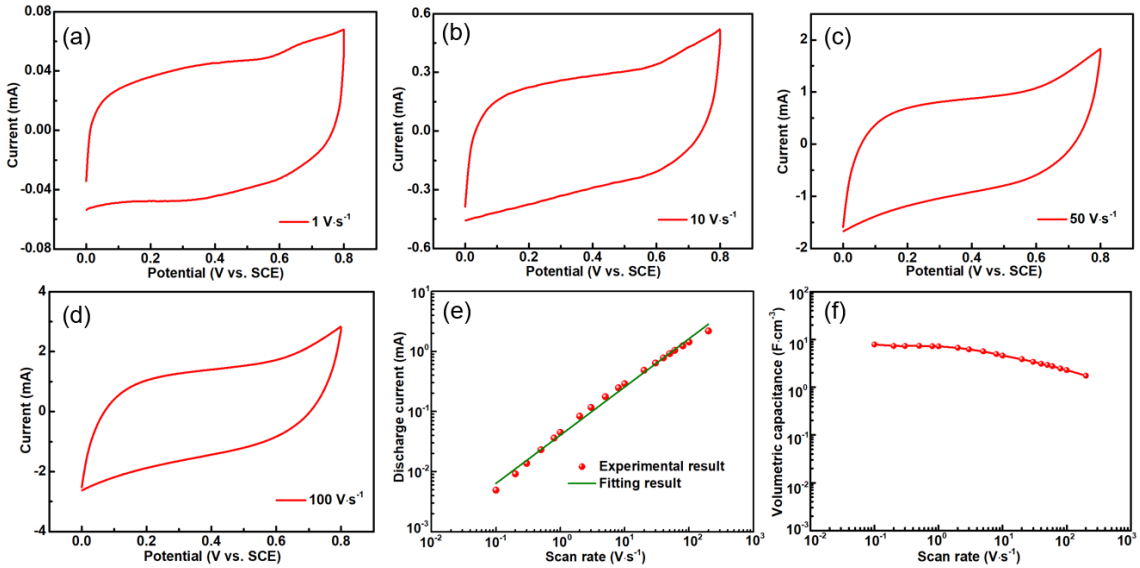

Figure 5-4 CV curves of MoS_2-QDs positive electrode in 0.5 M Na_2SO_4 electrolyte at different scan rates: (a) 1 $V \cdot s^{-1}$, (b) 10 $V \cdot s^{-1}$, (c) 50 $V \cdot s^{-1}$, (d) 100 $V \cdot s^{-1}$, respectively. Evaluation of (e) the discharge current and (f) volumetric capacitance of MoS_2-QDs positive electrode as a function of the scan rates.

As shown in **Figure 5-4a-c**, the CV curves of MoS_2-QDs show a good mirror image with respect to x-axis and a rapid current response at each end potential, illustrating a dominant Faradaic pseudo-capacitive behavior accompanying by a non-Faradaic double layer behavior of MoS_2-QDs. It should be mentioned that the associated energy storage mechanism is proposed as follows: [258, 259]

$$MoS_2 + Na^+ + e^- \leftrightarrow MoS - SNa^+ \quad (5\text{-}5)$$

$$(MoS_2)_{Surface} + Na^+ + e^- \leftrightarrow (MoS_2 - Na^+)_{Surface} \quad (5\text{-}6)$$

Where, the Faradaic process (5-5) is related to the intercalation/deintercalation of Na^+ into the interlayer structure of MoS_2-QDs, while the non-Faradaic process (5-6) is assigned to the adsorption/desorption of Na^+ at the interface of MoS_2-QDs/electrolyte. As the scan rate is up to 100 $V \cdot s^{-1}$, the CV curve still maintains a quasi-rectangular shape (**Figure 5-4d**), implying a low resistance and a high reversibility of the intercalation/deintercalation process of MoS_2-QDs electrode. This ultra-high scan rate of MoS_2-QDs electrode is almost three-orders of magnitude larger than those of conventional MoS_2-based SCs, [259-262] thus demonstrating an excellent rate capability of the MoS_2-QDs electrode. It is noted that there is a good linear dependence between discharge currents and scan rates up to at least 100 $V \cdot s^{-1}$ (**Figure 5-4e**), indicating a super-fast intercalation/deintercalation process of the MoS_2-QDs electrode. It is noted that its areal specific capacitance gradually decreases from 7.9 to 1.8 $F \cdot cm^{-2}$ when there is a three-orders of magnitude variation in scan rates ranging from 0.1 to 100 $V \cdot s^{-1}$ (**Figure 5-4f**). The good linearity and symmetrical triangle of the charge/discharge curve (**Figure 5-S7**) further implies good capacitor behavior of MoS_2-QDs electrode. Also, a high specific capacitance of 7.4 $F \cdot cm^{-3}$ is achieved according to the charge/discharge curve. Moreover, the MoS_2-QDs electrode shows a long-term cycling stability with 86.5 % retention of its initial capacitance after 6000 cycles (**Figure 5-S8**), which is much better than those of other reported MoS_2-based nanomaterials: MoS_2/PANI hybrid materials (60.9% retention after 1000 cycles), [263] MoS_2/RGO@PANI (82.5% retention after 3000 cycles),[264] MoS_2/Mn_3O_4 nanostructure (69.3% retention after 2000 cycles). [265] The superior durability is probably due to its unique 3D structure and the extreme small size of MoS_2-QD which can

provide a large contact area, effectively shorten the ion diffusion distance, and buffer the volume change during the intercalation/deintercalation processes.[266] The above electrochemical results indicate that MoS_2-QDs with nanoscale size, high surface area and enriched defects are promising positive material.

5.3.3 Characterization of N-GQDs//MoS_2-QDs micro-supercapacitors

Inspired by the excellent capacitive behavior of N-GQDs and MoS_2-QDs shown in half-cells, the asymmetric MSCs were successfully constructed with capacitor-type of N-GQDs and battery-type of MoS_2-QDs as negative and positive materials, respectively. In this configuration, a wide potential window can be obtained by taking the advantage of the different stable potential window of the N-GQDs anode and the MoS_2-QDs cathode as well as their relatively high overpotentials for hydrogen evolution reduction and oxygen evolution reduction. [266] The low-magnification SEM images (**Figure 5-5a, 5b**) show that the interdigital electrodes are alternately covered by N-GQDs and MoS_2-QDs, both of which exhibit a unique 3D structure, beneficial for easy access of electrolyte and fast transportation of electron/charge. The high-magnification SEM image (**Figure 5-5c**) shows that there are many free spaces among the N-GQDs with even a small fraction of N-GQDs agglomeration observed, facilitating the penetration of electrolyte and ensuring the active materials participate in the electrochemical reaction. As shown in the high-magnification SEM image (**Figure 5-5e**), there are lots of voids among the MoS_2-QDs produced during the assembling process, which can shorten the diffusion distance of the electrolyte ions and provide more surface-active sites for Faradic redox reaction. In addition, the cross-section SEM images

show that the thickness of the N-GQDs (**Figure 5-5d**) and MoS_2-QDs (**Figure 5-5f**) films are about 142 and 171 nm, respectively.

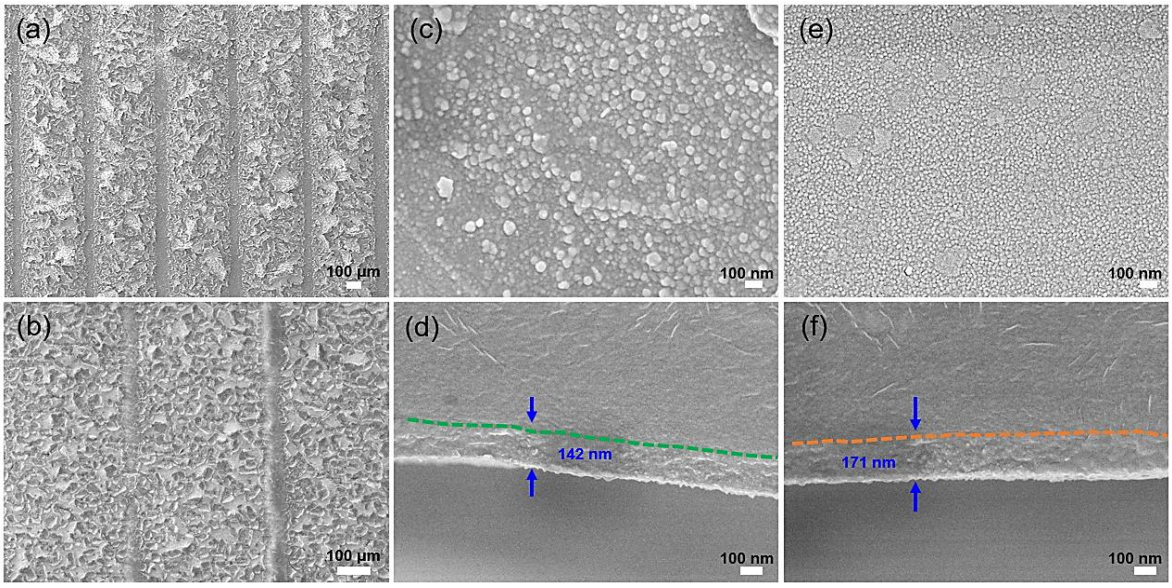

Figure 5-5 (a, b) Low magnification SEM images of the interdigital finger electrodes after the alternative deposition of N-GQDs and MoS_2-QDs. (c) High magnification SEM of N-GQDs finger electrode and (d) its corresponding cross-section image. (e) High-magnification SEM image of MoS_2-QDs finger electrode and (f) its corresponding cross-section image.

To achieve a large and stable potential window for asymmetric MSCs (**Figure 5-6a**), it is crucial to balance the charges between the N-GQDs negative electrode (q^-) and the MoS_2-QDs positive electrode (q^+). According to the typical CV curves of N-GQDs and MoS_2-QDs electrodes (**Figure 5-6b**), the ratio of deposition time between the negative material and the positive material is 0.91. The CV curves (**Figure 5-6c**) of the as-prepared N-GQDs//MoS_2-QDs asymmetric MSCs maintain a near rectangular shape when the operating voltage of the device gradually increases from 0.9 to 1.5 V, while it will deviate from the rectangle shape

due to polarization when the potential window is further extended. Furthermore, the energy storage of the device is proportional to the square of the potential window. Based on the above considerations, the operating voltage of the N-GQDs//MoS_2-QDs asymmetric MSCs is set to 1.5 V for further study in the subsequent research. The CV curves (**Figure 5-6d-f**) show a near perfect rectangle shape and no observable redox peaks when the scan rates are below 100 $V \cdot s^{-1}$, indicating a typical capacitive behavior of the MSCs with fast ion diffusion and rapid electron transportation. Importantly, the CV curve (**Figure 5-6g**) retains a nearly rectangle-shaped profile with slight distortion even at an ultra-high scan rate of 1000 $V \cdot s^{-1}$, which implies a small equivalent series resistance and an excellent rate capability of the microdevice. Remarkably, this ultra-high scan rate is close to three-orders of magnitude higher than those of conventional supercapacitors, and higher or comparable to those of reported MSCs based on onion-like carbon (200 $V \cdot s^{-1}$), [267] electrochemically reduced graphene oxide (400 $V \cdot s^{-1}$),[268] plasma reduced graphene (1000 $V \cdot s^{-1}$), [269] and vertically aligned CNTs (1000 $V \cdot s^{-1}$).[270] It is noted that the discharge currents show a linear dependence with the scan rates below 200 $V \cdot s^{-1}$ (**Figure 5-6h**), implying a fast surface-controlled kinetics; while with further increase of the scan rates, the linear relationship slightly deviates due to ohmic resistance. Impressively, a maximum volumetric capacitance of 1.8 $F \cdot cm^{-3}$ are achieved at 0.3 $V \cdot s^{-1}$ as shown in **Figure 5-6i**. This value is larger than or comparable to those of reported MSCs based on different materials: graphene/CNTs (1.08 $F \cdot cm^{-3}$),[271] onion-like carbon (1.10 $F \cdot cm^{-3}$),[267] laser reduction graphene (3.10 $F \cdot cm^{-3}$),[272] reduced graphene oxide/MnO_2/AgNW (4.42 $F \cdot cm^{-3}$). [227] Furthermore, the Ragone plot, which display the volumetric energy and power densities of N-GQDs//MoS_2-QDs asymmetric MSCs compared with other reported MSCs and commercial energy storage

devices, is shown in **Figure 5-S9**. Remarkably, the N-GQDs//MoS_2-QDs asymmetric MSCs show a volumetric energy density of 0.55 mWh·cm^{-3}, which is comparable to or larger than other reported MSCs such as laser-scribed graphene,[219, 272] laser scribed graphene/carbon nanotubes (CNTs), [273] graphene/CNTs,[271] graphene oxide/CNTs hybrid,[274] reduced graphene oxide/MnO_2/AgNW.[227] Particularly, this energy density is about two orders of magnitude larger than that of commercial electrolytic capacitors and comparable to that of thin-film lithium-ion batteries. [219, 267, 272]

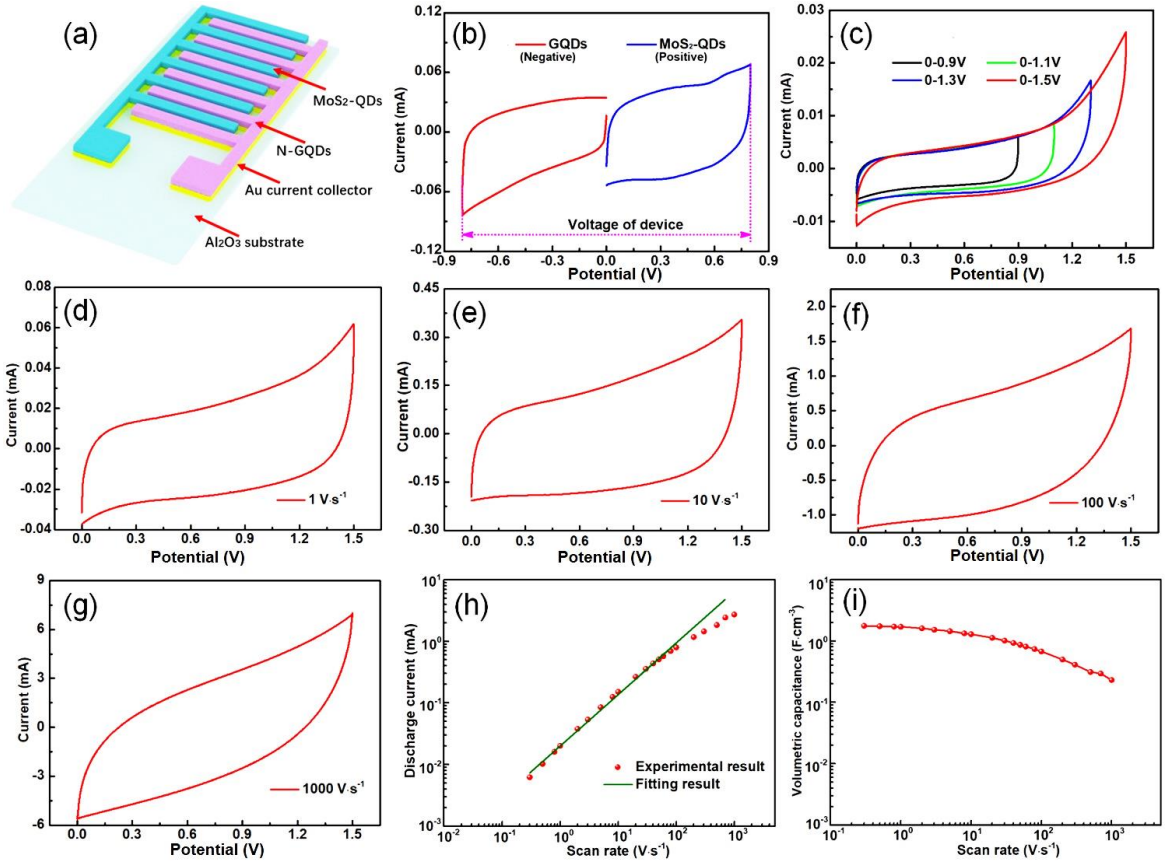

Figure 5-6 (a) Illustration of the as-prepared N-GQDs//MoS_2-QDs asymmetric MSCs. (b) Comparative CV curves of N-GQDs and MoS_2-QDs electrodes at 1 $V \cdot s^{-1}$. (c) CV curves of the N-GQDs//MoS_2-QDs asymmetric MSCs with different potential windows at 0.3 $V \cdot s^{-1}$. CV curves of the device measured at different scan rates: (d) 1 $V \cdot s^{-1}$, (e) 10 $V \cdot s^{-1}$, (f) 100 $V \cdot s^{-1}$, (g) 1000 $V \cdot s^{-1}$, respectively. (h) Plots of dependence between discharge currents and scan rates. (i) Volumetric capacitance of the cell as a function of scan rates ranging from 0.3 to 1000 $V \cdot s^{-1}$.

EIS is carried out to further characterize the MSCs and reveal the underlying reason behind its excellent electrochemical performance. As shown in **Figure 5-7a**, the Nyquist plot shows a near-straight line along the imaginary axis and no obvious semicircle is observed, suggesting a near-capacitive behavior and a small resistance of the resulting MSCs. Moreover, the relaxation time constant ($\tau_0 = 1/f_0$), another key factor of MSCs associated with diffusion manifested at low frequencies, is a quantitative evaluation of how fast the cell discharge all energy with efficiency more than 50%. The smaller value of the relaxation time constant, the faster power response capability of the MSCs. The relaxation time constant (τ_0) of the resulting N-GQDs//MoS_2-QDs asymmetric MSCs is 0.087 ms (**Figure 5-7b**), which is three-orders of magnitude smaller than those of conventional double-layer capacitors (1s) and much lower than those of most reported MSCs based on onion-like carbon (26 ms),[267] sulfuric-acid-treated poly(3,4-ethylenedioxythiophene):poly-(styrenesulfonate) (0.588 ms),[275] plasma reduced graphene (0.28 ms),[269] and electrochemically reduced graphene oxide (0.17-1 ms). [268] This result indicates a fast power response capability and a promising potential of the as-prepared device in the filtering application.

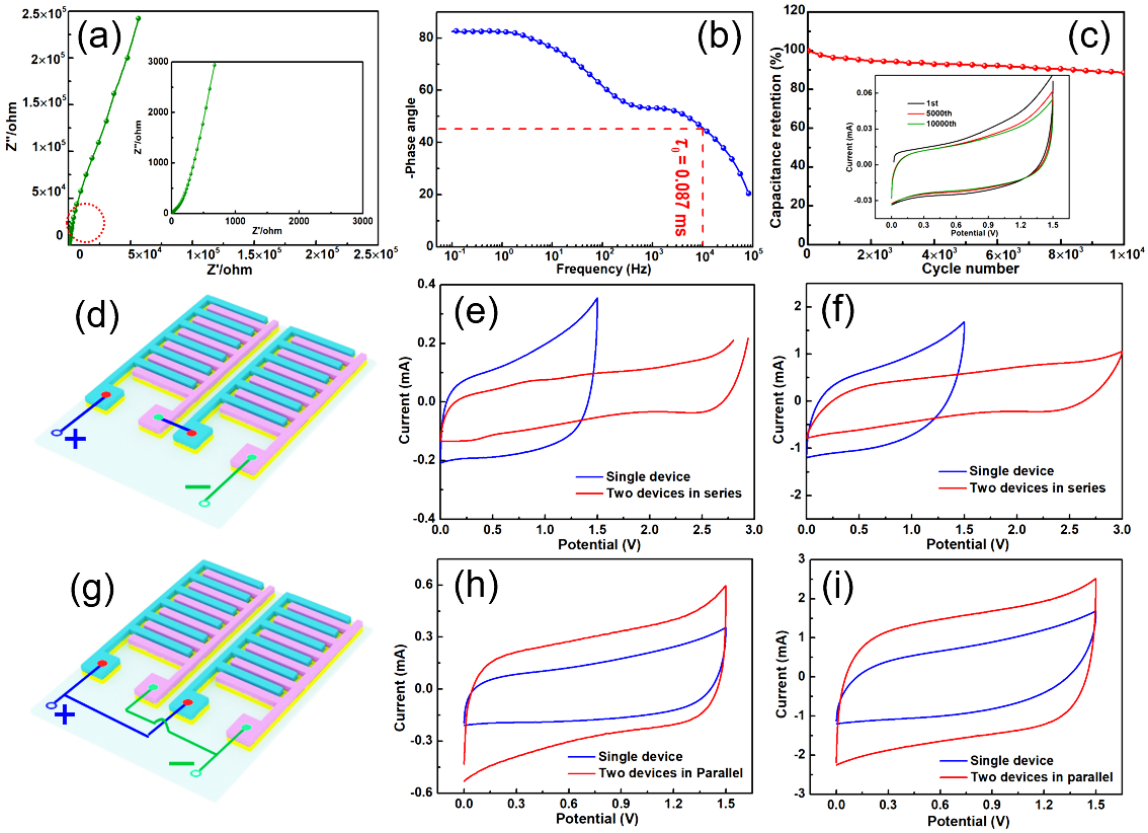

Figure 5-7 (a) Nyquist plot of the MSCs showing the imaginary part versus the real part. (b) Plot of impedance phase angle versus frequency. (d) Capacitance retention of the MSCs as a function of cycle number measured at the scan rate of 1 $V \cdot s^{-1}$ with 10000 cycles. (d) Illustration of two MSCs connected in series and corresponding CV curves: (e) 10 $V \cdot s^{-1}$, (f) 100 $V \cdot s^{-1}$. (g) Illustration of two MSCs connected in parallel and corresponding CV curves: (e) 10 $V \cdot s^{-1}$, (f) 100 $V \cdot s^{-1}$.

Furthermore, another important aspect for the evaluation of MSCs is the long-term cycling stability, which is performed by continuous CV testing. Notably, there is still 89.2 % retention of its initial capacity after 10000 cycles (**Figure 5-7c**), suggesting a good cycling stability. TEM characterization (**Figure 5-S10**) is carried out to check the structure change of the samples after the cycling test. It can be observed that both N-GQDs and MoS_2-QDs

can well maintain their structure without apparent changes, indicating good mechanical and electrochemical stability. Therefore, it is reasonable to deduce that the capacitance decay presented here is probably from the slight volume change of battery-type based material of MoS_2-QDs and the existence of side reaction occurring at the electrode/electrolyte interface in the large potential window. Additionally, in order to meet certain requirements of consumer electronic devices, it is necessary to connect two devices in series and parallel configuration (**Figure 5-S11**) to extend operating voltage and increase capacitance, respectively. As shown in **Figure 5-7d-7f**, the operating voltage of two devices connected in series is double compared to that of single cell, which indicates that the prepared devices are with a high consistency and obey the rule of series connection of capacitor. Importantly, the device keeps a rectangular shape even at 100 $V \cdot s^{-1}$, demonstrating an excellent rate capability. Moreover, when two MSCs are connected in parallel (**Figure 5-7g-7i**), the current is almost two times larger than that of a single MSC, suggesting it follows the principle of parallel connection of capacitor. In addition, the CV curve retains a near-rectangular shape at 100 $V \cdot s^{-1}$, further revealing the superior rate capability.

The excellent electrochemical performance of the N-GQDs//MoS_2-QDs asymmetric MSCs is by virtue of the following advantages derived from the special physicochemical properties of N-GQDs and MoS_2-QDs, the synergistic effect between them, and their unique 3D structures assembled. Firstly, the N-GQDs negative electrode maintains the distinctive features of N-GQDs including large active surface area, good hydrophilicity, and large contact area between electrode and electrolyte, which endow them with unique advantages as electrode materials. Also, the formed 3D hierarchical structure facilitates the easy access

of electrolyte, benefits the rapid transport of electrolyte ions, and accelerates the fast transport of electron. Secondly, the MoS_2-QDs positive electrode not only retains the merits of MoS_2-QDs such as two-dimensional layered crystal structure, high specific capacitance, and more accessible edge sites, but also possesses a unique 3D hierarchical architecture. These advantages of MoS_2-QDs electrode provide a large amount of electrochemical active sites, reduce ion diffusion distance, improve electron transportation from active materials to current collector, and promote fast and reversible intercalation/deintercalation process. Furthermore, the asymmetric configuration of MSCs proposed here can significantly increase energy density (due to the increase of the operating voltage) and still maintain excellent rate capability and long lifespan, which is mainly due to the synergistic effect between battery-type MoS_2-QDs electrode and capacitor-type N-GQDs electrode.

5.4 Conclusions

In summary, surface and structural engineering achieved by downsizing to quantum dot scale, doping heteroatom element, creating more structural defect and introducing rich functional group to 2D materials is employed to prepare defect-enriched nitrogen-doped graphene quantum dots (N-GQDs) and molybdenum disulfide quantum dots (MoS_2-QDs). By integrating the features of N-GQDs and MoS_2-QDs as well as the synergistic effect between them, the novel asymmetric MSCs are designed and constructed with capacitor-type N-GQDs as negative electrode and battery-type MoS_2-QDs as positive electrode. Particularly, the obtained MSCs display outstanding electrochemical performance compared to other reported MSCs, including a high energy density, an excellent rate capability, a fast frequency response capability, and a long-term cycling stability. The study presented here

provides a new insight for the construction of high-performance MSCs, and, more importantly, offers a new reference in designing other high-performance energy storage devices based on 2D materials QDs.

5.5 Supporting information

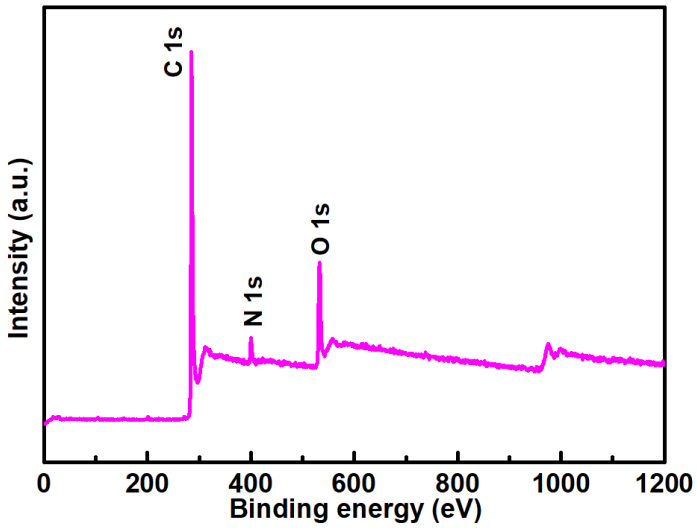

Figure 5-S1 XPS survey of N-GQDs.

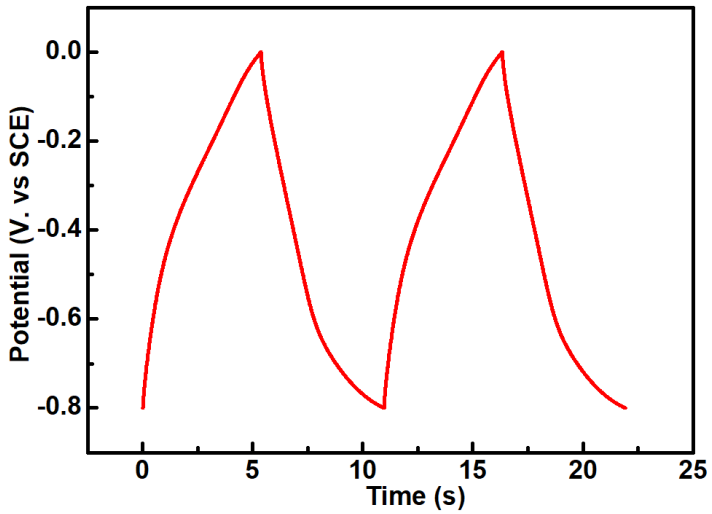

Figure 5-S2 Charge/discharge curves of N-GQDs at current density of 1.6 A·cm^{-3}.

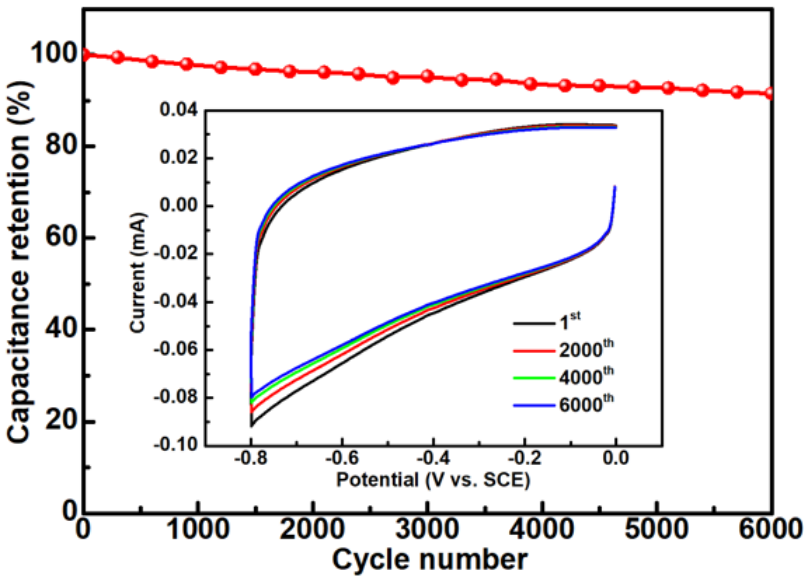

Figure 5-S3 Capacitance retention of N-GQDs after 6000 cycles measured by CV curve at the scan rate of 1 $V \cdot s^{-1}$. Inset is the corresponding CV curves under different cycle number (1^{st}, 2000^{th}, 4000^{th}, and 6000^{th}).

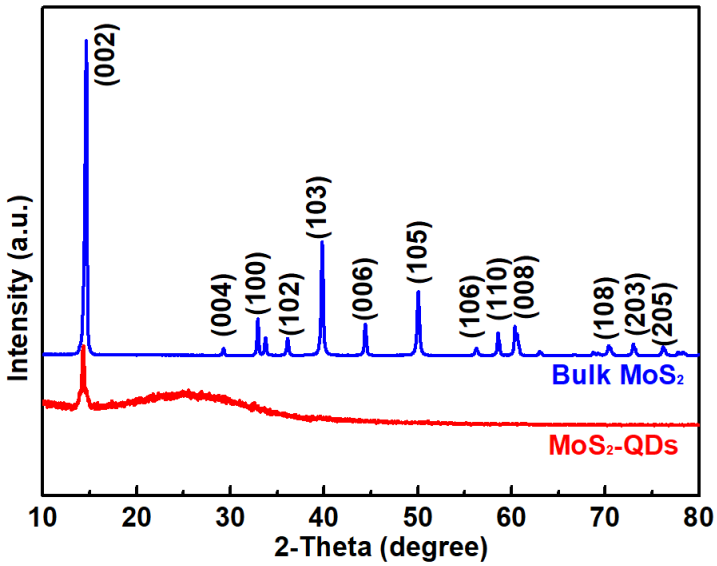

Figure 5-S4 XRD spectra of bulk MoS_2 and MoS_2-QDs.

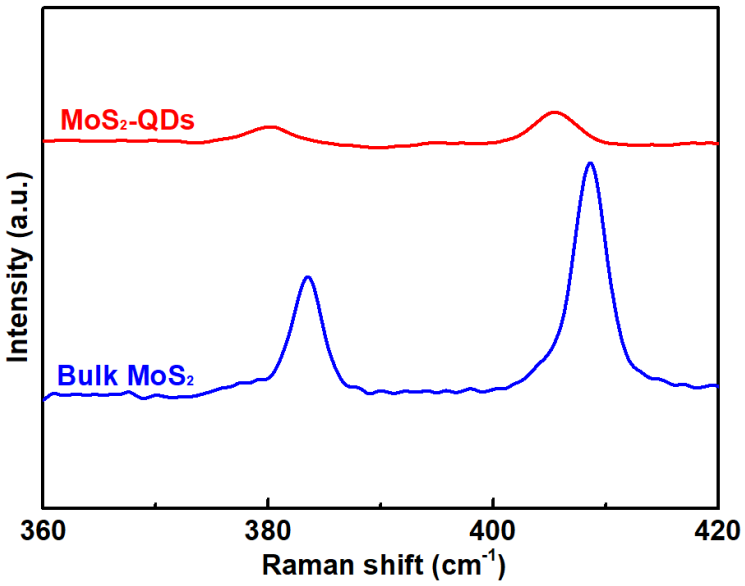

Figure 5-S5 Raman spectra of bulk MoS_2 and MoS_2-QDs.

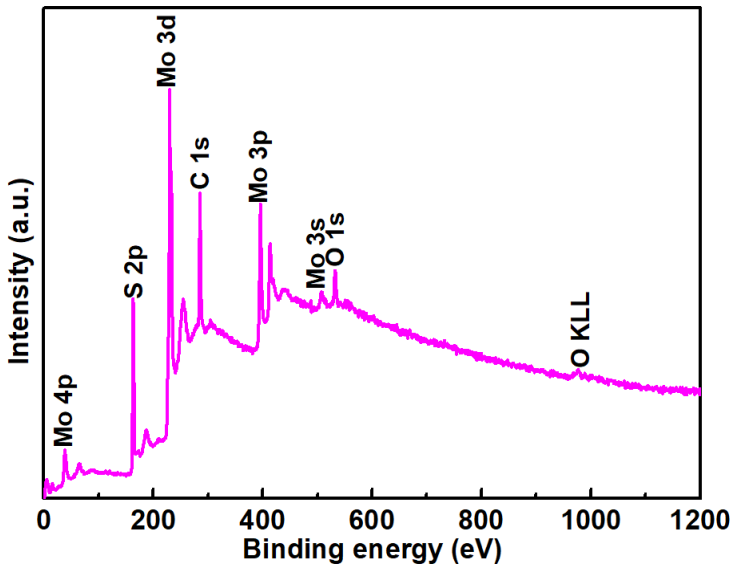

Figure 5-S6 XPS survey of MoS_2-QDs.

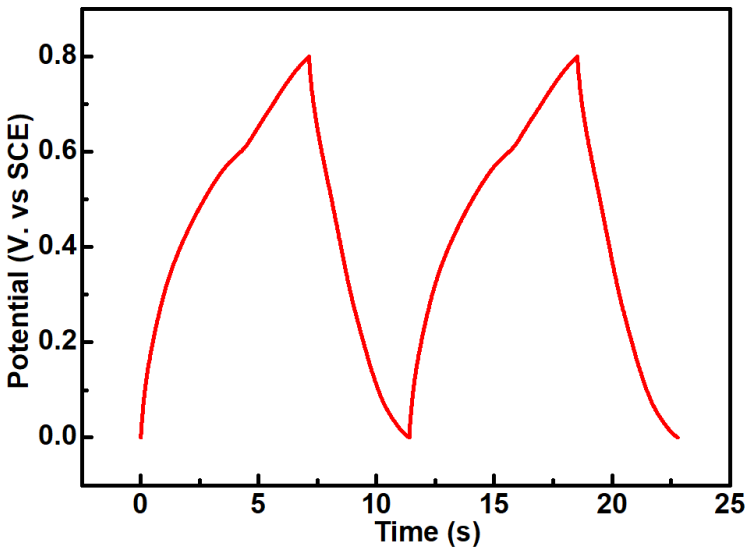

Figure 5-S7 Charge/discharge curves of MoS_2-QDs at current density of 1.6 $A \cdot cm^{-3}$.

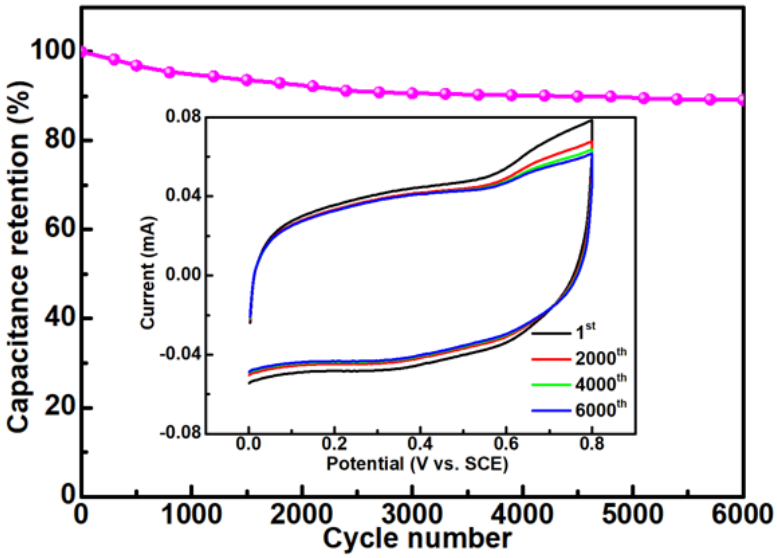

Figure 5-S8 Capacitance retention of MoS_2-QDs after 6000 cycles measured by CV curve at the scan rate of 1 $V \cdot s^{-1}$. Inset is the corresponding CV curves under different cycle number (1^{st}, 2000^{th}, 4000^{th}, and 6000^{th}).

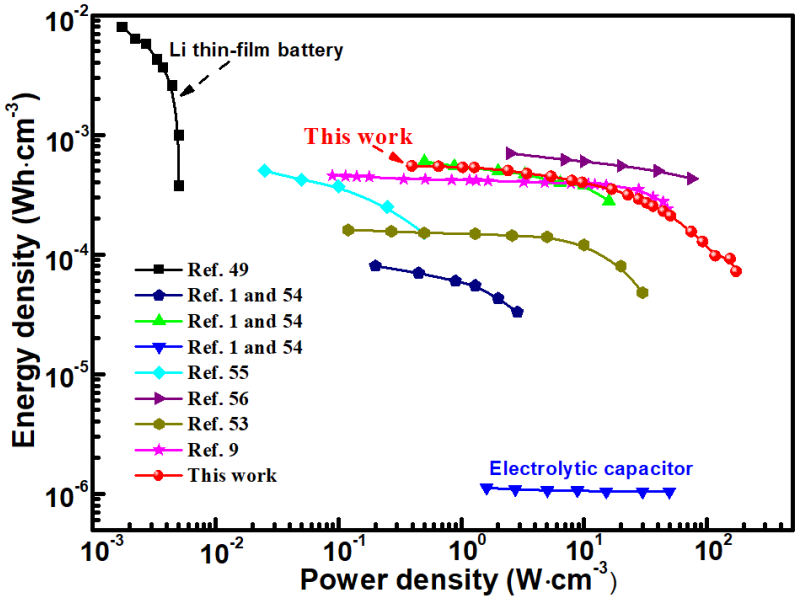

Figure 5-S9 Ragone plot exhibit the volumetric energy density and power density of N-GQDs//MoS_2-QDs asymmetric MSCs compared with other reported MSCs and commercial energy storage devices.

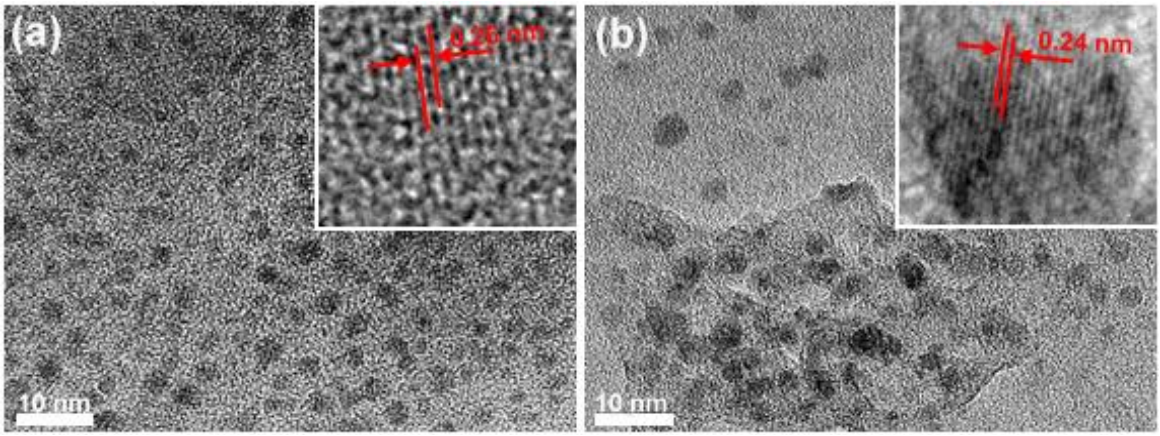

Figure 5-S10 TEM characterizations of (a) N-GQDs electrode and (b) MoS_2-QDs electrode in N-GQDs//MoS_2-QDs device after cycling test.

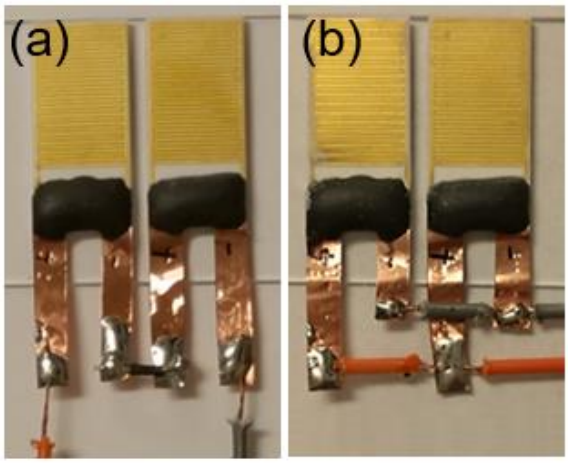

Figure 5-S11 Photos of two N-GQDs//MoS_2-QDs asymmetric MSCs devices connected in (a) series and (b) parallel, respectively.

Chapter 6: Conclusions and future work

In this thesis, to meet the new and higher requirements of consumer electronic devices, several types of emerging concept SCs including lithium ion hybrid capacitors, fiber-shaped MSCs, and in-plane MSCs have been developed by adopting different strategies and technologies. Specifically, the entire process involves the synthesis of nanomaterials, electrode preparation, and device assembly as well as electrochemical performance evaluation, while at the same time advanced characterization techniques are used to reveal the structure-property-performance relationship of these new nanomaterials, thus further understanding the underlaying reason behind the excellent electrochemical performance. More details of the conclusions of the previous chapters and the novelty of these works as well as the future work proposed are summarized as follows.

6.1 Summary and conclusions

In **Chapter 3**, novel high-performance Li-ion hybrid supercapacitors (LIHSs) has been successfully constructed using 3D graphene wrapped MoO_3 nanobelt foam (MoO_3/GNSs) and polyaniline/graphene foam derived carbon (PANI/GNSs) as the anode and cathode materials, respectively. By integrating the merits of these two graphene foam-enhanced materials, the as-prepared LIHSs possess a wide voltage range of 0.0-3.8 V, a long cycle life up to 3000 cycles with 90% capacity retention, and an improved ultrahigh energy density of 128.3 $Wh \cdot kg^{-1}$ (power density of 182.2 $W \cdot kg^{-1}$), which also remains of 44.1 $Wh \cdot kg^{-1}$ even at high power density of 13.5 $kW \cdot kg^{-1}$. First-principle calculation reveals that the introduction of graphene dramatically reduces the diffusion energy barrier of Li^+ adsorbed on the surface of MoO_3, thus improving its electrochemical performance. This work provides a promising

direction for the design of high-performance LIHSs by the development of graphene-based hybrid materials which combine the positive properties of each components.

In **Chapter 4**, inspired by nanostructured biological fiber (human hair), fiber-shaped micro-supercapacitors (FMSCs) have been successfully constructed for the first time with coaxial human hair/Ni/reduced graphene oxide (rGO)/MnO_2 fiber as the cathode and coaxial human hair/Ni/rGO fiber as the anode. Importantly, the as-prepared FMSCs show outstanding electrochemical performance such as a wide potential window (1.8 V), a high volumetric energy density (1.81 $mWh \cdot cm^{-3}$), a fast frequency response (τ_0 = 55 ms), and an excellent rate capability (up to 20000 $mV \cdot s^{-1}$). Furthermore, the human hair/Ni/rGO/MnO_2 fiber can be woven into a simple textile-shaped framework, and shows good flexibility even bended to 90˚, demonstrating its promising potential in wearable devices as power source. In addition, the strategy presented here offers a new reference for the design of fiber-shaped electrode as well as fiber-shaped MSCs.

In **Chapter 5**, two kinds of two-dimensional (2D) materials-based quantum dots are prepared using surface and structural engineering achieved by downsizing to quantum dot scale, doping heteroatom element, creating more structural defect and introducing rich functional group. By integrating the features of defect-enriched nitrogen-doped graphene quantum dots (N-GQDs) and molybdenum disulfide quantum dots (MoS_2-QDs) as well as the synergistic effect between them, the obtained asymmetric MSCs display a large operating voltage up to 1.5 V (far exceeding that of most reported MSCs), a high energy density (0.55 $mWh \cdot cm^{-3}$), an excellent rate capability (up to 1000 $V \cdot s^{-1}$), a fast frequency response capability (with the shortest time-constant of 0.087 ms so far), and a long-term cycling stability (with 89.2 % retention after 10000 cycles). In this work, the surface and

structure engineering strategies are proved to be an effective strategy to boost the electrochemical performance of MSCs by tailoring the physicochemical properties of the 2D materials. More importantly, this is the first report on asymmetric MSCs whose negative and positive electrodes are composed of 2D QDs-based materials, which could provide the guidance for the construction of high-performance MSCs.

6.2 Proposed future work

Based on the achieved results presented in this thesis, some suggestions for future work are proposed as follows.

1. Further investigation on the rational selection and design of organic electrolytes as well as the volumetric and gravimetric specific capacity. In **Chapter 3**, we have made many efforts for the design and construction of 3D GNS/MoO_3 nanocomposite anode material and 3D GNS/PANI nanocomposite cathode material, which are expected to address the mismatch problems between the anode and cathode electrodes in terms of the electrochemical kinetics and the specific capacitance. However, the flammable EC-based electrolytes have potential safety issues under overcharge or short circuit conditions. Thus, new electrolyte systems with large potential window, wide operating temperature, low-cost, and safety as well as good compatibility with both anode and cathode materials are highly desired. In addition, it is also necessary to consider how to obtain the high volumetric and gravimetric capacity of LIHSs at the same time. This is because most graphene-based electrode materials with relatively high surface area and rich porosity have small tap density, which usually leads to small volumetric capacitance of the device, thus limiting practical applications. Besides, a good understanding of the chemical interactions between the

components not only benefits to the rational design and controllable preparation of advanced electrode materials with unique surface and structural properties, thus achieving the optimal performance, but also provides some guidance and rules for other researchers.

2. Developing efficient and large-scale techniques to produce fiber-based electrode with enhanced performance as well as exploring new gel electrolytes. In **Chapter 4**, the energy density of the obtained fiber-shaped micro-supercapacitors have been improved compared with other reported results, but it is still lower those of batteries. One of the main reasons is that the natural fiber (human hair) only provide the mechanical flexibility, so the inside of the composite fiber does not contribute to energy storage. Moreover, the preparation process presented in this work is a little bit of complication, so it is necessary to search for low-cost and scalable strategies for fiber electrode synthesis and asymmetric SCs assembly. Additionally, the current PVA-KOH gel electrolyte is risky for wearable/portable devices due to its corrosion, so the appropriate gel/solid-state electrolyte should be considered.

3. Understanding the underlying reason behind the excellent electrochemical performance with the assisting of advanced techniques and further improve the energy density through innovation in all aspects. In **Chapter 5**, the asymmetric MSCs, whose negative and positive electrodes are composed of 2D QDs-based materials, are reported. Importantly, benefiting from the merits of these two 2D QDs-based electrode, the device exhibits superior electrochemical performance such as a large operating voltage, an excellent rate capability, a fast frequency response capability, and a long-term cycling stability. However, the deep reason for the excellent electrochemical performance are still unclear, so it is necessary to use some advanced characterizations such as in-situ XRD or TEM to

investigate the energy storage mechanism. Moreover, to make it practical application, the energy density should be further enhanced by innovating the configuration of electrode. Among them, the 3D electrode based MSCs is very promising (**Figure 6-1**), which can obviously increase the mass loading of active materials and thus increase the energy density without scarifying the power density. Furthermore, the packing issues should be considered, which plays an important role in sealing and maintaining the electrolyte during use. Other than those, it also needs to seek accurate, efficient, low-cost technologies to realize the large-scale production, which determines the practical application of in-plane MSCs.

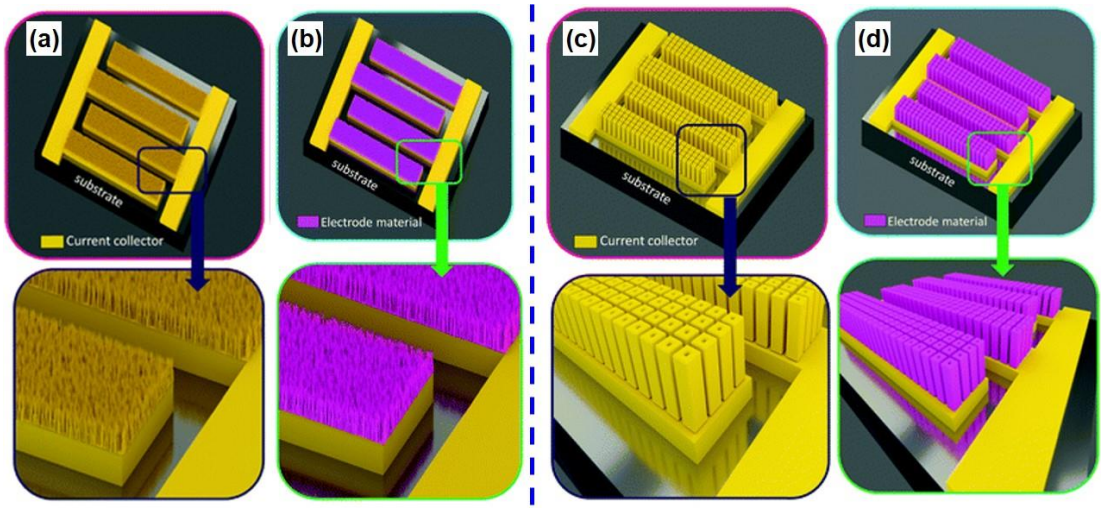

Figure 6-1 3D architecture adopted to further improve the energy density of MSCs: the nano-architecture electrode (a) before and (b) after coating with active material; the micro-architecture electrode (c) before and (d) after coating with active material. Reproduced with permission.[276] Copyright 2019, The Royal Society of Chemistry.

References

1. C. Lu,Y. H. Huang, Y. J. Wu, J. Li, J. P. Cheng, *J. Power Sources* **2018**, *394*, 9-16.

2. Y. Zhang, H. Feng, X. Wu, L. Wang, A. Zhang, T. Xia, H. Dong, X. Li, L. Zhang, *Int. J. Hydro. Energ.* **2009**, *34*, 4889-4899.

3. B. Yang, J. Wang, X. Zhang, J. Wang, H. Shu, S. Li, T. He, C. Lan, T. Yu, *J. Power Sources* **2020**, *448*, 227444.

4. G. Xu, P. Nie, H. Dou, B. Ding, L. Li, X. Zhang, *Mater. Today* **2017**, *20*, 191-209.

5. Y. Deng, Y. Xie, K. Zou, X. Ji, *J. Mater. Chem. A* **2016**, *4*, 1144-1173.

6. J. Yan, S. Li, B. Lan, Y. Wu, P. S. Lee, *Adv. Funct. Mater.* **2020**, *30*, 1902564.

7. M. Zhi, C. Xiang, J. Li, M. Li, N. Wu, *Nanoscale* **2013**, *5*, 72-88.

8. G. Zhang, X. W. Lou, *Adv. Mater.* **2013**, *25*, 976-979.

9. Z. Yu , B. Duong , D. Abbitt, J. Thomas, *Adv. Mater.* **2013**, *25*, 3302-3306.

10. H. Yan, K. Zhu, X. Liu, Y. Wang, Y. Wang, D. Zhang, Y. Lu, T. Peng, Y. Liu, Y. Luo, *RSC Adv.* **2020**, *10*, 8760-8765.

11. W. Tang, L. Liu, S. Tian, L. Li, Y. Yue, Y. Wu, K. Zhu, *Chem. Commun.* **2011**, *47*, 10058-10060.

12. L. F. Chen, Z. -Y. Yu, X. Ma, Z. -Y. Li, S. -H. Yu, *Nano Energy* **2014**, *9*, 345-354.

13. Y. Zhu, S. Murali, M. D. Stoller, K. J. Ganesh, W. Cai, P. J. Ferreira, A. Pirkle, R. M. Wallace, K. A. Cychosz, M. Thommes, D. Su, E. A. Stach, R. S. Ruoff, *Science* **2011**, *332*, 1537-1541.

14. B. Li, F. Dai, Q. Xiao, L. Yang, J. Shen, C. Zhang, M. Cai, *Energy Environ. Sci.* **2016**, *9*, 102-106.

15. Z. Huang, L. Li, Y. Wang, C. Zhang, T. Liu, *Compos. Commun.* **2018**, *8*, 83-91.

16. M. D. Stoller, S. Murali, N. Quarles, Y. Zhu, J. R. Potts, X. Zhu, H. -W. Ha, R. S. Ruoff, *Phys. Chem. Chem. Phys.* **2012**, *14*, 3388-3391.

17. W. Fu, E. Zhao, R. Ma, Z. Sun, Y. Yang, M. Sevilla, A. B. Fuertes, A. Magasinski, G. Yushin, *Adv. Energy Mater.* **2020**, *10*, 1902993.

18. S. Li, T. Wang, W. Zhu, J. Lian, Y. Huang, Y. -Y. Yu, J. Qiu, Y. Zhao, Y. -C. Yong, H. Li, *J. Mater. Chem. A*, 2019, 7, 693-703.

19. J. Xu, Y. Li, L. Wang, Q. Cai, Q. Li, B. Gao, X. Zhang, K. Huo, P. K. Chu, *Nanoscale* **2016** *8*, 16761-16768.

20. Y. Ma, H. Chang, M. Zhang, Y. Chen, *Adv. Mater.* **2015** *27*, 5296-5308.

21. L. Chen, W. Zhai, L. Chen, D. Li, X. Ma, Q. Ai, X. Xu, G. Hou, L. Zhang, J. feng, P. Si, L. Ci, *J. Power Sources* **2018**, *392*, 116-122.

22. K. Karthikeyan, S. Amaresh, V. Aravindan, H. Kim, K. S. Kang, Y. S. Lee, *J. Mater. Chem. A* **2013**, *1*, 707-714.

23. F. Sun, J. Gao, X. Liu. L. Wang, Y. Yang, X. Pi. S. Wu, Y. Qin, *Electrochim. Acta* **2016**, *213*, 626-632.

24. Q. Wang, Y. Ma, X. Liang, D. Zhang, M. Miao, *Chem. Eng. J.* **2019**, *371*, 145-153.

25. L. Liu, Y. Feng, W. Wu, *J. Power Sources* **2019**, *410-411*, 69-77.

26. Y. Zheng, Y. Yang, S. Chen, Q. Yuan, *CrystEngComm* **2016**, *18*, 4218-4235.

27. H. Xu, X. Hu, Y. Sun, H. Yang, X. Liu, Y. Huang, *Nano Res.* **2015**, *8*, 1148-1158.

28. J. Han, H. Wang, Y. Yue, C. Mei, J. Chen, C. Huang, Q. Wu, X. Xu, *Carbon* **2019**, *149*, 1-18.

29. M. -X. Guo, S. -W. Bian, F. Shao, S. Liu, Y. -H. Peng, *Electrochim. Acta* **2016**, *209*,

486-497.

30. L. N. Jin, P. liu, C. Jin, J. -N. Zhang, S. -W. Bian, *J. Colloid Interface Sci.* **2018**, *510*, 1-11.

31. Y. Da, J. Liu, L. Zhou, X. Zhu, X. Chen, L. Fu, *Adv. Mater.* **2019**, *31*, 1802793.

32. S. Bellani, E. Petroni, A. E. D. R. Castillo, N. Curreli, B. Martín-García, R. Oropesa-Nuñez, M. Prato, F. Bonaccorso, *Adv. Funct. Mater.* **2019**, *29*, 1807659.

33. Z. Niu, L. Zhang, L. Liu, B. Zhu, H. Dong, X. Chen, *Adv. Mater.* **2013**, *25*, 4035-4042.

34. Z. -S. Wu, X. Feng, H. -M. Cheng, *Natl. Sci. Rev.* **2014**, *1*, 277-292.

35. C. Zhang, M. P. Kremer, A. Seral-Ascaso, S. -H. Park, N. McEvoy, B. Anasori, Y. Gogotsi, V. Nicolosi, *Adv. Funct. Mater.* **2018**, *28*, 1705506.

36. K. Guo, Y. Wan, N. Yu, L. Hu, T. Zhai, H. Li, *Energy Storage Mater.* **2018**, *11*, 144-151.

37. D. Qi, Y. Liu, Z. Liu, L. Zhang, X. Chen, *Adv. Mater.* **2017**, *29*, 1602802.

38. J. Zeng, L. Wei, X. Guo, *J. Mater. Chem. A* **2017**, *5*, 25282-25292.

39. A. González, E. Goikolea, J. A. Barrena, R. Mysyk, *Renew. Sust. Energ. Rev.* **2016**, *58*, 1189-1206.

40. K. L. Van Aken, M. Beidaghi, Y. Gogotsi, *Angew. Chem. Int. Ed.* **2015**, *54*, 4806-4809.

41. X. Zhang, X. Wang, L. jiang, H. Wu, C. Wu, J. Su, *J. Power Sources* **2012**, *216*, 290-296.

42. I. Shown, A. Ganguly, L. -C. Chen, K. -H. Chen, *Energy Sci. Eng.* **2015** *3*, 2-26.

43. M. Yang, B. Cheng, H. Song, X. Chen, *Electrochim. Acta* **2010** *55*, 7021-7027.

44. P. Simon, Y. Gogotsi, *Nat Mater.* **2008**, *7*, 845-854.

45. K. Jurewicz, C. Vix-Guterl, E. Frackowiak, S. Saadallah, M. Reda, J. Parmentier, J. Patarin, F. Béguind, *J. Phys. Chem. Solids.* **2004**, *65*, 287-293.

46. J. A. Fernández, T. Morishita, M. Toyoda, M. Inagaki, F. Stoeckli, T. A. Centeno, *J. Power Sources* **2008**, *175*, 675-679.

47. J. Jiang, L. Zhang, X. Wang, N. Holm, K. Rajagopalan, F. Chen, S. Ma, *Electrochim Acta* **2013**, *113*, 481-489.

48. R. Dash, J. Chmiola, G. Yushin, Y. Gogotsi, G. Laudisio, J. Singer, J. Fischer, S. Kucheyev, *Carbon* **2006**, *44*, 2489-2497.

49. A. E. Kravchik, J. A. Kukushkina, V. V. Sokolov, G. F. Tereshchenko, *Carbon* **2006**, *44*, 3263-3268.

50. Z. Wu, L. Li, J. -M. Yan, X. -B. Zhang, *Adv. Sci.* **2017**, *4*, 1600382.

51. Y. Zhang, S. -J. Park, *Carbon* **2017**, *122*, 287-297.

52. S. Kong, K. Cheng, T. Ouyang, Y. Gao, K. Ye, G. Wang, D. Cao, *Electrochim. Acta* **2017**, *246*, 433-442.

53. S. Korkmaz, F. Meydaneri Tezel, İ. A. Kariper, *J. Alloys Compd.*, **2018**, *754*, 14-25.

54. F. Shi, L. Li, X. -L. Wang, C. -D. Gu, J. -P. Tu, *RSC Adv.* **2014**, *4*, 41910-41921.

55. Z. -H. Huang, Y. Song, D. -Y. Feng, Z. Sun, X. Sun, X. -X. Liu, *ACS Nano* **2018**, 12, *4*, 3557-3567.

56. M. -K. Wu, C. Chen, J. -J. Zhou, F. -Y. Yi, K. Tao, L. Han, *J. Alloys Compd.* **2018**, *734*, 1-8.

57. Z. Xiao, L. Fan, B. Xu, S. Zhang, W. Kang, Z. Kang, H. Lin, X. Liu, S. Zhang, D. Sun, *ACS Appl. Mater. Interfaces* **2017**, *9*, 41827-41836.

58. W. Xu, S. Dai, G. Liu, Y. Xi, C. Hu, X. Wang, *Electrochim. Acta* **2016**, *203*,1-8.

59. W. Bi, J. Wang, E. P. Jahrman, G. T. Seidler, G. Gao, G. Wu, G. Cao, *Small* **2019**, *15*, 1901747.

60. W. Guo, Y. Li, Y. Tang, S. Chen, Z. Liu, L. Wang, Y. Zhao, F. Gao, *Electrochim. Acta* **2017**, *229*, 197-207.

61. D. Yan, W. Wang, X. Luo, C. Chen, Y. Zeng, Z. Zhu, *Chem. Eng. J.* **2018**, *334*, 864-872.

62. X. Liu, F. Wei, Y. Sui, J. Qi, Y. He, Q. Meng, *J. Alloys Compd.* **2018**, *735*, 1339-1343.

63. Y. Gao, Y. Xia, H. Wan, X. Xu, S. Jiang, *Electrochim. Acta* **2019**, *301*, 294-303.

64. X. Feng, Y. Huang, C. Li, X. Chen, S. Zhou, X. Gao, C. Chen, *Chem. Eng. J.* **2019**, *368*, 51-60.

65. K. Xu, J. Yang, J. Hu, *J. Colloid Interface Sci.* **2018**, *511*, 456-462.

66. C. Lu, W. Liu, H. Pan, B. K. Tay, X. Wang, K. Liang, X. Wei, *Appl. Surf. Sci.* **2018**, *439*,1019-1025.

67. W. Liu, C. Lu, K. Liang, B. K. Tay, *J. Mater. Chem. A* **2014**, *2*, 5100-5107.

68. W. He, C. Wang, F. Zhuge, X. Deng, X. Xu, T. Zhai, *Nano Energy* **2017**, *35*, 242-250.

69. G. Kaur, R. Adhikari, P. Cass, M. Bown, P. Gunatillake, *RSC Adv.* **2015**, *5*, 37553-37567.

70. Y. Wang, Y. Ding, X. Guo, G. Yu, *Nano Res.* **2019**, *12*, 1978-1987.

71. A. Rudge, J. Davey, I. Raistrick, S. Gottesfeld, J. P. Ferraris, *J. Power Sources* **1994**, *47*, 89-107.

72. R. Kötz, M. Carlen, *Electrochim Acta* **2000**, *45*, 2483-2498.

73. C. Arbizzani, M. Mastragostino, F. Soavi, *J Power Sources* **2001**, *100*, 164-170.

74. E. Frackowiak, V. Khomenko, K. Jurewicz, K. Lota, F. Béguin, *J. Power Sources* **2006**, *153*, 413-418.

75. J. Xu, K. Wang, S. -Z. Zu, B. -H. Han, Z. Wei, *ACS Nano* **2010**, *4*, 5019-5026.

76. C. Zhong, Y. Deng, W. Hu, J. Qiao, L. Zhang, J. Zhang, *Chem. Soc. Rev.* **2015**, *44*,

7484-7539.

77. G. Wang, L. Zhang, J. Zhang, *Chem Soc Rev.* **2012**, *41*, 797-828.

78. M. Galiński, A. Lewandowski, I. Stępniak, *Electrochim. Acta* **2006**, *51*, 5567-5580.

79. H. Liu, Y. Liu, J. Li, *Phys. Chem. Chem. Phys.* **2010**, *12*, 1685-1697.

80. X. Zhang, B. He, Y. Zhao, Q. Tang, *J. Power Sources* **2018**, *379*, 60-67.

81. S. Banerjee, K. K. Kar, *J. Environ. Chem. Eng.* **2016**, *4*, 299-310.

82. C. Y. Bon, L. Mohammed, S. Kim, M. Manasi, P. Isheunesu, K. S. Lee, J. M. Ko, *J. Ind. Eng.Chem.* **2018**, *68*, 173-179.

83. S. Banerjee, K. K. Kar, *J. Appl. Polym. Sci.* **2016**, *133*, 42952.

84. Y. Wang, Y. Song, Y. Xia, *Chem. Soc. Rev.* **2016**, *45*, 5925-5950.

85. H. Wang, L. Pilon, *J. Phys. Chem. C* **2011**, *115*, 16711-16719.

86. L. Chen, Y. Liu, Y. Zhao, N. Chen, L. Qu, *Nanotechnology* **2016**, *27*, 032001.

87. B. E. Conway, V. Briss, J. Wojtowicz, *J. Power Sources.* **1997**, *66*, 1-14.

88. J. P. Zheng, P. J. Cygan, T. R. Jow, *J. Electrochem.Soc.* **1995**, *142*, 2699-2703.

89. W. Wei, X. Cui, W. Chen, D. G. Ivey, *Chem. Soc. Rev.* **2011**, *40*, 1697-1721.

90. D. Chao, H. J. Fan, *Chem* **2019**, *5*, 1359-1361.

91. J. Dong, Y. He, Y. Jiang, S. Tan, Q. Wei, F. Xiong, Z. Chu, Q. An, L. Mai, *Nano Energy* **2020**, *73*, 104838.

92. J. Liu, J. Wang, C. Xu, H. Jiang, C. Li, L. Zhang, J. Lin, Z. X. Shen, *Adv. Sci.* **2018**, *5*, 1700322.

93. F. -X. Ma, L. Yu, C. -Y. Xu, X. W. Lou, *Energy Environ. Sci.* **2016**, *9*, 862-866.

94. X. -Y. Yu, L. Yu, X. W. Lou, *Adv. Energy Mater.* **2016**, *6*, 1501333.

95. L. Yu, G. Guan, W. Xiao, X. W. Lou, *Adv. Energy. Mater.* **2015**, *5*, 1500981.

96. E. Lim, C. Jo, J. Lee, *Nanoscale* **2016**, *8*, 7827-7833.

97. H. Kim, M. -Y. Cho, M. -H. Kim, K. -Y. Park, H. Gwon, Y. Lee, K. C. Roh, K. Kang, *Adv. Energy Mater.* **2013**, *3*, 1500-1506.

98. Q. Wang, Z. H. Wen, J. H. Li, *Adv. Funct. Mater.* **2006**, *16*, 2141-2146.

99. G. Gourdin, P. H. Smith, T. Jiang, T. N. Tran, D. Qu, *J. Electroanal. Chem.* **2013**, *688*, 103-112.

100. H. -G. Jung, N. Venugopal, B. Scrosati, Y. -K. Sun, *J. Power Sources* **2013**, *221*, 266-271.

101. H. Wang, C. Zhu, D. Chao, Q. Yan, H. J. Fan, *Adv. Mater.* **2017**, *29*, 1702093.

102. H. Seiler, *J Appl Phys.* **1983**, *54*, R1-R18.

103. Q. Meng, K. Cai, Y. Chen, L. Chen, *Nano Energy* **2017**, *36*, 268-285.

104. T. Liu, Y. Li, *InfoMat.* **2020**, DOI: 10.1002/inf2.12105.

105. S. Ratha, A. K. Samantara, **2018**, Characterization and Performance Evaluation of Supercapacitor. In: Supercapacitor: Instrumentation, Measurement and Performance Evaluation Techniques.

106. M. Xiao, J. Nie, Z. Zhang, X. Lu, Z. Wang, *Nano Energy* **2018**, *47*, 43-50.

107. Q. Zhang, C. Cai, J. Qin, B. Wei, *Nano Energy* **2014**, *4*, 14-22.

108. W. Liu, J. Li, K. Feng, A. Sy, Y. Liu, L. Lim, G. Lui, R. Tjanda, L. Rasenthiram, G. Chiu, A. Yu, *ACS Appl. Mater. Interfaces* **2016**, *8*, 25941-25953.

109. Z. Jian, V. Raju, Z. Li, Z. Xing, Y. -S. Hu, X. Ji, *Adv. Funct. Mater.* **2015**, *25*, 5778-5785.

110. X. Li, J. T. Xu, L. Mei, Z. J. Zhang, C.Y. Cui, H. K. Liu, J. M. Ma, S. X. Dou, *J. Mater. Chem. A* **2015**, *3*, 3257-3260.

111. K. Naoi, S. Ishimoto, J. Miyamoto, W. Naoi, *Energy Environ. Sci.* **2012**, *5*, 9363-9373.

112. V. Aravindan, J. Gnanaraj, Y. -S. Lee, S. Madhavi, *Chem. Rev.* **2014**, *114*, 11619-11635.

113. H. Wang, Y. Zhang, H. Ang, Y. Zhang, H. T. Tan, Y. Zhang, Y. Guo, J. B. Franklin, X. L. Wu, M. Srinivasan, H. J. Fan, Q. Yan, *Adv. Funct. Mater.* **2016**, *26*, 3082-3093.

114. R. Wang, J. Lang, P. Zhang, Z. Lin, X. Yan, *Adv. Funct. Mater.* **2015**, *25*, 2270-2278.

115. M. Yang, Y. Zhong, J. Ren, X. Zhou, J. Wei, Z. Zhou, *Adv. Energy Mater.* **2015**, *5*, 1500550.

116. X. Wang, G. Li, Z. Chen, V. Augustyn, X. Ma, G. Wang, B. Dunn, Y. Lu, *Adv. Energy Mater.* **2011**, *1*, 1089-1093.

117. R. Gokhale, V. Aravindan, P. Yadav, S. Jain, D. Phase, S. Madhavi, S. Ogale, *Carbon* **2014**, *80*, 462-471.

118. V. Aravindan, N. Shubha, W. Ling Chui, S. Madhavi, *J. Mater. Chem. A* **2013**, *1*, 6145-6151.

119. G. Li, Z. Yang, Z. Yin, H. Guo, Z. Wang, G. Yan, Y. Liu, L. Li, J. Wang, *J. Mater. Chem. A* **2019**, *7*, 15541-15563.

120. K. Leng, F. Zhang, L. Zhang, T. Zhang, Y. Wu, Y. Lu, Y. Huang, Y. Chen, *Nano Res.* **2013**, *6*, 581-592.

121. V. Aravindan, D. Mhamane, W. Ling Chui, S. Ogale, S. Madhavi, *ChemSusChem* **2013**, *6*, 2240-2244.

122. V. Augustyn, P. Simon, B. Dunn, *Energy Environ. Sci.* **2014**, *7*, 1597-1614.

123. Y. Gong, S. Yang, Z. Liu, L. Ma, R. Vajtai, P. M. Ajayan, *Adv. Mater.* **2013**, *25*, 3979-3984.

124. V. Raju, J. Rains, C. Gates, W. Luo, X. Wang, W. F. Stickle, G. D. Stucky, X. Ji, *Nano Lett.* **2014**, *14*, 4119-4124.

125. Y. -S. Lin, J. -G. Duh, M. -H. Hung, *J. Phys. Chem. C* **2010**, *114*, 13136-13141.

126. H. Huang, W. Zhu, X. Tao, Y. Xia, Z. Yu, J. Fang, Y. Gan, W. Zhang, *ACS Appl. Mater. Interfaces* **2012**, *4*, 5974-5980.

127. K. Feng, H. W. Park, X. Wang, D. U. Lee, Z. Chen, *Electrochim. Acta.* **2014**, *139*, 145-151.

128. L. Shen, X. Zhang, H. Li, C. Yuan, G. Cao, *J. Phys. Chem. Lett.* **2011**, *2*, 3096-3101.

129. H. Su, T. Wang, S. Zhang, J. Song, C. Mao, H. Niu, B. Jin, J. Wu, Y. Tian, *Solid State Sci.* **2012**, *14*, 677-681.

130. B. Ahmed, M. Shahid, D. H. Nagaraju, D. H. Anjum, M. N. Hedhili, H. N. Alshareef, *ACS Appl. Mater. Interfaces* **2015**, *7*, 13154-13163.

131. G. Zhao, N. Zhang, K. Sun, *J. Mater. Chem. A* **2013**, *1*, 221-224.

132. Q. Xia, H. Zhao, Z. Du, J. Wang, T. Zhang, J. Wang, P. Lv, *J. Power Sources* **2013**, *226*, 107-111.

133. J. Zhou, N. Lin, L. Wang, K. Zhang, Y. Zhu, Y. Qian, *J. Mater. Chem. A* **2015**, *3*, 7463-7468.

134. P. G. Bruce, B. Scrosati, J. -M. Tarascon, *Angew. Chem., Int. Ed.* **2008**, *47*, 2930-2946.

135. E. Hosono, T. Kudo, I. Honma, H. Matsuda, H. S. Zhou, *Nano Lett.* **2009**, *9*, 1045-1051.

136. L. Yang, L. Liu, Y. Zhu, X. Wang, Y. Wu, *J. Mater. Chem.* **2012**, *22*, 13148-13152.

137. X. -C. Dong, H. Xu, X. -W. Wang, Y. -X. Huang, M. B. Chan-Park, H. Zhang, L. -H. Wang, W. Huang, P. Chen, *ACS Nano* **2012**, *6*, 3206-3213.

138. M. Wu, S. Meng, Q. Wang, W. Si, W. Huang, X. Dong, *ACS Appl. Mater. Interfaces* **2015**, *7*, 21089-21094.

139. X. Dong, X. Wang, J. Wang, H. Song, X. Li, L. Wang, M. B. Chan-Park, C. M. Li, P. Chen, *Carbon* **2012**, *50*, 4865-4870.

140. Z. Zuo, T. Kim, I. Kholmanov, H. Li, H. Chou, Y. Li, *Small* **2015**, *11*, 4922-4930.

141. X. Li, J. Shen, W. Sun, X. Hong, R. Wang, X. Zhao, X. Yan, *J. Mater. Chem.* A **2015**, *3*, 13244-13253.

142. X. Zhou, Z. Bai, M. Wu, J. Qiao, Z. Chen, *J. Mater. Chem.* A **2015**, *3*, 3343-3350.

143. Y. Xu, K. Sheng, C. Li, G. Shi, *ACS Nano* **2010**, *4*, 4324-4330.

144. J. Yin, X. Xia, L. Xiang, X. Zhao, *Carbon* **2010**, *48*, 2958-2967.

145. K. Dewangan, N. Sinha, K. Sharma, A. Pandey, N. Munichandraiah, N. Gajbhiye, *CrystEngComm* **2011**, *13*, 927-933.

146. D. Chen, M. Liu, L. Yin, T. Li, Z. Yang, X. Li, B. Fan, H. Wang, R. Zhang, Z. Li, H. Xu, H. Lu, D. Yang, J. Sun, L. Gao, *J. Mater. Chem.* **2011**, *21*, 9332-9342.

147. Y. Xie, F. Cheong, Y. Zhu, B. Varghese, R. Tamang, A. Bettiol, C. Sow, *J. Phys. Chem. C* **2010**, *114*, 120-124.

148. C. Feng, H. Gao, C. Zhang, Z. Guo, H. Liu, *Electrochim. Acta* **2013**, *93*, 101-106.

149. Y. Mao, W. Li, X. Sun, Y. Ma, J. Xia, Y. Zhao, X. Lu, J. Gan, Z. Liu, J. Chen, P. Liu, Y. Tong, *CrystEngComm* **2012**, *14*, 1419-1424.

150. J. Li, X. Liu, *CrystEngComm* **2014**, *16*, 184-190.

151. M. A. Bica de Moraes, B. C. Trasferetti, F. P. Rouxinol, R. Landers, S. F. Durrant, J. Scarmínio, A. Urbano, *Chem. Mater.* **2003**, *16*, 513-520.

152. F. Xie, W. Choy, C. Wang, X. Li, S. Zhang, J. Hou, *Adv. Mater.* **2013**, *25*, 2051-2055.

153. Z. Zhang, R. Yang, Y. Gao, Y. Zhao, J. Wang, L. Huang, J. Guo, T. Zhou, P. Lu, Z. Guo, Q. Wang, *Sci. Rep.* **2014**, *4*, 6797-6805.

154. X. -Y. Xue, Z. -H. Chen, L. -L. Xing, S. Yuan, Y. -J. Chen, *Chem. Commun.* **2011**, *47*, 5205-5207.

155. V. Augustyn, J. Come, M. A. Lowe, J. W. Kim, P. L. Taberna, S. H. Tolbert, H. D. Abruña, P. Simon, B. Dunn, *Nat. Mater.* **2013**, *12*, 518-522.

156. T. Brezesinski, J. Wang, J. Polleux, B. Dunn, S. H. Tolbert, *J. Am. Chem. Soc.* **2009**, *131*, 1802-1809.

157. E. Lim, C. Jo, H. Kim, M. -H. Kim, Y. Mun, J. Chun, Y. Ye, J. Hwang, K. -S. Ha, K. C. Roh, K. Kang, S. Yoon, J. Lee, *ACS nano* **2015**, *9*, 7497-7505.

158. L. Kong, C. Zhang, J. Wang, W. Qiao, L. Ling, D. Long, *ASC Nano* **2015**, *9*, 11200-11208.

159. M. Trchová, E. N. Konyushenko, J. Stejskal, J. Kovářová, G. Ćirić-Marjanović, *Polym. Degrad. Stab.* **2009**, *94*, 929-938.

160. L. Lin, H. Niu, M. Zhang, W. Song, Z. Wang, X. Bai, *Appl. Surf. Sci.* **2008**, *254*, 7250-7254.

161. D. Zhang, X. Wen, L. Shi, T. Yan, J. Zhang, *Nanoscale* **2012**, *4*, 5440-5446.

162. Z. Tong, Y. Yang, J. Wang, J. Zhao, B. -L. Su, Y. Li, *J. Mater. Chem. A* **2014**, *2*, 4642-4651.

163. S. Stewart, P. Albertus, V. Srinivasan, I. Plitz, N. Pereira, G. Amatucci, J. Newman, *J. Electrochem. Soc.* **2008**, *155*, A253-A261.

164. H. Wang, C. Guan, X. Wang, H. Fan, *Small* **2015**, *11*, 1470-1477.

165. Z. Fan, J. Yan, T. Wei, L. Zhi, G. Ning, T. Li, F. Wei, *Adv. Funct. Mater.* **2011**, *21*, 2366-2375.

166. J. Yan, Z. Fan, T. Wei, W. Qian, M. Zhang, F. Wei, *Carbon* **2010**, *48*, 3825-3833.

167. J. Gamby, P. L. Taberna, P. Simon, J. F. Fauvarque, M. Chesneau, *J. Power Sources* **2001**, *101*, 109-116.

168. M. Wu, C. Huang, K. Lin, *J. Power Sources* **2009**, *186*, 557-564.

169. W. Liu, K. Feng, Y. Zhang, T. Yu, L. Han, G. Lui, M. Li, G. Chiu, P. Fung, A. Yu, *Nano Energy* **2017**, *34*, 491-499.

170. L. Bao, X. Li, *Adv. Mater.* **2012**, *24*, 3246-3252.

171. Q. Chen, Y. Meng, C. Hu, Y. Zhao, H. Shao, N. Chen, L. Qu, *J. Power Sources* **2014**, *247*, 32-39.

172. D. S. Yu, Q. H. Qian, L. Wei, W. C. Jiang, K. L. Goh, J. Wei, J. Zhang, Y. Chen, *Chem. Soc. Rev.* **2015**, *44*, 647-662.

173. X. Shi, L. Tian, S. Wang, P. Wen, M. Su, H. Xiao, P. Das, F. Zhou, Z. Liu, C. sun, Z. – S. Wu, X. Bao, *J. Energy Chem.* **2021**, *52*, 284-290.

174. D. Yu, S. Zhai, W. Jiang, K. Goh, L. Wei, X. Chen, R. Jiang, Y. Chen, *Adv. Mater.* **2015**, *27*, 4895-4901.

175. M. Beidaghi, Y. Gogotsi, *Energy Environ. Sci.* **2014**, *7*, 867-884.

176. J. Ren, W. Bai, G. Guan, Y. Zhang, H. Peng, *Adv. Mater.* **2013**, *25*, 5965-5970.

177. X. Cai, M. Peng, X. Yu, Y. Fu, D. Zou, *J. Mater. Chem. A* **2014**, *2*, 1184-1200.

178. L. Dong, C. Xu, Y. Li, C. Wu, B. Jiang, Q. Yang, E. Zhou, F. Kang, Q. -H. Yang, *Adv. Mater.* **2016**, *28*, 1675-1681.

179. Q. Wang, X. Wang, J. Xu, X. Ouyang, X. Hou, D. Chen, R. Wang, G. Shen, *Nano*

Energy **2014**, *8*, 44-51.

180. Z. Yu, J. Thomas, *Adv. Mater.* **2014**, *26*, 4279-4285.

181. Y. Li, K. Sheng, W. Yuan, G. Shi, *Chem. Commun.* **2013**, *49*, 291-293.

182. X. Wang, B. Liu, R. Liu, Q. Wang, X. Hou, D. Chen, R. Wang, G. Shen, *Angew. Chem. Int. Ed.* **2014**, *53*, 1849-1853.

183. S. T. Senthilkumar, J. Kim, Y. Wang, H. Huang, Y. Kim, *J. Mater. Chem. A* **2016**, *4*, 4934-4940.

184. W. Xiong, X. Hu, X. Wu, Y. Zeng, B. Wang, G. He, Z. Zhu, *J. Mater. Chem. A* **2015**, *3*,17209-17216.

185. V. T. Le, H. Kim, A. Ghosh, J. Kim, J. Chang, Q. A. Vu, D. T. Pham, J. -H. Lee, S. -W. Kim, Y. H. Lee, *ACS Nano* **2013**, *7*, 5940-5947.

186. G. Qu, J. Cheng, X. Li, D. Yuan, P. Chen, X. Chen, B. Wang, H. Peng, *Adv. Mater.* **2016**, *28*, 3646-3652.

187. B. Pramanick, L. B. Cadenas, D. -M. Kim, W. Lee, Y. -B. Shim, S. O. Martinez-Chapa, M. J. Madou, H. Hwang, *Carbon* **2016**, *107*, 872-877.

188. N. Yu, H. Yin, W. Zhang, Y. Liu, Z. Tang, M. -Q. Zhu, *Adv. Energy Mater.* **2016**, *6*, 1501458.

189. X. Zhu, P. Zhang, S. Xu, X. Yan, Q. Xue, *ACS Appl. Mater. Interfaces* **2014**, *6*, 11665-11674.

190. X. Ding, Y. Zhao, C. Hu, Y. Hu, Z. Dong, N. Chen, Z. Zhang, L. Qu, *J. Mater. Chem. A* **2014**, *2*, 12355-12360.

191. C. Hu, X. Zhai, L. Liu, Y. Zhao, L. Jiang, L. Qu, *Sci. Rep.* **2013**, *3*, 2065-2075.

192. S. H. Ko, D. Lee, H. W. Kang, K. H. Nam, J. Y. Yeo, S. J. Hong, C. P. Grigoropoulos,

H. J. Sung, *Nano Lett.* **2011**, *11*, 666-671.

193. L. Mai, X. Tian, X. Xu, L. Chang, L. Xu, *Chem. Rev.* **2014**, *114*, 11828-11862.

194. Q. Zhou, X. Ye, Z. Wan, C. Jia, *J. Power Sources* **2015**, *296*, 186-196.

195. D. P. Dubal, D. Aradilla, G. Bidan, P. Gentile, T. J. S. Schubert, J. Wimberg, S. Sadki, P. Gomez-Romero, *Sci. Rep.* **2015**, *5*, 9771.

196. Z. Zhang, F. Xiao, S. Wang, *J. Mater. Chem. A* **2015**, *3*, 11215-11223.

197. J. Zhu, J. He, *ACS Appl. Mater. Interfaces* **2012**, *4*, 1770-1776.

198. J. Chang, M. Jin, F. Yao, T. H. Kim, V. T. Le, H. Yue, F. Gunes, B. Li, A. Ghosh, S. Xie, Y. H. Lee, *Adv. Funct. Mater.* **2013**, *23*, 5074-5083.

199. H. Xia, M. Lai, L. Lu, *J. Mater. Chem.* **2010**, *20*, 6896-6902.

200. M. Huang, Y. Zhang, F. Li, Z. Wang, N. Hu, Z. Wen, Q. Liu, *Sci. Rep.* **2014**, *4*, 4518.

201. M. V. K. Azhagan, M. V. Vaishampayana, M. V Shelke, *J. Mater.Chem. A* **2014**, *2*, 2152-2159.

202. J. -L. Shi, W. -C. Du, Y. -X. Yin,Y. -G. Guo, L. -J. Wan, *J. Mater. Chem. A* **2014**, *2*, 10830-10834.

203. M. Beidaghi, C. L. Wang, *Adv. Funct. Mater.* **2012**, *22*, 4501-4510.

204. W. Liu, Y. Feng, X. Yan, J. Chen, Q. Xue, *Adv. Funct. Mater.* **2013**, *23*, 4111-4122.

205. J. Yan, Z. Fan, W. Sun, G. Ning, T. Wei, Q. Zhang, R. Zhang, L. Zhi, F. Wei, *Adv. Funct. Mater.* **2012**, *22*, 2632-2641.

206. Z. Tang, C. -H. Tang, H. A. Gong, *Adv. Funct. Mater.* **2012**, *22*, 1272-1278.

207. Z. -S. Wu, K. Parvez, A. Winter, H. Vieker, X. Liu, S. Han, A. Turchanin, X. Feng, K. Müllen, *Adv. Mater.* **2014**, *26*, 4552-4558.

208. Y. Fu, X. Cai, H. Wu, Z. Lv, S. Hou, M. Peng, X. Yu, D. Zou, *Adv. Mater.* **2012**, *24*,

5713-5718.

209. W. Liu, C. Lu, X. Wang, R. Y. Tay, B. K. Tay, *ACS Nano* **2015**, *9*, 1528-1542.

210. S. Pan, J. Deng, G. Guan, Y. Zhang, P. Chen, J. Ren, H. Peng, *J. Mater. Chem. A* **2015**, *3*, 6286-6290.

211. X. Xiao, T. Li, P. Yang, Y. Gao, H. Jin, W. Ni, W. Zhan, X. Zhang, Y. Cao, J. Zhong, L. Gong, W. -C. Yen, W. Mai, J. Chen, K. Huo, Y. -L. Chueh, Z. L. Wang, J. Zhou, *ACS Nano* **2012**, *6*, 9200-9206.

212. H. Jin, L. Zhou, C. L. Mak, H. Huang, W. M. Tang, H. L. W. Chan, *J. Mater. Chem. A* **2015**, *3*, 15633-15641.

213. G. Sun, X. Zhang, R. Lin, J. Yang, H. Zhang, P. Chen, *Angew. Chem. Int. Ed.* **2015**, *127*, 4734-4743.

214. J. Li, H. Q. Xie, Y. Li, J. Liu, Z. X. Li, *J. Power Sources* **2011**, *196*, 10775-10781.

215. J. Tao, N. Liu, W. Ma, L. Ding, L. Li, J. Su, Y. Gao, *Sci. Rep*. **2013**, *3*, 2286.

216. J. A. Lee, M. K. Shin, S. H. Kim, H. U. Cho, G. M. Spinks, G. G. Wallace, M. D. Lima, X. Lepró, M. E. Kozlov, R. H. Baughman, S. J. Kim, *Nat. Commun.* **2013**, *4*, 1970.

217. L. Kou, T. Huang, B. Zheng, Y. Han, X. Zhao, K. Gopalsamy, H. Sun, C. Gao, *Nat. Commun.* **2014**, *5*, 3754.

218. M. F. EI-Kady, R. B. Kaner, *Nat. Commun.* **2013**, *4*, 1475.

219. W. Liu, M. Zhang, M. Li, B. Li, W. Zhang, G. Li, M. Xiao, J. Zhu, A. Yu, Z. Chen, *Adv. Energy Mater.* **2020**, *10*, 1903724.

220. W. Liu, M. Li, G. Jiang, G. Li, J. Zhu, M. Xiao, Y. Zhu, R. Gao, A. Yu, M. Feng, Z. Chen, *Adv. Energy Mater.* **2020**, *10*, 202001275.

221. C. Couly, M. Alhabeb, K. L. Van Aken, N. Kurra, L. Gomes, A. M. Navarro-Suárez, B.

Anasori, H. N. Alshareef, Y. Gogotsi, *Adv. Electron. Mater.* **2018**, *4*, 1700339.

222. K. Lee, H. Lee, Y. Shin, Y. Yoon, D. Kim, H. Lee, *Nano Energy* **2016**, *26*, 746-754.

223. X. Pu, M. Liu, L. Li, S. Han, X. Li, C. Jiang, C. Du, J. Luo, W. Hu, Z. L. Wang, *Adv. Energy Mater.* **2016**, *6*, 1601254.

224. J. W. Long, B. Dunn, D. R. Rolison, H. S. White, *Chem. Rev.* **2004**, *104*, 4463-4492.

225. M. Armand, J. -M. Tarascon, *Nature* **2008**, *451*, 652-657.

226. X. Shi, S. Pei, F. Zhou, W. Ren, H. -M. Cheng, Z. -S. Wu, X. Bao, *Energy Environ. Sci.* **2019**, *12*,1534-1539.

227. J. Chang, S. Adhikari, T. H. Lee, B. Li, F. Yao, D. T. Pham, V. T. Le, Y. H. Lee, *Adv. Energy Mater.* **2015**, *5*, 1500003.

228. Y. -Y. Peng, B. Akuzum, N. Kurra, M. -Q. Zhao, M. Alhabeb, B. Anasori, E. C. Kumbur, H. N. Alshareef, M. -D. Gerc, Y. Gogotsi, *Energy Environ. Sci.* **2016**, *9*, 2847-2854.

229. S. Das, R. Ghosh, D. Mandal, A. K. Nandi, *ACS Appl. Energy Mater.* **2019**, *2*, 6642-6654.

230. X. Shi, Z. -S. Wu, J. Qin, S. Zheng, S. Zheng, S. Wang, F. Zhou, C. Sun, X. Bao, *Adv.Mater.* **2017**, *29*, 1703034.

231. W. Liu, C. Lu, H. Li, R. Y. Tay, L. Sun, X. Wang, W. L. Cow, X. Wang, B. K. Tay, Z. Chen, J. Yan, K. Feng, G. Lui, R. Tjandra, L. Rasenthiram, G. Chiu, A. Yu, *J. Mater. Chem. A* **2016**, *4*, 3754-3764.

232. W. Si, C. Yan, Y. Chen, S. Oswald, L. Han, O. G. Schmidt, *Energy Environ.Sci.* **2013**, *6*, 3218-3223.

233. A. Ferris, S. Garbarino, D. Guay, D. Pech, *Adv. Mater.* **2015**, *27*, 6625-6629.

234. L. Zhang, D. DeArmond, N. T. Alvarez, R. Malik, N. Oslin, C. McConnell, P. K. Adusei, Y. -Y. Hsieh, V. Shanov, *Small* **2017**, *13*, 1603114.

235. S. Wang, Z.-S. Wu, S. Zheng, F. Zhou, C. Sun, H.-M. Chen, X. Bao, *ACS Nano* **2017**, *11*, 4283-4291.

236. J. Pu, X. Wang, R. Xu, K. Komvopoulos, *ACS Nano* **2016**, *10*, 9306-9315.

237. H. Zhang, X. Yu, P. V. Braun, *Nat. Nanotech.* **2011**, *6*, 277-281.

238. K. Cao, L. Jiao, W. K. Pong, H. Liu, T. Zhou, Z. Guo, Y. Wang, H. Yaun, *Small* **2016**, *12*, 2991-2997.

239. Y. Xu, X. Wang, W. L. Zhang, F. Lv, S. Guo, *Chem. Soc. Rev.* **2018**, *47*, 586-625.

240. X. Wang, G. Sun, N. Li, P. Chen, *Chem. Soc. Rev.* **2016**, *45*, 2239-2262.

241. W. W. Liu, J. N. Wang, *Chem. Commun.* **2011**, *47*, 6888-6890.

242. S. Lin, L. Dong, J. Zhang, H. Lu, *Chem. Mater.* **2016**, *28*, 2138-2146.

243. S. Sarkar, D. Gandla, Y. Venkatesh, P. R. Bangal, S. Ghosh, Y. Yang, S. Misra, *Phys. Chem. Chem. Phys.* **2016**, *18*, 21278-21287.

244. J. Han, G. Xu, B. Ding, J. Pan, H. Dou, D. R. MacFarlane, *J. Mater. Chem. A* 2014, *2*, 5352-5357.

245. D. -W. Wang, F. Li, L. -C. Yin, X. Lu, Z. -G. Chen, I. R. Gentle, G. Q. Lu, H. -M. Chen, *Chem. -Eur. J.*, **2012**, *18*, 5345-5351.

246. T. Shao, G. Wang, X. An, S. Zhou, Y. Xia, C. Zhu, *RSC Adv.* **2014**, *4*, 47977-47981.

247. X. He, Z. Tang, L. Gao, F. Wang, J. Zhao, Z. Miao, X. Wu, J. Zhou, Y. Su, S. Zhou, *J. Electroanal. Chem.* **2020**, *871*, 114311.

248. N. Soin, S. S. Roy, S. Sharma, T. Thundat, J. A. McLaughlin, *J. Solid State Electrochem.* **2013**, *17*, 2139-2149.

249. L. -F. Chen, X. -D. Zhang, H. -W. Liang, M. Kong, Q. F. Guan, P. Chen, Z. -Y. Wu, S. -H. Yu, *ACS Nano* **2012**, *6*, 7092-7102.

250. Q. Wang, J. Yan, Y. Wang, T. Wei, M. Zhang, X. Jing, Z. Fan, *Carbon* **2014**, *67*, 119-127.

251. S. Xu, D. Li, P. Wu, *Adv. Funct. Mater.* **2015**, *25*, 1127-1136.

252. G. Ou, P. Fan, X. Ke, Y. Xu, K. Huang, H. Wei, W. Yu, H. Zhang, M. Zhong, H. Wu, Y. Li, *Nano Res.* **2018**, *11*, 751-761.

253. W. Gu, Y. Yan, X. Cao, C. Zhang, C. Ding, Y. Xian, *J. Mater. Chem. B* **2016**, *4*, 27-31.

254. D. Gopalakrishnan, D. Damien, M. M. Shaijumon, *ACS Nano* **2014**, *8*, 5297-5303.

255. Y. Xu, L. Yan, H. Xu, *Sci. Rep.* **2019**, *9*, 2931.

256. W. Gu, Y. Yan, C. Zhang, C. Ding, Y. Xian, *ACS Appl. Mater. Interfaces* **2016**, *8*, 11272-11279.

257. T. Zhao, Z. Xing, Z. Xiu, Z. Li, S. Yang, W. Zhou, *ACS Appl. Mater. Interfaces* **2019**, *11*, 7104-7111.

258. A. Ramadoss, T. Kim, G. -S. Kim, S. J. Kim, *New J. Chem.* **2014**, *38*, 2379-2385.

259. M. Acerce, D. Voiry, M. Chhowalla, *Nat. Nanotech.* **2015**, *10*, 313-318.

260. L. Gao, S. Yang, W. Gao, Z. Liu, Y. Gong, L. Ma, G. Shi, S. Lei, Y. Zhang, S. Zhang, R. Vajtai, P. M. Ajayan, *Small* **2013**, *9*, 2905-2910.

261. Y. Yang, H. Fei, G. Ruan, C. Xiang, J. M. Tour, *Adv. Mater.* **2014**, *26*, 8163-8168.

262. M. A. Bissett, I. A. Kinloch, R. A. W. Dryfe, *ACS Appl. Mater. Interfaces* **2017**, *7*, 17388-17398.

263. L. Ren, G. Zhang, Z. Yan, L. Kang, H. Xu, F. Shi, Z. Lei, Z. -H. Liu, *ACS Appl. Mater. Interfaces* **2015**, *7*, 28294-28302.

264. X. Li, C. Zhang, S. Xin, Z. Yang, Y. Li, D. Zhang, P. Yao, *ACS Appl. Mater. Interfaces* **2016**, *8*, 21373-21380.

265. M. Wang, H. Fei, P. Zhang, L. Yin, *Electrochim. Acta.* **2016**, *209*, 389-398.

266. V. Bonu, B. Gupta, S. Chandra, A. Das, S. Dhara, A. K. Tyagi, *Electrochimica Acta.* **2016**, *203*, 230-237.

267. D. Pech, M. Brunet, H. Durou, P. Huang, V. Mochalin, Y. Gogotsi, P. -L. Taberna, P. Simon, *Nat. Nanotechnol.* **2010**, *5*, 651-654.

268. K. Sheng, Y. Sun, C. Li, W. Yaun, G. Shi, *Sci. Rep.* **2012**, *2*, 247.

269. Z. -S Wu, K. Parvez, X. Feng, K. Müllen, *Nat. Commun.* **2013**, *4*, 2487.

270. A. Ghosh, V. T. Le, J. J. Bae, Y. H. Lee, *Sci. Rep.* **2013**, *3*, 2939.

271. J. Lin, C. G. Zhang, Z. Yan, Y. Zhu, Z. W. Peng, R. H. Hauge, D. Natelson, J. M. Tour, *Nano Lett.* **2013**, *13*, 72-78.

272. P. Zhang, Y. Li, G. Wang, F. Wang, S. Yang, F. Zhu, X. Zhuang, O. G. Schmidt, X. Feng, *Adv. Mater.* **2019**, *31*, 1806005.

273. F. S. Wen, C. X. Hao, J. Y. Xiang, L. M. Wang, H. Hou, Z. B. Su, W. T. Hu, Z. Y. Liu, *Carbon* **2014**, *75*, 236-243.

274. M. Beidaghi, C. L. Wang, *Adv. Funct. Mater.* **2012**, *22*, 4501-4510.

275. M. Zhang, Q. Zhou, J. Chen, X. Yu, L. Huang, Y. Li, C. Li, G. Shi, *Energy Environ. Sci.* **2016**, *9*, 2005-2010.

276. C. Lethien, J. L. Bideau, T. Brousse, *Energy Environ. Sci.* **2019**, *12*, 96-115.